universität wien

MASTERARBEIT / MASTER'S THESIS

Titel der Masterarbeit / Title of the Master's Thesis

„Exploration study for trace detection of long lived fission products at VERA“

verfasst von / submitted by

Oscar Marchhart, BSc

angestrebter akademischer Grad / in partial fulfilment of the requirements for the degree of

Master of Science (MSc)

Wien, 2020 / Vienna, 2020

Studienkennzahl lt. Studienblatt / degree programme code as it appears on the student record sheet:	UA 066 876
Studienrichtung lt. Studienblatt / degree programme as it appears on the student record sheet:	Masterstudium Physik
Betreut von / Supervisor:	Univ.-Prof. Dipl.-Ing. Dr. Robin Golser

Abstract

Accelerator mass spectrometry (AMS) is able to detect extremely low concentrations of trace isotopes. Depending on the chosen nuclide, isotopic ratios down to 10^{-16} can be measured. The interference of abundant stable isobars is the limiting factor of AMS, because in the mass range A≈100 amu these isobars can not be sufficiently separated from the trace isotopes neither by the electrostatic analyzers and bending magnets nor in the detectors.
A novel approach at the Vienna Environmental Research Accelerator (VERA) is to suppress isobars via non-resonant laser photodetachment in a gas-filled radiofrequency quadrupole (RFQ) ion guide with the Ion Laser Interaction Mass Spectrometry (ILIAMS) setup. This is achieved by overlapping the ion beam with a laser beam using elemental or molecular anions whose electron affinities (EA) are suitable for optical filtering. Suitable anionic systems require that the EA of the interfering isobar is lower than that of the isotope of interest. Hence, the unwanted isobars are neutralized via laser photodetachment while the isotope of interest remains unaffected.

The aim of this master thesis was to explore the feasibility of measuring environmental concentrations of the long lived fission products (LLFP) ^{90}Sr, ^{99}Tc and ^{107}Pd with the ILIAMS setup at VERA. The elemental EAs of these LLFPs are not suitable for laser photodetachment, therefore suitable molecules have to be used.
The investigations on ^{90}Sr show that the best sample matrix is a 1:8 mixture of SrF_2+PbF_2 by weight as it results in the highest ionization yield for SrF_3^-. SrF_3^- is unaffected by either a 532-nm or 355-nm laser, while the isobaric molecules YF_3^- and ZrF_3^- are efficiently detached. By using a He+O_2 mixture (30:1), instead of pure He, as buffer gas adds almost an order of magnitude to the suppression of the isobars reaching a suppression factor of 10^7 with ILIAMS. Ion cooler transmissions of up to 35% can be reached, while the accelerator transmission at 3 MV, using He stripping, for the +3 charge state is around 23%. The energy of the Sr^{3+} particles is around 10.89 MeV giving additional separation of $^{90}Sr^{3+}$ and $^{90}Zr^{3+}$ in a compact gas ionization chamber (GIC) with two separate anodes. In-house made reference materials were produced through a dilution series. First ^{90}Sr measurements with these reference materials were successfully conducted reaching a blank level of $(4.5 \pm 3.2) \times 10^{-15}$ corresponding to a limit of detection < 0.1 mBq,

improving the previous limit of detection by a factor of 30. Thus AMS is now the most sensitive technique for measuring ^{90}Sr. Taking everything into consideration, ^{90}Sr measurements of environmental concentrations at VERA are feasible.
Investigations on ^{99}Tc show that by adding Nb to a matrix containing Ru heavily suppresses the formation of RuO^-, RuF_3^- and higher oxide or fluoride molecules of Ru. The EAs of all oxide and fluoride molecules for the isobars Ru and Mo, have been investigated with the 532-nm laser, whereas the EAs of RuO_x^- also have been tested with the 355-nm laser. Without the knowledge of the EAs of TcF_x^- and TcO_x^- no molecular system can be picked or dismissed as suitable or not. Nonetheless due to RuO_3^- not being sufficiently suppressed with the current setup it is highly unlikely that TcO_3^- is suitable. Depending on the EAs of TcO_2^- and MoO_2^-, which still have to be investigated, this molecular system might be suitable for ^{99}Tc/^{97}Tc measurements.
The last LLFP investigated was ^{107}Pd. The same way as for Tc the EAs of the oxide and fluoride molecules of Pd and its isobar Ag were investigated with the 532-nm laser and additionally the oxide molecules of both elements were tested with the 355-nm laser. With the current lasers available all molecules except PdF^- and PdF_2^- can already be dismissed, because their EAs are not suitable for the ILIAMS setup.

Zusammenfassung

Beschleuniger-Massespektrometrie (AMS) ist in der Lage extrem niedrige Konzentrationen von Spurenisotopen zu detektieren. Je nach Nuklid können Isotopenverhältnisse von bis zu 10^{-16} gemessen werden. Limitiert wird AMS durch stabile Isobare mit hoher natürlicher Häufigkeit, weil im Massenbereich A≈100 amu die Isobare weder durch die elektrostatischen Analysatoren und Magnete noch in den Detektoren ausreichend von den Spurenisotopen getrennt werden können.
Eine neuartige Methode am Vienna Environmental Research Accelerator (VERA) ist die Unterdrückung von Isobaren durch nicht-resonantes Laser Photodetachment in einem gasgefüllten Hochfrequenzquadrupol mithilfe des Ion Laser Interaction Mass Spectrometry (ILIAMS) Setups. Dies wird durch Überlappen des Ionenstrahls, bestehend aus atomaren oder molekularenn Anionen deren Elektronenaffinitäten (EA) für optische Filterung geeignet sind, mit einem Laserstrahl erreicht. Damit ein Anionensystem geeignet ist muss die EA des Isobars kleiner sein als die EA des Spurenisotops. Dadurch wird das isobare Anion durch Laser Photodetachment neutralisiert während das Spurenisotop unbeeinflusst bleibt.

Ziel dieser Masterarbeit war es die Umsetzbarkeit der Messung von Umweltkonzentrationen der langlebigen Spaltprodukte (LLFP) ^{90}Sr, ^{99}Tc und ^{107}Pd mit dem ILIAMS-Setup für VERA zu untersuchen. Die atomaren EA dieser LLFPs sind ungeeignet für Laser Photodetachment, daher müssen entsprechend geeignete molekulare Systeme verwendet werden.
Die Untersuchungen bezüglich ^{90}Sr haben ergeben, dass die Verwendung einer SrF_2+PbF_2 Matrix in einem Mischungsverhältnis von 1:8 nach Gewicht die besten SrF_3^- Ionisationsausbeuten erzielt. SrF_3^- bleibt unter Verwendung eines 532 nm oder 355 nm Lasers unbeeinflusst, während die isobaren Moleküle YF_3^- und ZrF_3^- neutralisiert werden. Anstatt pures He als Buffergas zu verwenden eignet sich eine Mischung aus He+O_2, welche die Isobarenunterdrückung um beinahe eine Größenordnung verbessert. Dadurch erreicht man mit ILIAMS einen Unterdrückungsfaktor der Isobare von 10^7. Eine Transmission durch den Ionenkühler von bis zu 35% wird erreicht. Die Beschleunigertransmission für den +3 Ladungszustand bei 3 MV mit Helium als Strippergas ist 23%. Die Energie der Sr^{3+} Teilchen liegt bei ungefähr 10.89 MeV, wodurch eine zusätzliche Trennung von $^{90}Sr^{3+}$ und $^{90}Zr^{3+}$ in einer kompakten Gasionisationskammer mit zwei separaten Anoden erreicht wird. Eigene Referenzmaterialien wurden durch eine Verdünnungsreihe hergestellt

und damit erste erfolgreiche ^{90}Sr Messungen durchgeführt. Es wurde ein Blanklevel von $(4.5 \pm 3.2)\times10^{-15}$ erreicht, welches einem Detektionslimit von <0.1 mBq entspricht, wodurch das alte Detektionslimit um einen Faktor 30 verbessert wurde. Dadurch hat AMS die beste Sensitivität für ^{90}Sr. Basierend auf den Erkenntnissen zu Sr sind Messungen von Umweltkonzentrationen für ^{90}Sr bei VERA möglich.
Die Untersuchungen bezüglich ^{99}Tc zeigen, dass durch Beimischung von Nb in eine Matrix, die Ru enthält, die Bildung von RuO^-, RuF_3^- und höheren Fluorid- oder Oxidmolekülen von Ru stark unterdrückt wird. Desweiteren wurden die Elektronenaffinitäten aller Fluorid- und Oxidmoleküle der beiden Isobare Ru und Mo mit dem 532 nm Laser untersucht. Zusätzlich dazu wurden die RuO_x^- Moleküle ebenfalls mit dem 355 nm Laser untersucht. Jedoch können ohne Kenntnis der Elektronenaffinitäten der Fluorid- und Oxidmoleküle von Tc derzeit noch keine Moleküle als geeignet oder ungeeignet klassifiziert werden. Dennoch ist es sehr unwahrscheinlich, dass TcO_3^- als molekulares System geeignet ist, weil RuO_3^- mit dem derzeitigen Setup nicht ausreichend stark unterdrückt werden kann. Sofern die Elektronenaffinität des Moleküls TcO_2^- größer ist als von MoO_2^- könnte es für Messungen von ^{99}Tc/^{97}Tc verwendet werden könnte.
Das letzte untersuchte LLFP war ^{107}Pd. Wie bei Tc wurden die Elektronenaffinitäten der Oxid- und Fluoridmoleküle von Pd und seinem Isobar Ag mit dem 532 nm Laser getestet, wobei die Oxidmoleküle zusätzlich mit dem 355 nm Laser untersucht wurden. Die vorhandenen Laser können nur für PdF^- und möglicherweise PdF_2^- verwendet werden. Die Elektronenaffinitäten aller anderen Moleküle sind nicht geeignet.

Contents

1. Motivation

Accelerator Mass Spectrometry (AMS) is the most sensitive method to measure small amounts of long lived trace isotopes. Typical isotopic abundances as low as 10^{-12}-10^{-16} can be measured with high efficiency. AMS has a broad range of applications, in various fields of research, and measures nuclides such as ^{10}Be, ^{14}C, ^{26}Al, ^{36}Cl, ^{60}Fe, ^{129}I, ^{236}U and many more.
Some of the applications include ^{14}C for archaeological dating, ^{10}Be, ^{26}Al and ^{36}Cl for geological dating (e.g. dating of rocks), ^{60}Fe for the detection of supernovae and ^{129}I, ^{236}U for ocean currents. A more detailed list of used nuclides and their applications in AMS can be found in (Kutschera 2013).

Using conventional radiometric methods (e.g. decay counting) is not feasible for long lived trace isotopes with half lives of $T_{1/2} \geq 1000$ a, because it would require large sample sizes or counting times. With AMS however, only small amounts of target material, typically a few mg, are needed for sufficiently high counting statistics and measuring times of a few hours.
The advantage of AMS compared to other mass spectrometric methods (e.g. ICP-MS, TIMS) is the suppression of isobaric background and its sensitivity limit. With the accelerator the ion beam is accelerated to energies in the MeV range. At those energies molecular isobars are dissociated and their fragments are subsequently separated from the trace isotopes using electrostatic analyzers and bending magnets as mass filters as well as in the detectors.
In AMS solid target material is pressed into cathodes and sputtered, typically with cesium, to produce negative ions. The ions are extracted from the source and possible interfering impurities of the target material need to be separated in the remaining AMS system, in order to achieve sensitive concentration measurements. A typical AMS system consists of an ion source, electrostatic and magnetic fil-

ters and an accelerator. The separation of molecular isobars and the isotope of interest can be achieved by the stripping process inside the accelerator. During the stripping process electrons are stripped of the initially produced anions and molecules are dissociated into fragments (Purser 1977). At a charge state of +3 or higher most isobaric molecules dissociate and their fragments can be removed with additional filters. This is not true for actinides and thus other methods need to be applied to eliminate the isobaric molecules (Synal 2013), e.g. a second analyzing magnet on the high energy side.

Getting rid of abundant and stable elemental isobars is more challenging, because they still remain as fragments after the dissociation of the molecules during the stripping process. This problem can be avoided in rare cases by using negative ions, because the formation of stable anions is not possible for element with negative electron affinities (EA), e.g. ^{14}N in radiocarbon measurements. For the majority of elements this can not be utilized and thus different methods have to be used. A commonly used method exploits the different energy loss of isobar and isotope of interest in a detector (Wacker et al. 2004) or in a gas-filled magnet (Paul 1990, Knie et al. 1997). Both require high energies to reach sufficient isobar suppression. Using degrader foils showed to be an effective method for specific isotopes, e.g. for the ^{10}Be/^{10}B or ^{182}Hf/^{182}W separation (Raisbeck et al. 1984, Vockenhuber et al. 2007).

In recent years new AMS facilities tend to buy smaller accelerators and measurements are done with lower energies (e.g. MILEA system from *Ionplus*). Due to lower ion energies the isobar suppression of the common methods is typically worse and thus not able to sufficiently separate the abundant isobars from the trace isotopes. Thus, new methods for elemental isobar suppression have to be developed. The ^{10}Be measurements with degrader foils are already able to compete with high energy AMS facilities (Müller et al. 2010).

Currently there are investigations with two different methods of elemental isobar suppression that allow separation at low energies. The first method utilizes low energy ion–molecule reactions and collisional induced dissociation processes inside a gas-filled reaction cell, between ions in the eV range and a reaction gas. This solution was first investigated at the IsoTrace laboratory in Toronto (Litherland et al. 2007). Further developments of this technique are currently done at the A.E. Lalonde AMS Laboratory in Ottawa (Alary et al. 2015).

The second one is an element selective method that uses a combination of chemical reactions similar to the reaction cell in Ottawa and electromagnetic radiation provided by a laser. The technique exploits differences in the electron affinities between the isobars and the isotope of interest to neutralize the unwanted isobars via non-resonant laser photodetachment while leaving the isotope if interest unaffected. It was already successfully applied to AMS measurements (Martschini et al. 2019, Lachner et al. 2019), using the Ion Laser InterAction Mass Spectrometry (ILIAMS) system at the Vienna Environmental Research Accelerator (VERA).

The objective of this master thesis was the investigation of molecular systems of the long lived fission products ^{90}Sr, ^{99}Tc and ^{107}Pd to find systems suitable for AMS at VERA. If such systems were found, first attempts of measuring the trace isotopes by AMS were conducted to assess their detection efficiency and the sensitivity limit.

2. Introduction

2.1. Vienna Environmental Accelerator - VERA

The Vienna Environmental Research Accelerator (VERA) is an AMS facility at the University of Vienna. The facility was initially built to measure mainly ^{14}C, with the potential to be upgraded for other isotopes, and put into operation in 1996. The precision achieved on the first performance tests was close to expectation (Priller et al. 1997).
In 2001 the facility was expanded to be able to measure various other isotopes, ranging from light (^{10}Be, ^{26}Al) to heavy (e.g. ^{236}U, ^{244}Pu) ones (Steier et al. 2004). The last big extension to the facility was the addition of the Ion Laser InterAction Mass Spectrometry (ILIAMS) and a second ion source in 2018. With this new setup even trace amounts of isotopes with abundant stable isobars can be measured (e.g. ^{36}Cl, ^{90}Sr) (Martschini et al. 2019).

A scheme of the current layout of VERA is shown in Fig. 2.1. VERA contains two Sources of Negative Ions by Cesium Sputtering (SNICS) holding up to 40 samples per sample wheel. Besides the second ion source and the ILIAMS setup (see section 2.3), VERA resembles a typical AMS facility. Depending on the used ion source, the ion beam is typically extracted from the SNICS with 30 keV or 70 keV, followed by an electrostatic spherical analyzer (ESA) and the injection magnet, acting as a m/q filter for the low energy side. With the 3-MV-Pelletron tandem accelerator manufactured by the National Electrostatics Corporation (NEC), which is the key component for any AMS facility, the ions are accelerated into the MeV range and their electrons are stripped off by either a thin foil or stripper gas, located at the high voltage terminal in the middle of the accelerator. The high energy cations extracted from the accelerator can be filtered and separated

using a Wienfilter, analyzing magnets and another ESA. Afterwards, the isotope of interest can be detected in one of the ionization chambers following the high energy side ESA.
VERA has multiple detection beam lines dedicated to the detection of different trace isotopes. Isotopes such as ^{14}C and ^{26}Al are measured in the gas ionization chamber (GIC) right after the high energy side ESA. Following the mentioned detector there is the so-called switching magnet splitting the beam line into four separate beam lines each serving different purposes. One beam line is dedicated to analysis of materials using proton induced x-ray emission (PIXE), the other three beam lines are dedicated to measure either ^{10}Be, ^{36}Cl or actinides (e.g. ^{236}U and ^{244}Pu). While the ^{10}Be and ^{36}Cl beam lines only differ in the used detectors the actinide beam line contains a second analyzing magnet, which is needed to further suppress the isobaric background (Steier et al. 2019).
Efficient tuning of the ion beam through the system is achieved by using beam optical components (e.g. lenses and steerers) and beam diagnostic elements (e.g. beam profile monitor, Faraday cup). Fast sequential injection of different masses can be achieved with a Multi Beam Switcher (MBS) at the injection magnet by accelerating or decelerating the anions before entering the magnet. During measurements, the stable isotopes can be measured in the offset Faraday cups located behind both magnets.

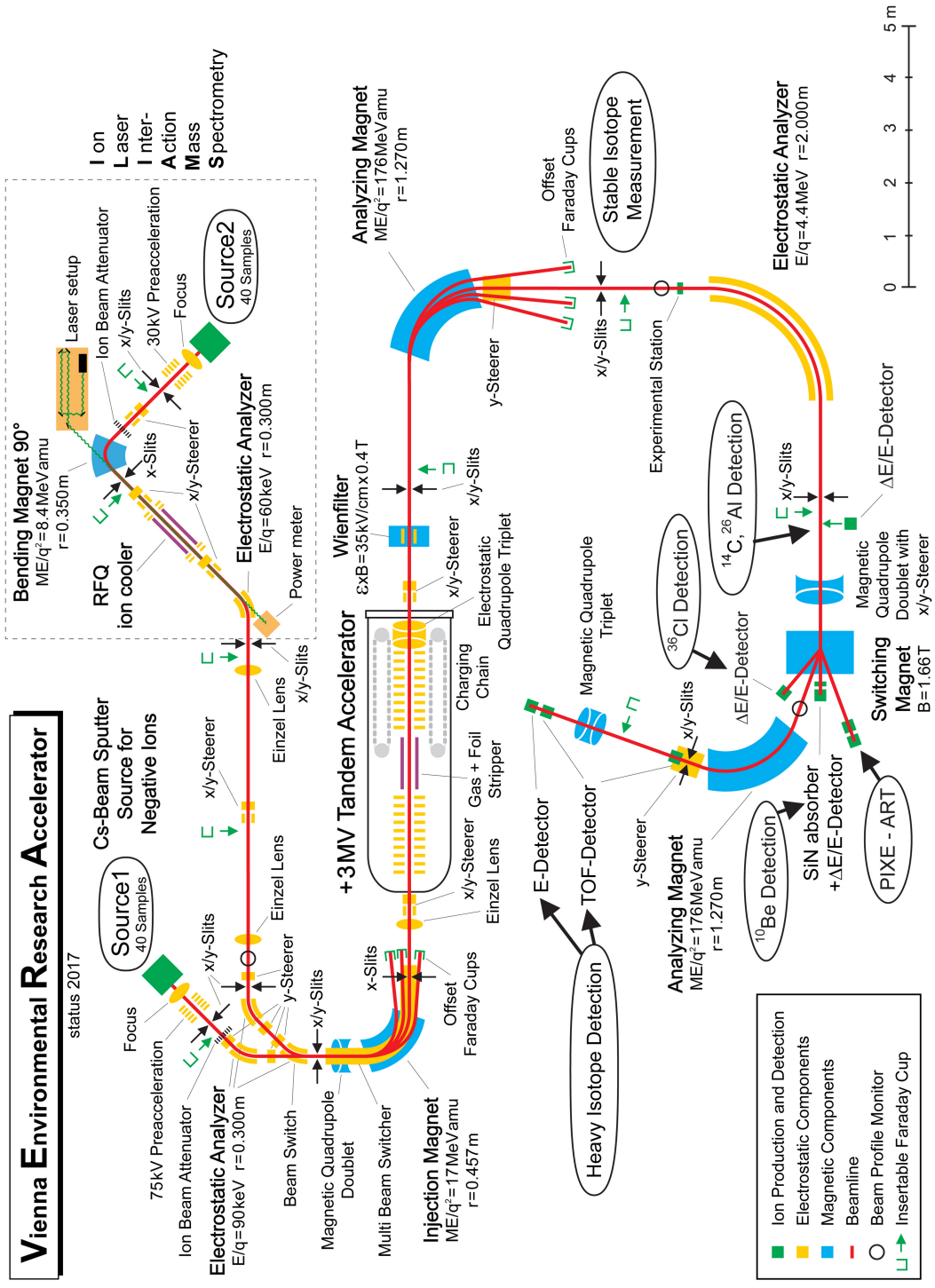

Figure 2.1.: Detailed scheme of VERA as of August 2019. The relevant ion source for this master thesis is Source 2 at the ILIAMS.

2.2. The long lived fission products ^{90}Sr,^{99}Tc,^{107}Pd

2.2.1. Production of long lived fission products by neutron induced fission

The long lived fission products (LLFP) ^{90}Sr, ^{99}Tc and ^{107}Pd, with half-lives of 28.9 a, 2.11×10^5 a and 6.5×10^6 a, respectively, are almost exclusively produced anthropogenically in the nuclear fuel cycle or by nuclear weapons.
For heavy nuclides (e.g.^{233}U, ^{235}U, ^{239}Pu) the fission into smaller fission fragments represents an exothermic reaction, if the binding energies of the fission products exceed the binding energy of its parent nuclide. The energy released in one nuclear fission is typically in the range of 200 MeV, which consist of the kinetic energy of the primary fission fragments (including produced neutrons) and the excitation energy of the fragments (released in decay processes of the fragments). Usually the fission process is a binary process, meaning that only two fission fragments are produced per fission, but in some rare cases a ternary fission (three fragments) takes place. Which fission fragments are produced mainly depends on the neutron energy and the parent nuclide (Fig. 2.2). Variation of these parameters slightly shifts the fragment peaks, nevertheless the most probable fission fragments lie within the mass region around 93 amu and 138 amu. An overall estimation of the cumulative neutron induced fission yields for the fragments ^{90}Sr, ^{99}Tc and ^{107}Pd are listed in Tab. 2.1. A more detailed list can be found in (Crouch 1977).

fission fragment	**fission yield (%)**
^{90}Sr	4.51 %
^{99}Tc	6.12 %
^{107}Pd	1.25 %

Table 2.1.: Overall cumulative fission yield of the fission fragments ^{90}Sr, ^{99}Tc and ^{107}Pd

Another important factor to consider is that the cross sections of the different processes following the neutron capture also depend on the energy of the captured neutron. This energy dependency is illustrated in Fig. 2.3 for ^{235,238}U and ^{239}Pu. For thermal neutrons (25 meV) the fission cross section of ^{239}Pu and ^{235}U are similar to each other, whereas the cross section of ^{238}U is several orders of magnitude

lower. At neutron energies around 1 MeV, the difference is only about a factor 80 and decreases further with increasing energy.

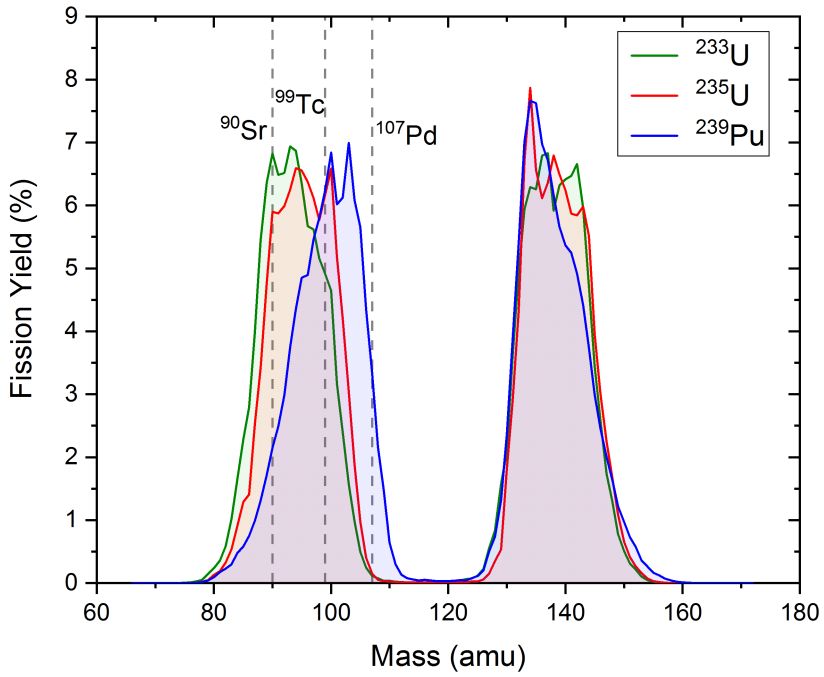

Figure 2.2.: Fission fragment yields by mass for thermal neutron induced fission of ^{233,235}U and ^{239}Pu. The data is taken from (*JAEA-Nuclear Data Center* 2012) using the JENDL/FPY-2011 data

As mentioned before, the LLFPs in the environment are almost exclusively produced anthropogenically in the nuclear fuel cycle and nuclear weapon tests. Not much information can be found about the production of the LLFPs through the bomb tests. Estimations show that about 140 - 160 TBq of ^{99}Tc have been produced by nuclear weapon detonations (García-Léon 2005) and that from roughly 350 atmospheric atomic bomb tests in the northern hemisphere, during late 1940 to early 1960, around 6×10^8 TBq of ^{90}Sr was released (Hu et al. 2010). Likewise at the Nevada test site a large inventory of radionuclides is present in the subsurface environments as a result of 828 underground nuclear weapon tests, which

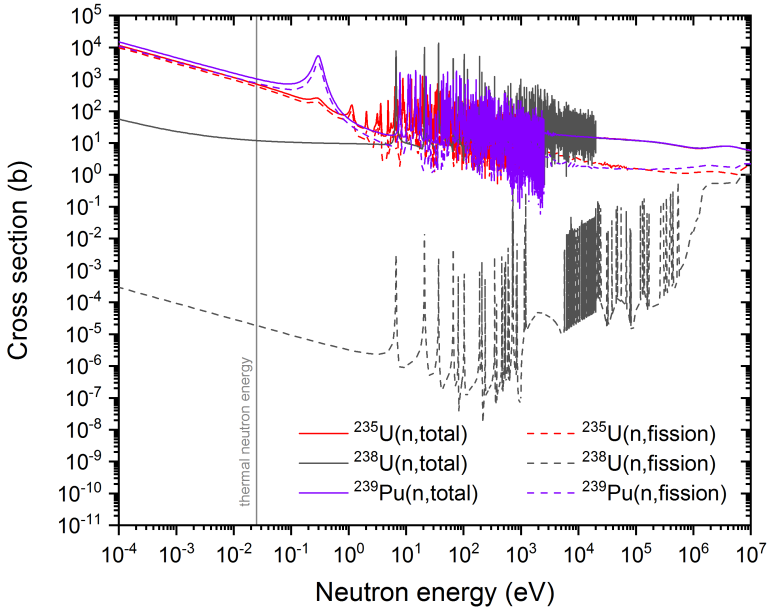

Figure 2.3.: Energy dependency for the total and fission cross section of ^{235,238}U and ^{239}Pu. Data plotted is the TENDL-2017 data taken from (*JANIS 4.0* 2013).

includes 5.58×10^{4} TBq of ^{90}Sr, 2.11×10^{1} TBq of ^{99}Tc and 1.27×10^{-1} TBq of ^{107}Pd (Hu et al. 2010). On the other hand, as of 2011, approximately 2500 t of spent fuel, containing 3 t of LLFPs, are produced annually in nuclear power plants of the European Union. The content of typical spent fuel from a pressurized water reactor (PWR) consists of $0.5\,\mathrm{kg\,t^{-1}}$ of ^{90}Sr, $0.82\,\mathrm{kg\,t^{-1}}$ of ^{99}Tc and $0.2\,\mathrm{kg\,t^{-1}}$ of ^{107}Pd (Salvatores and Palmiotti 2011), which corresponds to $2.46\times10^{3}\,\mathrm{TBq\,t^{-1}}$, $0.52\,\mathrm{TBq\,t^{-1}}$ and $3.82\times10^{-3}\,\mathrm{TBq\,t^{-1}}$ respectively.

In comparison, the natural inventory of the LLFPs in the earth crust can be estimated through the spontaneous fission of ^{238}U. Unfortunately this is not possible for Tc since there is no data available on how abundant Tc is in the earth crust. However, the abundances of U, Sr and Pd are roughly 2.7 ppm, 370 ppm and 0.015 ppm, respectively (Haynes et al. 2016, Yaroshevsky 2006). Hence, in the earth crust the isotopic ratios are $^{88}\mathrm{Sr}/^{238}\mathrm{U}=42.2$ and $^{108}\mathrm{Pd}/^{238}\mathrm{U}=6.9\times10^{-4}$. The cumulative fission yields of ^{90}Sr and ^{107}Pd from spontaneous fission of ^{238}U are 5.43 % and 0.14 %, respectively (England and Rider 1995). In secular equilibrium the ratios can be estimated to $^{90}\mathrm{Sr}/^{238}\mathrm{U}\approx1.9\times10^{-16}$ and $^{107}\mathrm{Pd}/^{238}\mathrm{U}\approx1.1\times10^{-12}$.

Which leads to estimated natural ratios of $^{90}Sr/^{88}Sr \approx 4.5 \times 10^{-18}$ and $^{107}Pd/^{108}Pd \approx 1.6 \times 10^{-9}$, corresponding to a natural activity of 0.03 mBq for Sr and 38.2 mBq for Pd.
The main pathway of release for the investigated LLFPs, i.e. ^{90}Sr, ^{99}Tc and ^{107}Pd, is direct release via nuclear bomb test and during accidents of nuclear power plants, such as Chernobyl (Pöllänen et al. 1997) and Fukushima (Hirose 2012). It is also possible to have some leakage into the environment during reprocessing or in older disposal facilities of nuclear waste, which do not satisfy the regulatory requirements. This poses radiological risks to the environment as ^{90}Sr has high mobility in soils and groundwater systems (Dewiere et al. 2004). ^{99}Tc is highly soluble in the form of TcO_4^- and also highly adsorbable to geological materials and clay in the oxidation state Tc^{4+} (Chen et al. 2000).

2.2.2. Applications of LLFPs

The three LLFPs, which were investigated in this thesis, have different fields of interest. More sensitive methods of detecting these trace isotopes could lead to wider range of possible applications.

^{90}Sr

^{90}Sr is produced with high yield of 4.51 % as a fission fragment. The currently preferred method of measuring ^{90}Sr is decay counting, but due to is gamma-less decay this is cumbersome and time consuming. To use decay counting secular equilibrium of ^{90}Sr and ^{90}Y has to be reached after radiochemical separation, which takes >2 weeks (Martin 1987). AMS does not only have a theoretically better detection limit, but would also deliver results faster.
Besides the applications of the trace isotope ^{90}Sr, also stable strontium has its applications. The $^{87}Sr/^{86}Sr$ ratio can be used in geology for dating the age of rocks and as a tracer of weathering processes and flow pathways in surface and groundwaters in different landscapes (Shand et al. 2009). There is also an application concerning food provenance, where among other the $^{87}Sr/^{86}Sr$ ratio of food commodities (e.g. cheese, wine, rice etc.) is used to determine their geographical origin (Kelly et al. 2005).
The range of applications for the trace isotope ^{90}Sr is diverse. One of these appli-

cations is using it as a tracer for water mass mixing and sedimentation processes (Egorov et al. 1999), because ^{90}Sr is highly mobile in soil and groundwater systems (Dewiere et al. 2004). Due to its chemical similarities to calcium it is important to reliably monitor the amount of ^{90}Sr released in nuclear accidents or as fallout of nuclear bombs and the possible occurrence in food such as milk (Campbell et al. 1959). If larger releases of strontium happen, it is incorporated in bones and teeth (Stamoulis et al. 1999), which could later lead to health problems such as leukemia. ^{90}Sr has also medical applications, e.g. treatment of in-sent restenosis (Popma et al. 2002).
Another application is in the industry, as a β-source for nuclear gauges measuring the thickness of a material (Liljestrand et al. 1976). This is done by placing the material between a β^- source and a detector. The thickness can be determined by measuring the signals reaching the detector with and without material.
Radioisotope thermal generators (RTG) are thermoelectric generators that produce an electric potential by exploiting the Seebeck effect. The effect is observed when a temperature gradient exists across the junction of two different metals or semiconductors. The heat for the RTGs is provided by the decay of a suitable radioisotope. ^{90}Sr is mainly deployed for unmanned lighthouses, coastal beacons and remote weather and environment monitoring stations, but does not look promising as a fuel replacement of ^{238}Pu for the general-purpose heat source radioisotope thermoelectric generator (GPHS-RTG) design used in space missions (O´Brien et al. 2008).

^{99}Tc

^{99}Tc is the most produced of the three fission fragments with a yield of around 6.12 %. It is mostly known for its short lived metastable nuclear isomer ^{99m}Tc with a half-life of 6 hours because of its wide spread application in nuclear medicine. The pertechnetate ion (TcO_4^-) is the main form of technetium in the environment and very mobile due to its high solubility and high geochemical mobility (Tagami and Uchida 2002). Technetium discharge into the environment from spent nuclear fuel is a problem and still a field of studies (Li et al. 2018). Due to its high sol-

ubility and mobility, ^{99}Tc can be used as an anthropogenic oceanographic tracer (Dahlgaard 1994), but also as a tracer for soil transport (Tagami and Uchida 2002). Currently, there is an ongoing project, funded by the „Fonds zur Förderung der wissenschaftlichen Forschung“ (FWF), investigating ^{99}Tc. The goal of this project is to study the migration behavior of ^{99}Tc from nuclear weapons fallout and subsequently estimate the global fallout of ^{99}Tc. Likewise, investigations on the possibility to make ^{99}Tc measurements accessible to low energy AMS facilities by using laser photodetachment are conducted (*Universität Wien - Isotopenphysik* 2019).
By far the most common application is the use of the nuclear isomer ^{99m}Tc in the medical field. It is used as a tracer for a variety of nuclear imaging purposes. Some of these include imaging for myocardial perfusion, diabetic foot, osteomyelitis, pulmonary actinomycosis (Maffioli et al. 1996), parathyroid imaging (Coakley et al. 1989) or brain scanning (Quinn 1965).

^{107}Pd

Palladium is a noble metal of the platinum group and the radioactive fragment ^{107}Pd has a low yield of 1.25, %. As a noble metal, Pd is not as mobile as Tc in the environment and is not amenable to disposal by nuclear transmutation, nonetheless it is part of nuclear waste. After five years of cooling, about 17 % of the Pd in nuclear waste is the radioactive ^{107}Pd, while the rest of the Pd in nuclear waste consists of stable isotopes (Bush 1991).
Recovering platinum metals (e.g. Pd, Rh etc.) from waste during the reprocessing process of spent fuel is of interest as it can be seen as an extra source for those metals. There are several possible hydrometallurgical processes for separation, but solvent extraction and electrolytic deposition are the most promising methods. Precipitation and ion exchange or extraction chromatography are less promising (Kolarik and Edouard 2003a, Kolarik and Edouard 2003b). Possible applications of the recovered Pd with residual radioactivity is in the nuclear industry. There the materials are radioactive themselves or become radioactive during operation. A more detailed list of possible applications can be found in (Kolarik and Edouard 2005).
Provided that sensitive detection techniques become available, ^{107}Pd could be used

as a tracer to investigate the largely unknown behavior of mobilized Pd in the environment. This includes the study of possible evoked health problems in form of particulate matter ejected from cars, since modern catalytic converters are made of Pd.

2.2.3. Detection of LLFPs

This section is dedicated to the present detection methods available (e.g. radiometric, AMS, ICP-MS etc.) as well as their current limitations for measuring ^{90}Sr,^{99}Tc and ^{107}Pd.

^{90}Sr

As far as strontium is concerned there is a published paper comparing all currently available mass spectrometric methods with each other as well as with the radiometric detection limit (Bu et al. 2016). In Tab. 2.2 the ^{90}Sr detection limits are listed. It shows that all methods do have similar detection limits with the exception of thermal ionization mass spectrometry (TIMS) and inductively coupled plasma mass spectrometry (ICP-MS). For resonance ionization mass spectrometry (RIMS) the absence of commercially available instruments and the complex procedures for instrument efficiency optimization are the main limitations. For AMS the limiting factor besides the relatively high cost and complex instrumental operation is the suppression of the isobar ^{90}Zr. Similar to AMS, the interference of the isobar ^{90}Zr limits ICP-MS.

method	**detection limit**
radiometric	$\approx 3\,\mathrm{mBq}$ (0.6 fg)
AMS	3 mBq (0.6 fg)
RIMS	4 mBq (8 fg)
ICP-MS	200 mBq/g (40 fg)
TIMS	N/A

Table 2.2.: Comparison of the ^{90}Sr detection limits of different methods. Data was taken from (Bu et al. 2016).

^{99}Tc

An overview of the detection limits of different methods for ^{99}Tc is given in Tab. 2.3. It shows that AMS presently is the most sensitive method for ^{99}Tc beating the other mass spectrometric methods by one order of magnitude, while radiometric measurements only reach detection limits around 1 - 5 mBq within 24 hours of measuring.
Currently, AMS measurements of ^{99}Tc can only be done by high energy AMS facilities, e.g. with the 14 -MV tandem accelerator at the Technical University of Munich (TUM) or the 14 UD pelletron accelerator at the Australian National University (ANU) in Canberra. Like for ^{90}Sr, the limiting factor for AMS is the suppression of the isobaric background, in this case ^{99}Ru. For this purpose, a Gas-filled Analyzing Magnet System (GAMS) is used in Munich (Quinto et al. 2019), whereas in Australia a gas-filled ionization chamber was developed. It has an anode plane optimized for ^{99}Tc and makes eight measurements of the energy loss along the ion track (Wacker et al. 2004).

method	**detection limit**	**reference**
radiometric	1-5 mBq (2-8 pg)	García-Léon 2005
AMS	0.3 µBq (0.5 fg)	Quinto et al. 2019
RIMS	3 µBq (4 fg)	Wendt et al. 2000
ICP-MS	5 µBq (8fg)	Kim et al. 1991
TIMS	N/A	N/A

Table 2.3.: Comparison of the ^{99}Tc detection limits of different methods.

^{107}Pd

There is only scarce literature on the methods to measure ^{107}Pd and their limitations. The only nominal value was a ratio $^{107}\mathrm{Pd}/^{106}\mathrm{Pd} = 1\times10^{-8}$ corresponding to 0.2 Bq done by AMS (Korschinek et al. 1994). Radiometric methods are not feasible due to the long half-live of 6.5×10^{6} a.

2.3. Ion Laser InterAction Mass Spectrometry - ILIAMS

The ILIAMS setup suppresses isobaric interferences via non-resonant selective laser photodetachment. A detailed scheme of the ILIAMS system can be found in Fig. 2.4, which is located in an annex to the VERA building. The ILIAMS beam line is directly connected to the low energy beam line of the AMS system of VERA (see Fig. 2.1). A detailed description of the components of the ILIAMS setup can be found in the work of Marek 2018. In 2019, the old laser table was replaced with a new one and in addition to the 532-nm cw-laser a 355-nm pulsed laser, with a repetition rate of up to 300 kHz, was added.

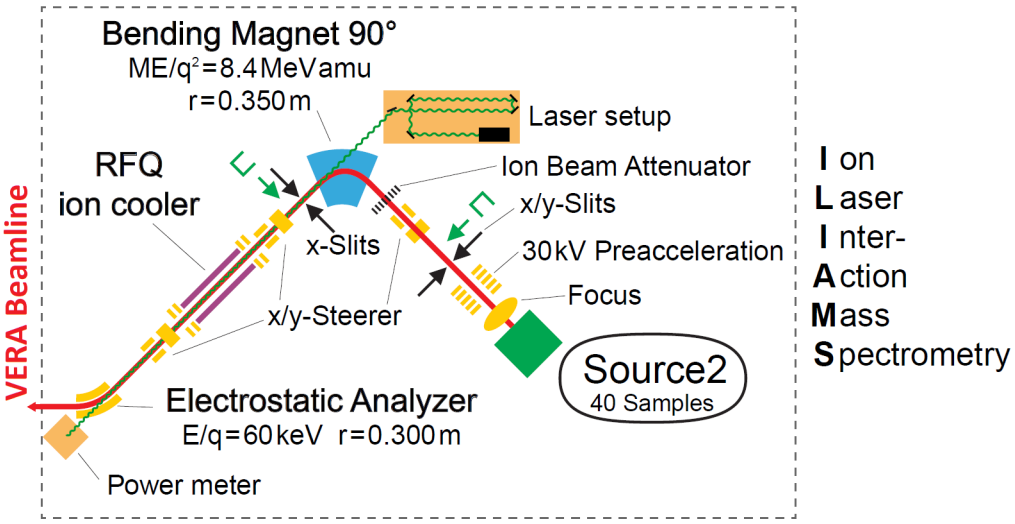

Figure 2.4.: Scheme of the ILIAMS system

Efficient photodetachment relies on the ion beam to have a good overlap with the laser beam and thus the ions have to be confined inside the cooler. To achieve this goal, a linear Paul trap is used, which creates a confining potential for charged particles using an electric quadrupole field alternating at high frequency. In section (2.3.1) a mathematical overview of linear Paul traps is given. More details regarding ion traps can be found in Dawson 1976 and Major et al. 2006.

2.3.1. Mathieu equations and ion motion in the RFQ ion guide

For particle confinement, a potential that creates a restoring force proportional to the radial deviation from the center is needed. This can be realized with a potential of the form:

$$\Phi(t) = \frac{\Phi_0(t)}{r_0^2}(\alpha x^2 + \beta y^2 + \gamma z^2) \tag{2.1}$$

In charge free space, Φ has to satisfy the Laplace equation $\Delta\Phi = 0$. There are two obvious solutions, $\alpha = \beta$ and $\gamma = -2\alpha$ describing the 3-dimensional Paul trap or $\alpha = -\beta$ and $\gamma = 0$ the 2-dimensional trap, which is used for ILIAMS. Such a potential can be created with a setup of four cylindrical electrodes, as shown in Fig. 2.5.

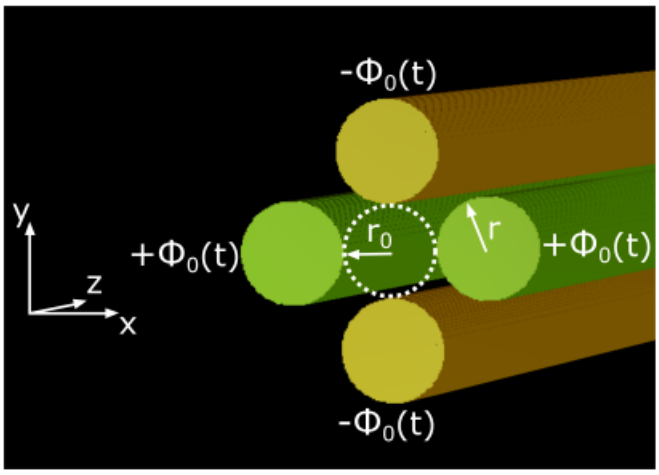

Figure 2.5.: Geometric setup of the RFQ electrodes. The orange and green electrodes are oppositely charged with respect to each other. Picture was taken from (Moreau 2016).

The resulting potential has the form:

$$\Phi(t) = \frac{\Phi_0(t)}{r_0^2}(x^2 - y^2) \tag{2.2}$$

The radius of the circle enclosed by the four electrodes is denoted as r_0. From the equation it is evident that the created force is restoring in one direction, while being repulsive in the orthogonal direction. To achieve a time averaged restoring force in both directions a time dependent potential of the form

$$\Phi_0(t) = U_{\mathrm{DC}} + U_{\mathrm{RF}} \cos \omega_{\mathrm{RF}} \mathrm{t} \tag{2.3}$$

is applied to the electrode pairs. Here $\mathrm{U_{DC}}$ denotes a DC voltage and $\mathrm{U_{RF}}$ the amplitude of an AC voltage with circular frequency ω_{RF}. Deriving the equation of motion for a particle with charge Q and mass m in such a potential and substituting $\tau = \frac{\omega \mathrm{t}}{2}$ ultimately leads to the differential equations

$$\ddot{\mathrm{u}}_{\mathrm{j}}(\tau) + (\mathrm{a_j} - 2\mathrm{q_j} \cos 2\tau)\, \mathrm{u_j}(\tau) = 0 \ , \quad \mathrm{j = x,\ y} \tag{2.4}$$

called Mathieu equations, characterized by the real parameters $\mathrm{a_j}$ and $\mathrm{q_j}$.

$$\mathrm{a_x} = -\mathrm{a_y} = \frac{8\mathrm{QU_{DC}}}{\mathrm{mr_0^2}\omega_{\mathrm{RF}}^2} \qquad \mathrm{q_x} = -\mathrm{q_y} = -\frac{4\mathrm{QU_{RF}}}{\mathrm{mr_0^2}\omega_{\mathrm{RF}}^2} \tag{2.5}$$

For the general discussion of the solutions the subscript j will be dropped. The solutions of the Mathieu equations describe the trajectories of the ions. These solutions can be stable or unstable depending on the values of a and q. Figure 2.6 shows the relevant region of stability for the ILIAMS RFQ ion cooler. Linear Paul traps can be used as mass filters (Paul and Steinwedel 1953), due to the fact that both a and q are dependant on the m/Q ratio of the particles. Operating at $\mathrm{a/q = U_{DC}/U_{RF}} = \mathrm{const}$, only particles with specific m/Q ratios have stable trajectories and can pass the filter. In contrast to quadrupole mass filters, the RFQ ion guide does not need the mass filtering feature and thus no DC voltage ($\mathrm{U_{DC}} = 0 \Rightarrow \mathrm{a} = 0$). Without the contribution of a DC voltage the stability of ion motion inside the cooler only depends on the value of the parameter q. Although theoretically stable trajectories are possible for all $|\mathrm{q}| < 0.908$, experiments show that the ion cooler acts as a weak mass filter allowing only stable trajectories in the region of $0.2 \leq \mathrm{q} \leq 0.8$ (Fig. 2.6).

All stable solutions of equation (2.4) can be expressed as a Fourier series (Major et al. 2006). Considering a 2-dimensional Paul trap $\mathrm{u}(\tau)$ is either x or y.

$$\mathrm{u}(\tau) = \mathrm{A} \sum_{\mathrm{n}=-\infty}^{+\infty} \mathrm{c_{2n}} \cos\left[(\beta + 2\mathrm{n})\tau\right] + \mathrm{B} \sum_{\mathrm{n}=-\infty}^{+\infty} \mathrm{c_{2n}} \sin\left[(\beta + 2\mathrm{n})\tau\right] \tag{2.6}$$

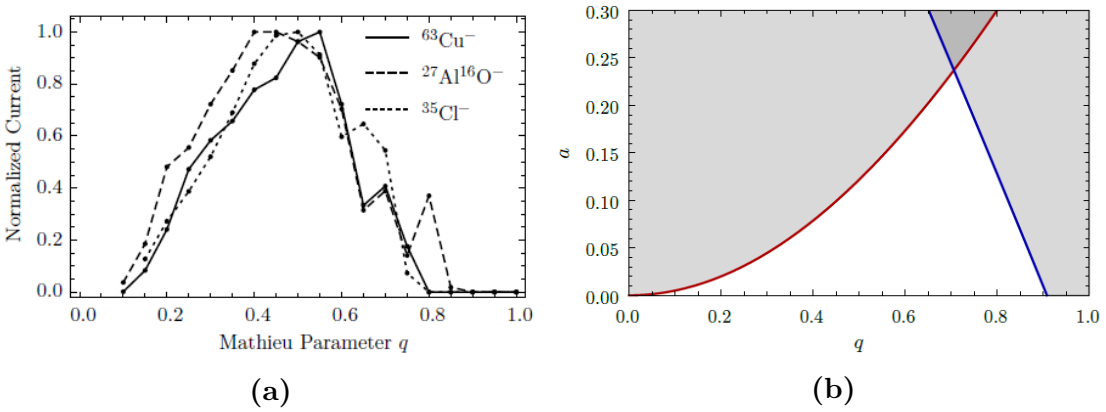

Figure 2.6.: Region of stability of the RFQ ion cooler for (a) measurements and (b) theoretically. The measurements were done with an RF amplitude of 100 V and scanning the RF frequency. Pictures were taken from (Pitters 2015).

A and B are constants depending on the initial conditions, β is the stability parameter and c_{2n} are the amplitudes of the Fourier components. Both β and c_{2n} can be obtained by recursion formulas (Major et al. 2006). The adiabatic approximation is applicable if the amplitude of the field is nearly constant over the oscillation of the particle, which is valid for a,q$\ll$1. In this approximation the stability parameter β simplifies to

$$\beta \approx a + \frac{q^2}{2} \tag{2.7}$$

the coefficients are $c_{2n} \propto q$ and become rapidly smaller for higher increasing n. For a=0 and q<0.6 the ion motion be can described as a micro motion with frequency ω_{RF}, superimposed upon a macro motion that represents harmonic oscillations in a pseudo-potential well

$$\Phi_{pp} = \frac{qU_{RF}}{4r_0^2} r^2 \tag{2.8}$$

of depth

$$D = \frac{qU_{RF}}{4} \tag{2.9}$$

and frequency

$$\Omega = \frac{q}{\sqrt{8}}\omega_{RF} \tag{2.10}$$

(Nieminen et al. 2001, Herfurth et al. 2001, Liu et al. 2002).
The discussed solutions only apply for single charged particles in vacuum and are not entirely true in the presence of space charge or buffer gas inside the ion trap. The maximum amount of trapped particles is limited by the space charge potential of the ions. Ion losses are expected if the space charge potential exceeds the depth of the potential well. Simply increasing the well depth does not work without backlash, since $D \propto q$ (eq. (2.9)) the depth can be increased by increasing q, but the particles oscillation amplitudes c_{2n} also increase with q, generating more losses. The optimal trapped ion density can be reached in the region of $a = 0$ and $q = 0.5$ - 0.6 (Pitters 2015).

2.3.2. Laser Photodetachment

Laser photodetachment describes the process of detaching the weakly bound extra electron (e^-) from an anion (A^-) by means of laser radiation ($h\nu$), resulting in an extra electron and a neutral atom (A). Here h denotes Planck's constant and ν the frequency of the photon.

$$A^- + h\nu \rightarrow A + e^- \tag{2.11}$$

This is the main effect used by ILIAMS to suppress the interfering elemental or molecular isobars against the isotope of interest. The crucial parameter for this technique is the electron affinity (EA) of the elemental or molecular anion entering the RFQ ion guide.
The EA of an atom A is defined as the difference between the total energies (E_{tot}) of the ground states of A and its negative ion A^- (Andersen et al. 1999).

$$EA(A) = E_{tot}(A) - E_{tot}(A^-) \tag{2.12}$$

Within this thesis, only molecular EAs where investigated, since the elemental EAs of the ions of interest are not suited for this technique. The EA of a molecule R

is defined as the transition energy from the ground vibrational/rotational state of the anion ($|R^-, v''=0, J''=0>$) to the ground vibrational/rotational state of the neutral ($|R, v'=0, J'=0>$). (Rienstra-Kiracofe et al. 2002).

$$EA(R) = \Delta E(|R, v' = 0, J' = 0> \leftarrow \ |R^-, v'' = 0, J'' = 0>) \tag{2.13}$$

In Fig. 2.7 a qualitative diagram of the potential energy surfaces for a molecular anion R^- and its neutral state R is given. Occasionally the EA associated with the (0,0) band can not be identified by experimental methods. In such cases the „vertical attachment energy“ (VAE) and „vertical detachment energy“ (VDE) provide lower and upper boundaries, respectively, for the EA (Rienstra-Kiracofe et al. 2002). A physical interpretation of the VAE is the energy released from the near-instantaneous addition of an electron to a neutral molecule, whereas the VDE is the energy required for the near-instantaneous removal of an electron from an anion.

The cross section behavior of laser photodetachment processes near threshold energy is described by the Wigner law (Wigner 1948):

$$\sigma \propto k^{2l+1} \tag{2.14}$$

Here k denotes the linear momentum and l the angular momentum of the outgoing electron. Equation (2.14) can be rewritten in terms of threshold energy, that relates to the electron affinity (EA), and photon energy (E_γ) (Forstner et al. 2015):

$$\sigma(E_\gamma) \begin{cases} \propto (E_\gamma - EA)^{l+\frac{1}{2}} & \text{for } E_\gamma \geq EA \\ = 0 & \text{for } E_\gamma < EA \end{cases} \tag{2.15}$$

Looking at equation (2.15) one can see that using laser photodetachment to suppress isobars is applicable if the EAs of unwanted isobars are smaller than the EA of the isotope of interest. Only in this case it is possible to choose the photon energy such that the electrons of interfering isobars are detached while leaving the isotope of interest unaffected (Fig. 2.8).

When interacting with laser light, the number of ions lost due to laser photodetachment, in dependence on the interaction time t, is described by

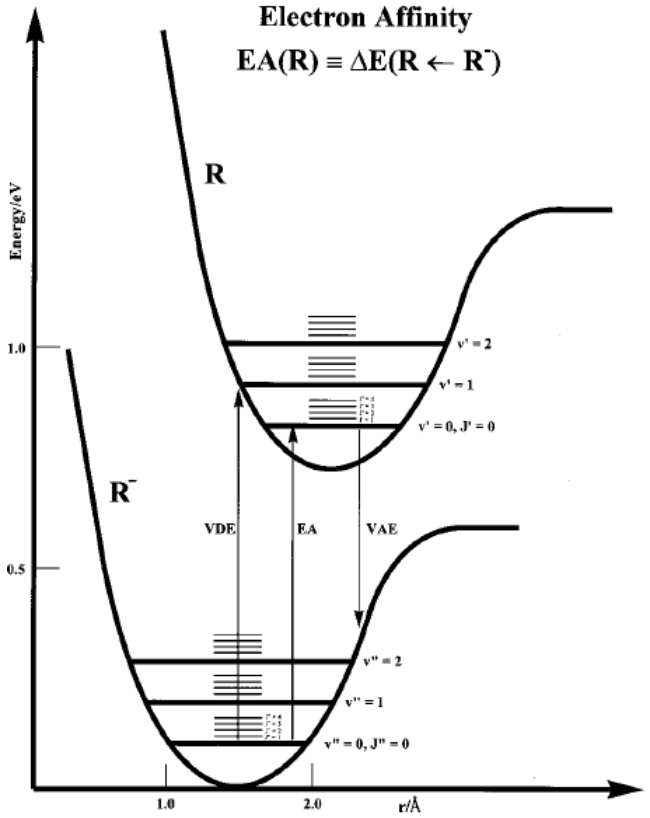

Figure 2.7.: Qualitative diagram of the potential energy surfaces for a molecular anion R^- and its neutral state R. Transitions shown represent the VDE, EA and the VAE. Picture was taken from (Rienstra-Kiracofe et al. 2002)

$$N(t) = N(0)e^{-\sigma\Phi t} \tag{2.16}$$

where σ is the cross section and Φ the photon flux. Typical cross sections for laser photodetachment are on the order of $10^{-17}\,cm^2$ and commercially available cw-lasers have photon fluxes between 10^{20} to $10^{21}\,cm^{-2}\,s^{-1}$.

For AMS near complete isobar suppression is preferred and thus the interaction time between the ions and the laser beam should at least be on the order of several hundreds of μs (Martschini et al. 2017). This can only be achieved by deceleration of the keV ions down to thermal energy, since laser overlaps with keV ions would require hundreds of meters of beam line. First attempts on slowing down anions to thermal energies were done with gas-filled RFQ ion beam coolers (Liu et al. 2002,

Zhou et al. 2002, Liu et al. 2007) and with this technique isobar suppressions of more than four orders of magnitude were reached with stable isotopes (Andersson et al. 2010).

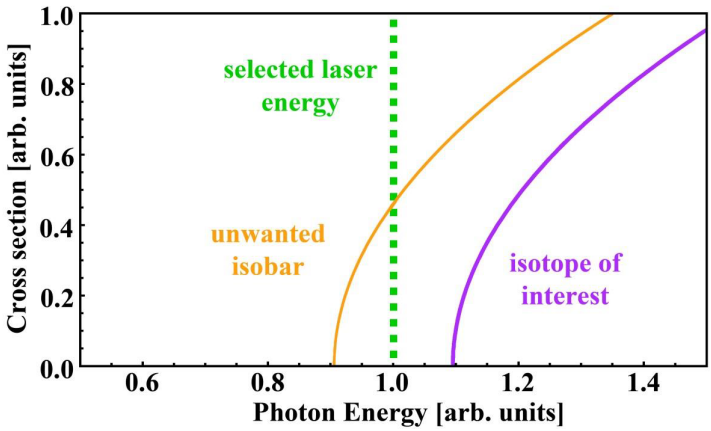

Figure 2.8.: Indicative photodetachment cross-sections of the isotope of interest (purple) and an unwanted isobar (orange) versus the photon energy (green) is shown. By choosing a suitable photon energy it is possible to only detach the electron of the interfering isobar while leaving the isotope of interest unaffected. Picture is based on (Forstner et al. 2015)

2.3.3. Buffer gas cooling and ion residence times

Taking a look at Fig. 2.4 it is notable that after the extraction of usually 30-keV anions from the ion source the 90° bending magnet is the first filtering device, letting only ions of specific p/q ratios enter the RFQ ion beam cooler. In principle the ion cooler is a linear Paul trap, as explained in section 2.3.1, but as mentioned before the ions have to be decelerated to thermal energies. After electrostatic deceleration of the anions to typically tens of eV, buffer gas cooling is used in order to reach sufficiently long laser interaction times. For this purpose, the RFQ volume is filled with a light gas (e.g. He) or a gas mixture (e.g. $He+O_2$).
Buffer gas cooling was developed with positively charged ions, whereas the negatively charged ions extracted from the ion source at VERA impose certain constraints. The weakly bound extra electron of anions is lost by collisional detachment with the buffer gas if the collision energy in the center of mass frame exceeds

the EA. This corresponds to the threshold energy for detachment (Pitters 2015). Hence the ions are decelerated electrostatically, before colliding with the buffer gas. A system of aperture lenses on the entrance side of the cooler ensures proper focusing of the ion beam into the 3 mm cooler aperture. Four so-called guide electrodes are placed symmetrically between the RFQ rods. The guiding electrodes are slightly tilted in order to produce a longitudinal field gradient, with a typical guiding field strength of 10 V/m, causing a preferred direction of movement towards the end of the cooler. The distance of the guide electrodes from the axis changes by 0.5 mm between the two ends, corresponding to a tilt of 0.036 ° (Pitters 2015). At the end of the RFQ cooler, the ions are re-accelerated again to 30 keV. Turbo molecular pumps with He pumping powers of 1270 l/s and 650 l/s, respectively, efficiently remove the buffer gas from the beam line volume around the cooler tube in a differential pumping system, where the aperture lenses act as pumping barriers towards adjacent beam line sections. A schematic drawing of the RFQ ion cooler can be seen in Fig. 2.9.

According to Pitters 2015, a small energy transfer per collision is favorable for the injection as well as the buffer gas cooling process. To minimize the energy transfer per collision, the buffer gas has to be as light as possible, but not chemically reactive with the isotope of interest. The electrostatically decelerated ions lose further energy through elastic collisions with the neutral gas atoms, gathering in the minimum of the trapping potential. Simulations done by Pitters 2015 result in a mean kinetic energy of the trapped ions of 0.08(2) eV and that, once the ions reach equilibrium, they are confined to the trap center within 0.5 mm. The simulated residence times are on the order of ms.

The aim of the whole RFQ ion guide setup is to increase the residence time of the confined ions into the ms range to enable sufficient isobar suppression by laser photodetachment. First experimental measurements on the residence time were done by Moreau 2016. He investigated the influence of the following parameters on the ion residence time: injected current, buffer gas pressure and guiding field strength. The relevant results are shown in Fig. 2.10. Increasing residence times are observed by decreasing injection current, increasing buffer gas pressure and decreasing guiding field strength. While the buffer gas pressure and the guiding

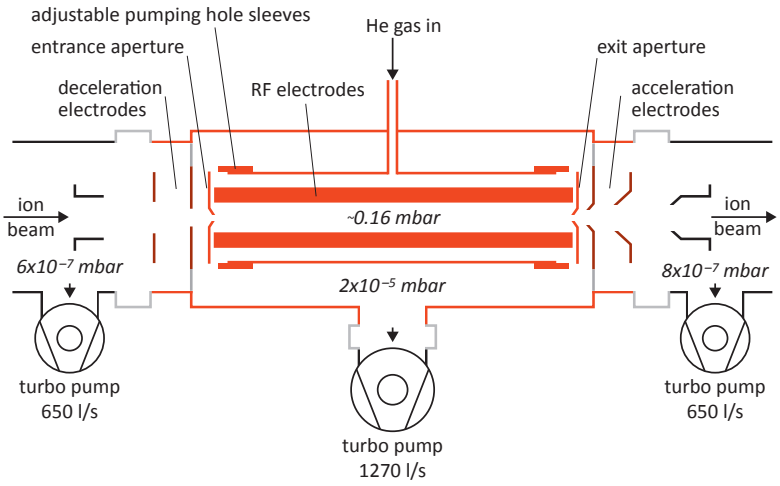

Figure 2.9.: Schematic drawing of the ILIAMS RFQ ion cooler. The red section is on cooler high voltage, insulated from the rest of the beam line by ceramic insulators indicated in light gray. Picture was taken from (Martschini et al. 2017)

field strength only cause slight changes in the residence time, the injected current has a much stronger impact. It seems that for higher currents, a field gradient is built up by the accumulated space charge, resulting in much shorter residence times (Moreau 2016). Between the current values 32 pA and 460 nA the most likely residence time changes more than an order of magnitude from 7 ms to 0.4 ms.

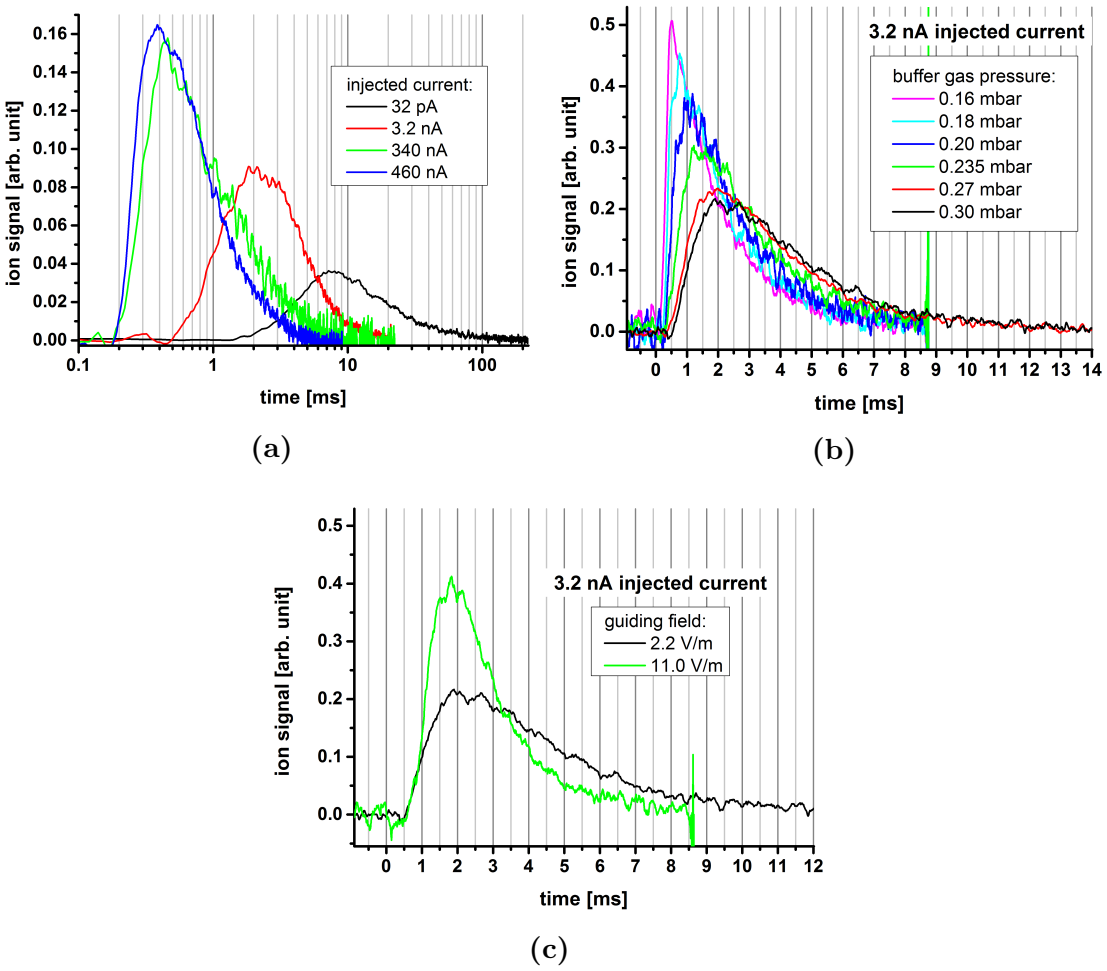

Figure 2.10.: Ion residence time distribution dependency from (a) injected current, (b) cooler pressure and (c) guiding field strength. Pictures were taken from (Moreau 2016).

3. Measurements and results for ^{90}Sr

This chapter will give an overview of the results for ^{90}Sr gained throughout the beam times from September 2018 to July 2019. This includes the measurements to find a suitable molecular anion system for laser photodetachment, tests of the ion beam transmissions through the ion cooler and the accelerator and results of first AMS measurements.

3.1. Search for a suitable molecular system

Since the electron affinity (EA) of Sr^- of (52.06 ± 0.06) meV (Andersen et al. 1997) is smaller than the EAs of its isobars, it is not possible to use laser photodetachment with elemental strontium (c.f. Tab. 3.1.1). Hence, a molecular anion of Sr with suitable EA, with respect to the isobaric EAs, has to be found and used for AMS measurements here at VERA. At the beginning of my work on ^{90}Sr it was already clear that the molecule SrF_3^- not only fulfills these requirements, but the literature also strongly suggests using SrF_3^-, since no other fluorides form (Zhao et al. 2010) and Sr^- is no prolific anion either. Thus no other fluoride or oxide molecules were investigated.

3.1.1. Isobaric background

There exist two atomic isobars interfering in measurements of ^{90}Sr, which are the stable ^{90}Zr with a natural abundance of 51.45 % and the unstable β^- emitter ^{90}Y with a half-life of $T_{1/2} = 64$ h. Their positions on the nuclide chart can be seen in Fig. 3.1.

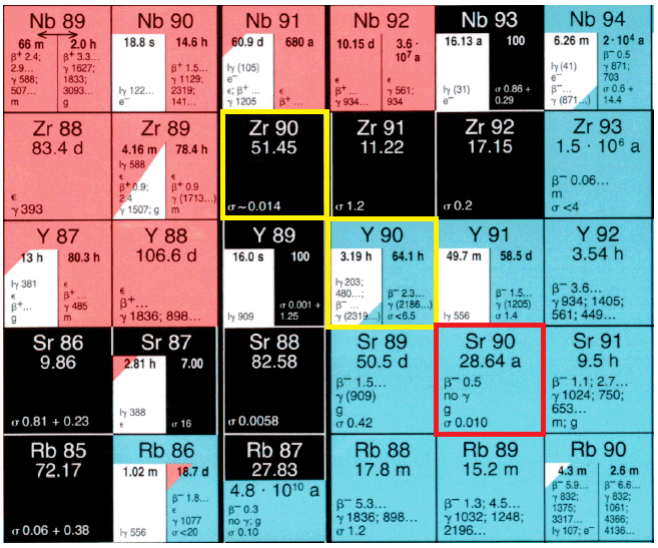

Figure 3.1.: Nuclide chart around mass 90 amu. The isotope of interest is marked in red and the interfering isobars are marked in yellow. Picture was taken from *Karlsruher Nuklidkarte, 7th edition.*

The elemental EAs (i.e. Sr, Y and Zr) and the known EA limits for the SrF_3^-, YF_3^- and ZrF_3^- molecules are listed in Tab. 3.1. It clearly shows why elemental anions, due to their EAs, can not be used for laser photodetachment. On the other hand SrF_3^- is considered a superhalogen (Eliades et al. 2015), thus should have a very high EA, while the EAs of the isobaric molecules are expected to be lower. The wavelength of the 532 nm laser corresponds to a photon energy of 2.33 eV. Hence it is possible to detach the electrons of the isobaric molecules YF_3^- and ZrF_3^-, while leaving the molecule SrF_3^- unaffected.

anion	EA (eV)	reference
Sr^-	0.05206 ± 0.00006	Andersen et al. 1997
Y^-	0.308 ± 0.012	Feigerle et al. 1981a
Zr^-	0.427 ± 0.014	Feigerle et al. 1981b
SrF_3^-	>3.6	Eliades et al. 2015
YF_3^-	<2.3	Eliades et al. 2015
ZrF_3^-	<2.3	Eliades et al. 2015

Table 3.1.: List of electron affinities and limits for the anions Sr^-, Y^-, Zr^-, SrF_3^-, YF_3^- and ZrF_3^-.

3.1.2. Molecule formation within the ion source

An important part of the research involves investigations of the efficiency of molecule formation in the ion source during the sputtering process. This was done by mass scans of samples with different sample matrices, recording the ion current with Faraday cup (FC) FC I1-1 behind the 90° bending magnet BM I1-1 (see Fig. 3.7). Evaluation of the mass scans shows which of the matrices is best suited for AMS samples and also how the isobar formation behaves in certain matrices. Tab. 3.2 lists the matrices used in this study.

sample matrix	**mass-ratio**
SrF_2 + PbF_2	1:3
SrF_2 + PbF_2	1:8
SrF_2 + YF_3 + PbF_2	1:1:1
ZrF_4 + PbF_2	1:1
SrF_2 + ZrF_4 + PbF_2	1:1:1

Table 3.2.: Used matrices during mass scans to investigate the molecule formation within the ion source.

All mass scans were evaluated the same way. At first, the scan was mass calibrated, done with easily identifiable and abundant peaks. Those are typically the formed fluorides of the isotope of interest in the sample (e.g. $^{88}SrF_x^-$, $^{90}ZrF_x^-$), copper molecules (e.g. $^{x}Cu_3^-$, $^{x}CuF_x^-$) and the $^{133}CsF_2^-$ peak. Every scan covered the same mass range. The magnetic field of the bending magnet was varied by changing the current from 87 A to 145 A, corresponding to a scanned mass range of 80 to 205 amu. An examplary mass scan is shown in Fig. 3.2.

The final results of the mass scan measurements are shown in Fig. 3.3. The distribution of fluoride formation, by Zhao et al. 2010 was always a good guideline, although it was never possible to exactly reproduce their results.
Our results show that ZrF_3^- as well as YF_3^- have very low yields for the tri-fluorides, namely 2 % and 16 % respectively, in comparison to SrF_3^-, which almost exclusively forms it. Therefore, extracting SrF_3^- out of the ion source already provides isobar suppression. According to Eliades et al. 2013, the isobar suppression relative to the SrF_3^- yield can reach up to 10^{-5} for both ZrF_3^- and YF_3^-, but here we typically achieved factors around 5×10^{-3} and 5×10^{-2}, respectively.

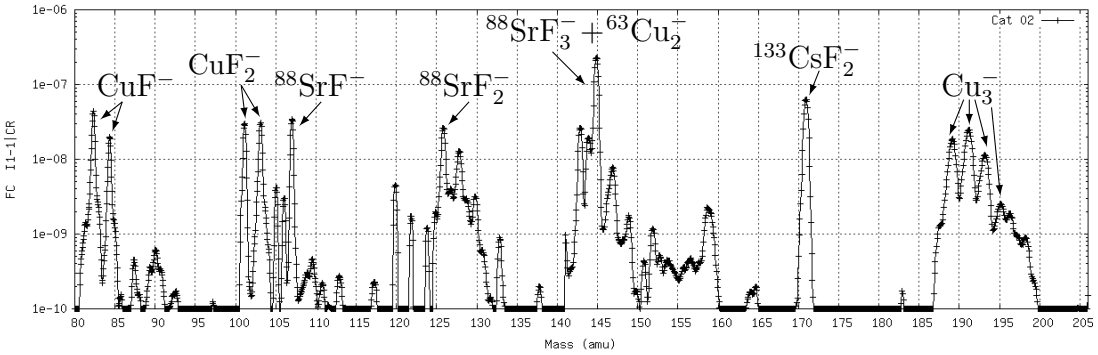

Figure 3.2.: Exemplary mass scan of the SrF_2 + PbF_2 matrix into FC I1-1 to investigate the dependancy of molecule formation within the ion source on the sputter matrix.

For strontium the preferable mixing-ratio of SrF_2 and PbF_2 turned out to be the 1:8 ratio by weight (see Fig. 3.3 (a)). The higher admixing of PbF_2 leads to an even higher SrF_3^- anion fraction of almost 90 % of the total current and thus fewer losses due to SrF^- and SrF_2^- formation, which is in good agreement with the literature (Zhao et al. 2010). This could be explained by the fact that the 1:3 mixing-ratio provides less fluorine inside the ion source favoring the formation of lower fluorides.

3.1.3. Ionization yield

To find out how much of the Sr contained inside a target forms the molecule SrF_3^- and thus how much is lost otherwise in the ion source or to other anions than SrF_3^-, the so-called ionization yield for SrF_3^- is measured.
For the ionization yield it is necessary to know the amount of strontium in the targets. This is done by weighing the exact amounts of SrF_2 and PbF_2 before mixing them together to form the sample matrix. Afterwards the amount of matrix material inside the targets is determined by the difference in weight of the empty cathode plus the used pin and the weight of the pressed cathode. The amount of stable ^{88}Sr inside the targets is then easily calculated with the knowledge of exact mixing-ratio, the amount of matrix material inside the target and the natural abundance of ^{88}Sr (see Appendix B). This could in principle be done with every stable strontium isotope, but since ^{88}Sr is the most abundant with 82.58 % it is the best choice. The properties of the targets used for the measurement are summarized in Tab. 3.3.

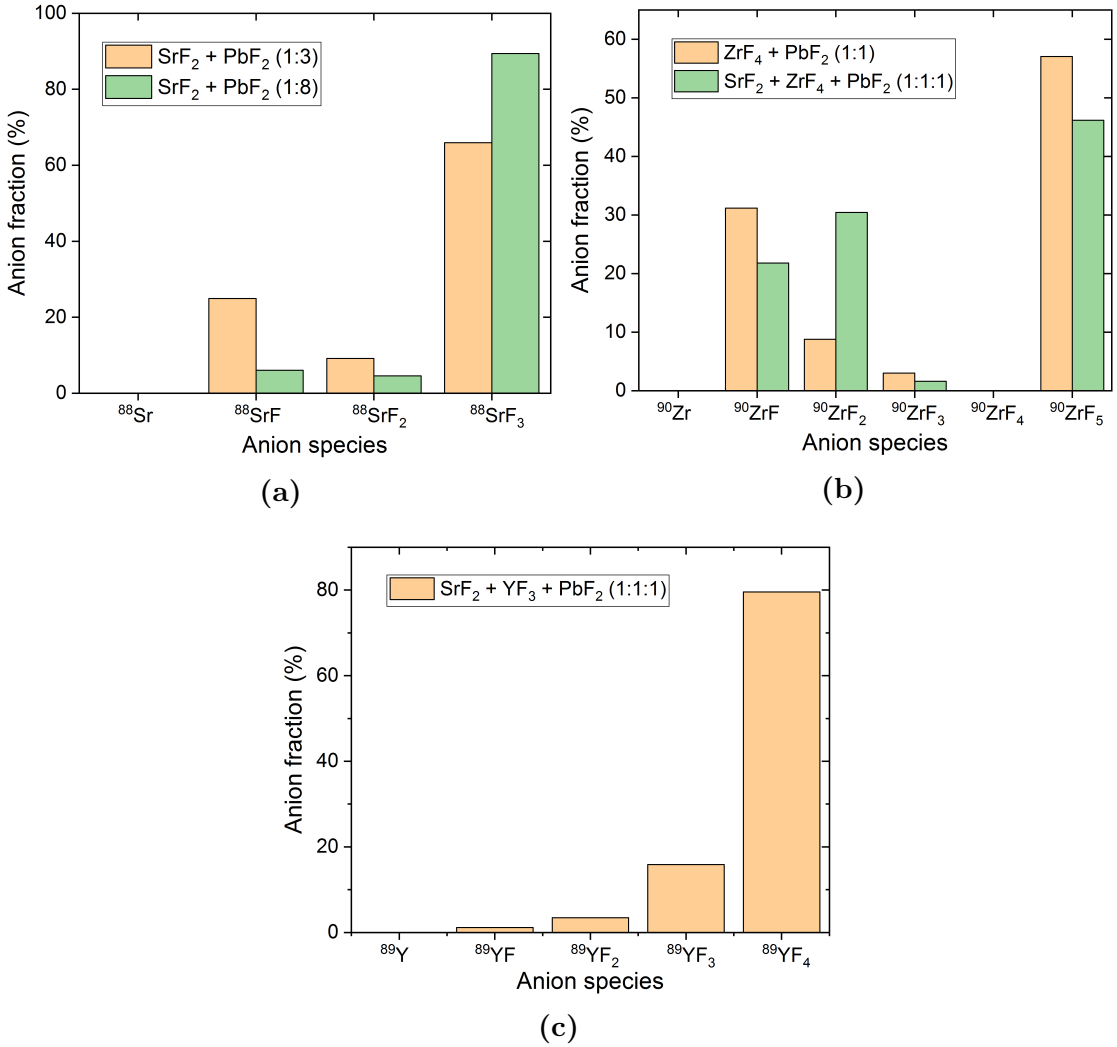

Figure 3.3.: Results of the mass scans for (a) Sr, (b) Zr and (c) Y. The empty columns correspond to no formation or formation below the Faraday cup threshold of 100 pA. The diagrams are normalized to the total current output of all detected molecules represented in the diagrams.

Besides the ionization yield of SrF_3^- itself, the yield was also measured for different mixing-ratios of the sample matrices. This was done because the molecule formation mass scans, done prior to the ionization yield, suggest that the 1:8 mixing-ratio should have a higher SrF_3^- ionization yield, since less Sr atoms are lost in the ion source due to the formation of SrF^- and SrF_2^- (see Fig. 3.3 (a)).

SrF_2:PbF_2 ratio	**matrix weight (mg)**	**content of SrF_2 (mg)**
1:8	3.06 ± 0.02	0.342 ± 0.002
1:8	2.82 ± 0.02	0.315 ± 0.002
1:8	2.71 ± 0.02	0.303 ± 0.002
1:8	0.92 ± 0.02	0.103 ± 0.002
1:8	1.64 ± 0.02	0.183 ± 0.002
1:8	1.37 ± 0.02	0.153 ± 0.002
1:3	1.26 ± 0.02	0.314 ± 0.005
1:3	1.34 ± 0.02	0.334 ± 0.005
1:3	1.11 ± 0.02	0.277 ± 0.005

Table 3.3.: Properties of the measured cathodes for the ionization yields of SrF_3^- and SrF^-. The exact SrF_2:PbF_2 mixing-ratios are 1:7.958 and 1:3.012.

The measurement itself runs automatically, needing only minimal tuning beforehand, and in principle are continuous mass scans measured in the FC I1-1. In contrast to the mass scans done in section 3.1.2, this time the magnet is set on a constant magnetic field and the high voltage of the ion source, thus the anion energy, is changed. Sr acts as an ionizer poison which can be overcome by sputtering carbon targets to regenerate the ionizer. This was done during the measurement by placing carbon targets in-between sets of three Sr targets. To calculate the ionization yield correctly, the whole material has to be sputtered out of the cathodes, hence the targets should not contain too much material to keep the sputter duration reasonably short. The evaluation of the yield measurements is discussed in detail in Appendix B.

Fig. 3.4 shows the ionization yields ((a) & (b)) as well as the current profiles ((c) & (d)) plotted against the sputter duration. The current profiles show a typical trend for fluorides, they start at high currents and fall off pretty quickly. At around 1.5 h there is a sudden rise in current, because the measurement had to be interrupted for roughly an hour while sputtering a carbon target in the downtime refreshing the ionizer. The measurements show that the 1:8 mixing-ratio targets reach higher ionization yields for SrF_3^- and lower SrF^- ionization yields. This fits well with the expectations from the mass scan results of Fig. 3.3. Within the first hour of sputtering, the SrF_3^- ionization yield of the 1:8 mixing-ratio reaches 0.6 %

and in total around 0.9 %. This result shows that for ^{90}Sr AMS measurements it is best to use SrF_2:PbF_2-ratios of 1:8 and extract SrF_3^- from the ion source.

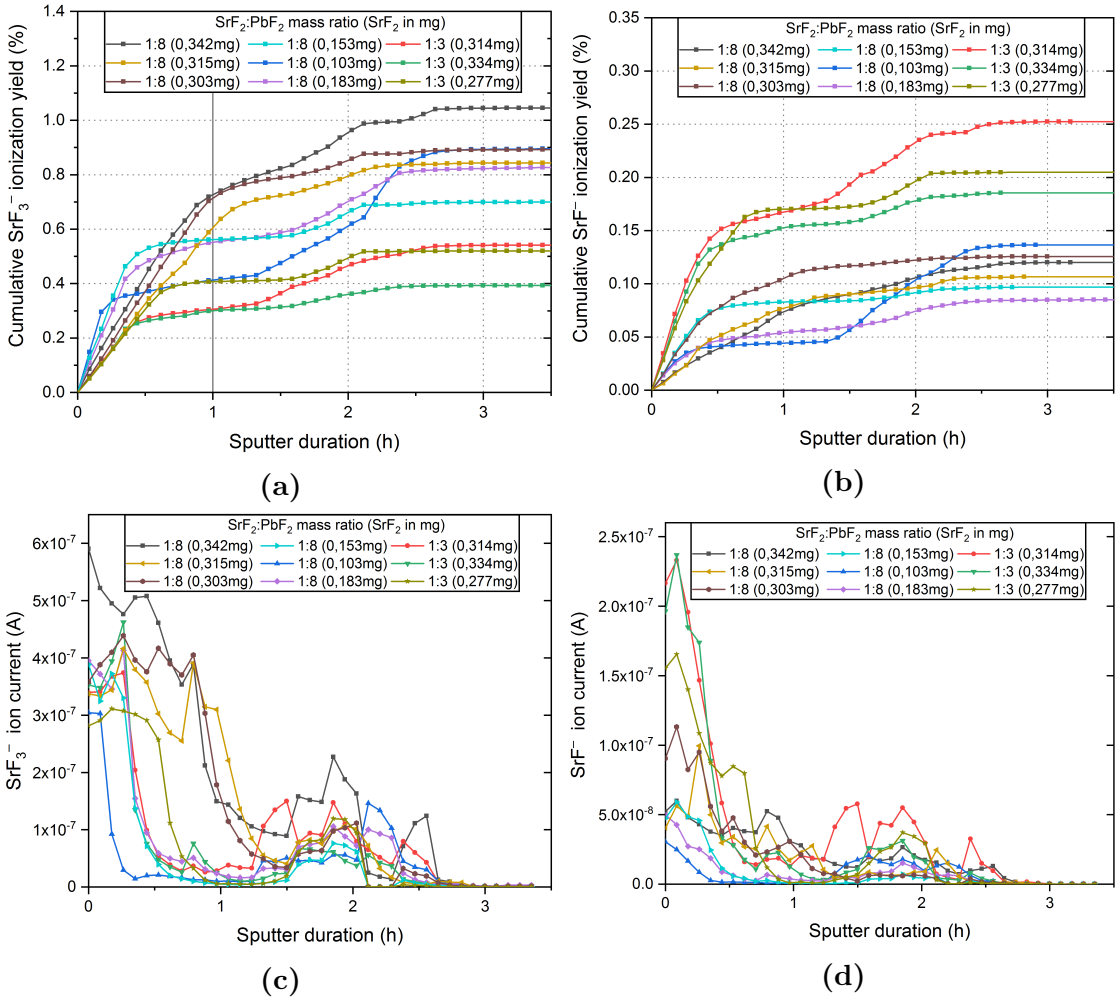

Figure 3.4.: Results of the ionization yield measurements. The graphs show the cumulative yield of SrF_3^- (a), SrF^- (b), SrF_3^- ion current trend (c) and SrF^- ion current trend (d) all as a function of the sputter duration on the individual target. Lines without symbols indicate that the target was sputtered to exhaustion and did not give any more current above 100 pA

3.1.4. Investigation of isobar suppression

Isobar suppression with ILIAMS

In section 3.1.1 it was already mentioned that the isobars of ^{90}Sr are ^{90}Y and ^{90}Zr and that the elemental EAs are not suitable for laser photodetachment, but one has to use tri-fluoride molecules instead (see Tab. 3.1).
To measure the isobar suppression with ILIAMS the ion beam has to be guided through the whole beam line into the gas ionization chamber (GIC) detector in the section L4 (Fig. 3.7). The GIC-detector is a compact gas ionization chamber with two separate anodes. Without laser, the position of $^{90}Zr^{3+}$ in the energy loss spectrum of the detector is determined and its count rate is measured. Afterwards, the count rate of $^{90}Zr^{3+}$ is measured with the laser switched on and the suppression factor (S) is calculated with eq. (3.1).

$$S = \frac{r_{\text{Laser off}}}{r_{\text{Laser on}}} \cdot T_{\text{cooler}} \tag{3.1}$$

Here r denotes the count rates in the detector and T_{cooler} is the transmission of strontium through the ion cooler. This was also done with different gas pressures in the RFQ ion guide to check whether the gas pressure itself has a significant effect on the suppression factor or not.
The important isobar to get near complete suppression is ^{90}Zr, because it is stable and highly abundant at 51.45 %, while ^{90}Y concentrations in strontium samples are negligibly small compared to ^{90}Zr due to the fact that in secular equilibrium the $^{90}Y/^{90}Sr$ ratio reaches only as high as 2×10^{-4} (Eliades et al. 2013). In comparison, the $^{90}Zr/^{90}Sr$ ratio results in roughly 5×10^{4}, assuming a cathode filled with 10 mg of SrF_2+PbF_2 mixed 1:8 by weight, a $^{90}Sr/Sr$ ratio of 1×10^{-11} and a zirconium contamination of 1 ppm. In Tab. 3.4 the values of the suppression factors for ^{90}Zr with different ILIAMS settings, at a buffer gas pressure of 0.30 mbar, can be found. For these suppression tests Zr-spiked material was used, where additional ZrF_4 was mixed to the SrF_2+PbF_2 matrix to ensure high Zr content. The mixing-ratio of the Zr-spiked sample matrix was SrF_2:ZrF_4:PbF_2 1:1:1 by weight Two different buffer gases were tested. One was pure He and the other one was a mixture of He+O_2 roughly mixed 30:1 (He : O_2). It turned out that He+O_2 is the better buffer

gas, because the mixture alone already yields a great suppression factor for ^{90}Zr of around 5×10^5 and with the addition of the 532-nm laser a suppression factor of $>10^7$ is reached. The results show that using the 355-nm laser only results in a slight improvement of the suppression factor, making the choice of laser not as relevant.
The other isobar ^{90}Y also gets suppressed by several orders of magnitude, but has not been investigated as detailed as ^{90}Zr. The He+O_2 buffer gas at 0.30 mbar results in a suppression factor of $>1.5\times10^3$, under the assumption that the lowest detectable current is 10 pA, making it undetectable in our Faraday cups. Going down to low buffer gas pressures of 0.18 mbar results in measurable YF_3^- currents after the ion cooler, but the current is immediately lost while ramping up the power of the 532-nm laser, corresponding to a suppression factor of $>7\times10^1$. Thus additional ^{90}Y suppression is provided by the laser.

method	**suppression factor**
He + 532 nm laser	3×10^6
He + O_2	5×10^5
He + O_2 + 532 nm laser	1×10^7
He + O_2 + 355 nm laser	2×10^7

Table 3.4.: Experimental ^{90}Zr suppression factors with different ILIAMS settings. The lasers were operated at 10 W and the buffer gas pressure was set to 0.30 mbar.

In Fig. 3.5 the count rates of Zr-spiked targets and of ^{88}Sr are plotted against the RFQ buffer gas pressure for both, He and He+O_2. It shows that Zr can be suppressed up to 2 orders of magnitude by changing the buffer gas pressure from 0.20 mbar up to 0.30 mbar, whereas the ^{88}Sr count rates are unaffected by both, the buffer gas pressure and the laser.

Isobar suppression with the detector

The used detector is a compact gas ionization chamber (GIC) with two separate anodes, to allow isobar separation by differential energy loss measurement. The stopping power is proportional to the proton number (Z), meaning that ions with higher Z have a higher energy loss in the first part of the detector. Thus, a higher signal will be detected on the first anode compared to the signal of the residual

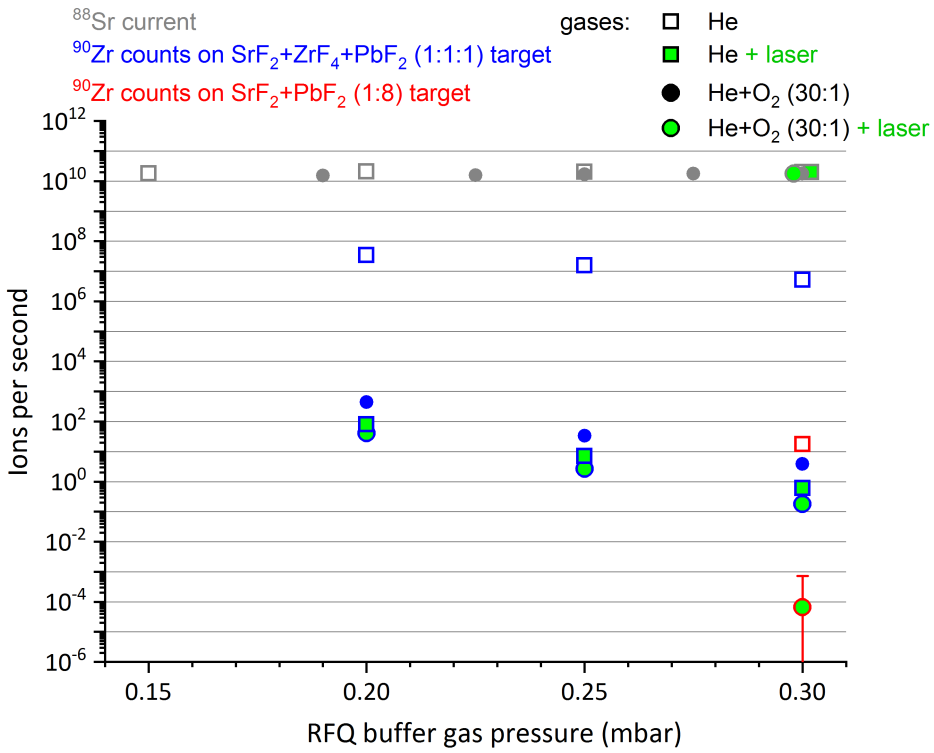

Figure 3.5.: Picture of the Zr count rates against the RFQ buffer gas pressure with and without laser. It shows the tested buffer gases He (squares) and $He+O_2$ (circles). ^{88}Sr is neither effected by the buffer gas nor the laser

energy on the second anode. This effect is helpful to distinguish between different elements that enter the detector with the same energy.

In this respect, Sr is a rather favorable case, because the relevant isobar ^{90}Zr (Z=40) has a bigger Z than the trace isotope ^{90}Sr (Z=38). Therefore the two isotopes are not only rather well separated in the detector, but due to the fact that Sr has the smaller Z it is not located in the tail of scattered $^{90}Zr^{3+}$ particles in a 2D energy loss spectrum, i.e. energy loss on anode 1 vs anode 2. During the measurements of $^{90}Sr^{3+}$ the separation of the two isobars $^{90}Sr^{3+}$ and $^{90}Zr^{3+}$ in the detector spectra is clearly visible, but the distance distance between the centers of the two peaks varies between measurements. Nonetheless the region of interest (ROI) typically includes more than 50 % of the ^{90}Sr events. In Fig. 3.6 a spectrum with good isobar separation in the detector can be seen.

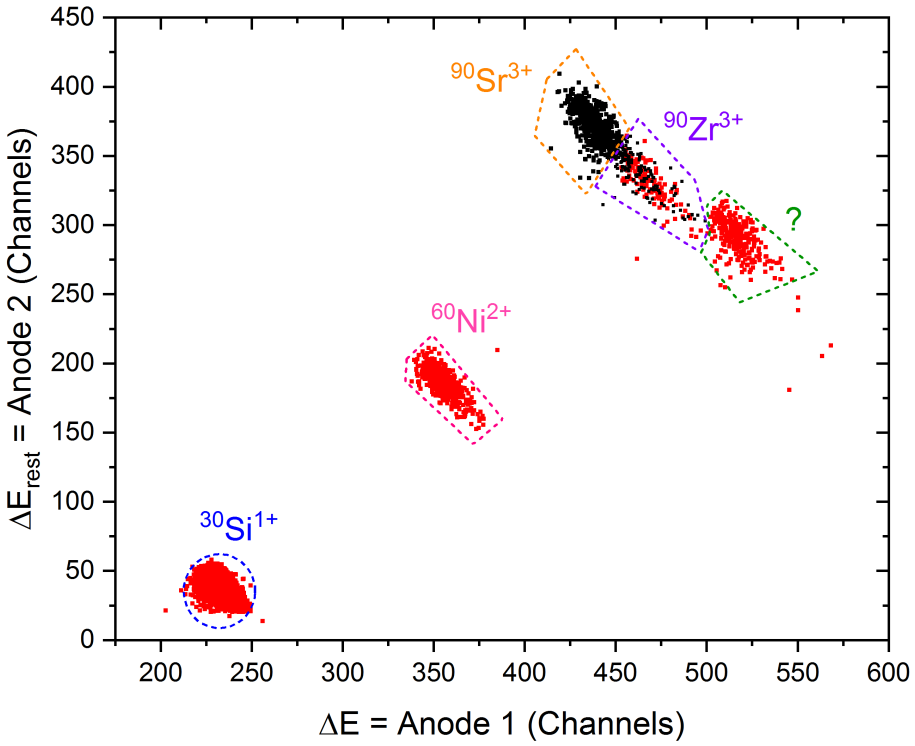

Figure 3.6.: Isobar separation of $^{90}Sr^{3+}$ and $^{90}Zr^{3+}$ inside the GIC-detector. The different isotopes and their ROI in the detector are marked and labeled accordingly. It contains the $^{90}Sr^{3+}$ events of one run (black) and all events of a Zr-spiked run (red) from the beam time Sr1907. One channel corresponds to roughly 13.5 keV.

The $^{90}Sr^{3+}$ particles with energies around 10.89 MeV enter the GIC-detector, which is filled with isobutane gas at pressures of 50 - 55 mbar. Zr-spiked targets are used to monitor the detector separation between $^{90}Sr^{3+}$ and $^{90}Zr^{3+}$, as well as for a Zr proportional correction factor. This is needed if the sputter targets Zr contamination is too high, such that $^{90}Zr^{3+}$ events lie within the set $^{90}Sr^{3+}$ ROI. Typical $^{90}Zr^{3+}$ count rates on Zr-spiked targets are between 20 - 80 cps with laser and up to 10^4 cps without laser. For $^{90}Sr^{3+}$, which is unaffected by the laser, typical count rates are 0.2 - 0.8 cps for a standard with $^{90}Sr/Sr = 1.09 \times 10^{-11}$. The Zr suppression factor in the detector can reach up to 10^3.
Events of $^{30}Si^{1+}$ and $^{60}Ni^{2+}$ isotopes can be found in the detector spectra, because they have the same m/q ratio as $^{90}Sr^{3+}$ and seem to be contained to some extent in our sputter materials. Until now it was not possible to identify the events located in the green ROI.

3.2. AMS measurements and performances

This section is dedicated to the AMS measurement routine and performance tests done for ^{90}Sr. It features the performance tests, i.e. transmissions and detection efficiency, as well as the tuning procedure and the typical ^{90}Sr measurement routine. All components and their locations at VERA, important for this section (e.g. Faraday Cups), are shown in Fig. 3.7. The stripper gas pressures correspond to the pressure measured by the ionization gauge IGC 03-1 located at the end of the accelerator tube. For He, it is roughly 9×10^6 lower than the actual stripper pressure (Steier et al. 2019). This empirical factor should be taken with caution.

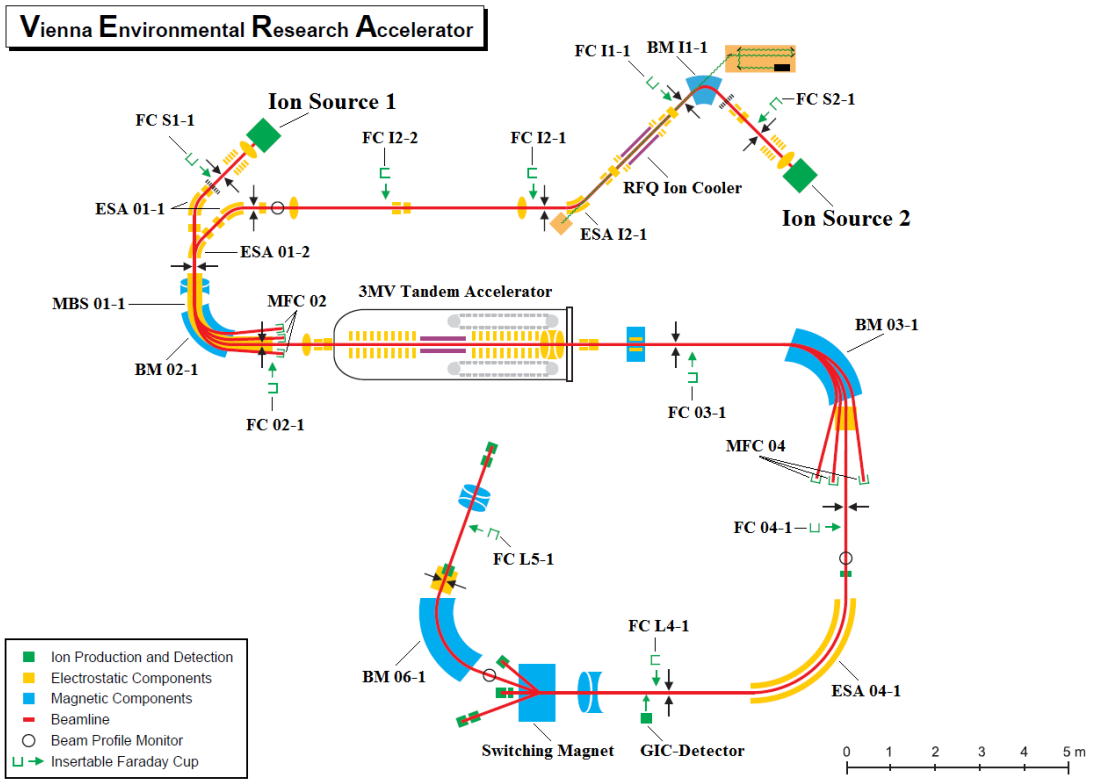

Figure 3.7.: Sketch of VERA with all Faraday cups (FC), electrostatic analyzers (ESA), bending magnets (BM) and other important components labeled with their respective section names. The offset FCs are labeled as MFC.

3.2.1. Ion cooler transmission

The first Faraday cups (FC) after the ion cooler are FC I2-1 and FC I2-2, but according to Marek 2018 their reading can not be trusted and thus for monitoring the ion cooler transmission MFC 02-1 has to be used. The problems with these two FCs is that without a m/q-filter it is not clear which ions are extracted and FC I2-1 also does not read accurately. Another problem is that FC I2-2 is rather small, such that it might be missed by parts of the ion beam when tuned for accelerator injection and thus not all of the SrF_3^- is measured. The transmission through the ion cooler (T_{cooler}) can be calculated as

$$T_{cooler} = \frac{I_{MFC\ 02\text{-}1}}{I_{FC\ I1\text{-}1}} \tag{3.2}$$

where I denotes the measured current in the corresponding FC. At both FCs the ion charge state is -1. The buffer gas pressure inside the ion cooler has no significant effect on the transmission of SrF_3^- in the range of 0.20 - 0.30 mbar (see Fig. 3.5).

The ion cooler transmission plotted against the injected current can be seen in Fig. 3.8. It shows the transmission for two different tuning setups of the same measurement, where the second setup (Tune B) was a big improvement compared to the first setup (Tune A) in terms of ion cooler transmission. The first setup reached an average transmission of 20 %, while the average transmission of the second setup is 35 %. Despite the differences in the absolute transmission, the transmission drops for both setups if the injected current is above 250 nA. This might be due to the fact that at higher injected currents more losses are to be expected because of space charge effects (Moreau 2016).
From other beam times it was also discovered that when the current is $\geq$500 nA the ion cooler transmission does not exceed 10 %, even when lowering the injected current with a 60-fold attenuator. At those high currents it seems that the phase space of the ion beam emitted by the ion source is too big to entirely fit through the 3 mm aperture of the ion cooler. The space charge accumulated in the ion source is high due to $>$30 µA of $^{19}F^-$ current, which is a general challenge for fluoride measurements.

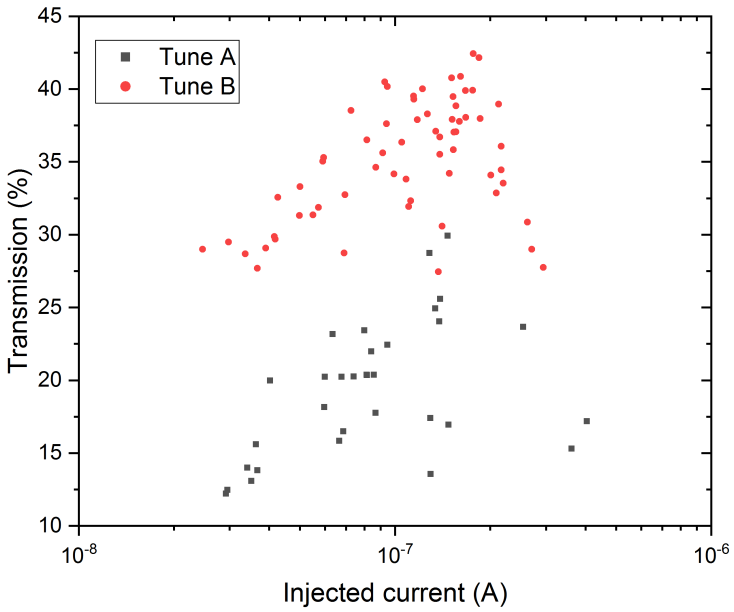

Figure 3.8.: Ion cooler transmission as a function of the injected current for two different tuning setups from the measurement Sr1901. Each data point correspond to the average of the three sequences of a run.

3.2.2. Accelerator transmission and charge state yield

The first FC after the accelerator has no m/q filtering component and therefore measures all cations in every charge state reaching it. Hence the FCs used for calculating the accelerator transmission are MFC 02-1 and FC 04-1 right after the analyzing magnet BM 03-1. The accelerator transmission ($T_{accelerator}$) is calculated as

$$T_{accelerator} = \frac{I_{FC\ 04\text{-}1}}{Q \cdot I_{MFC\ 02\text{-}1}} \tag{3.3}$$

where I is the current measured in the corresponding FC and Q is the charge state of the ions on the high energy side.

During the stripping process in the accelerator, the positive charge state distribution determines the possible transmission yield. The two most important parameters for changes of the charge state distribution are the accelerator terminal

voltage, thus the ions velocity during the stripping process, and the choice of stripper medium (foils or gases). In general, higher energy during the stripping process as well as using stripper foils, instead of gas, result in an increased yield for higher charge states. The charge state, in which the isotopes can be measured with decent transmission yield, therefore strongly depends on the capabilities of the AMS facility. The goal is to get as many ions as possible into one charge state, because all other ions are lost. Facilities with big accelerators typically use foils and measure in high charge states, e.g. from +7 to +11. At VERA the 3-MV tandem accelerator typically uses gas for the stripping process and the used charge states are in the range from +2 to +4. Furthermore, the most suited type of stripper gas (e.g. He, O_2, Ar) and its pressure inside the accelerator is chosen individually for different isotopes.

During the first beam time in September 2018 the effective yields of the charge states $^{88}Sr^{2+,3+,4+}$ were measured at different terminal voltages using Ar as stripper gas. The results are shown in Fig. 3.9.

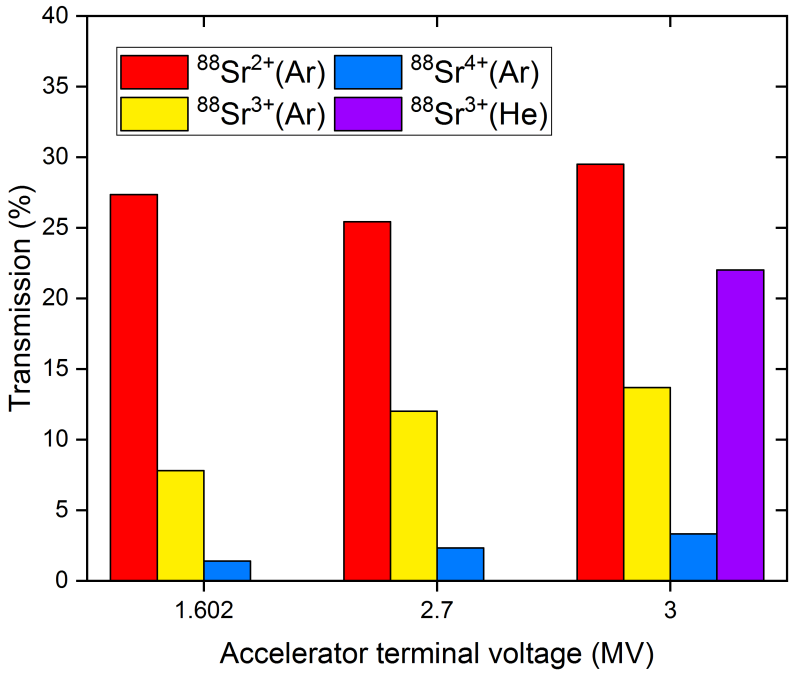

Figure 3.9.: Accelerator transmission for the three charge states $^{88}Sr^{2+,3+,4+}$ with Ar as stripper gas at different terminal voltages. At 3 MV one He data point was added for the Ar vs He stripper gas comparison.

It is evident the yields for higher charge states increase with beam energy. Despite a favorable accelerator transmission around 30 % for the +2 charge state, the +3 charge state was chosen for the ^{90}Sr measurements. The higher charge state adds an extra 3 MV of energy to the Sr ions. Higher ion energies achieve better isobar separation in the GIC-detectors energy loss spectra as discussed in section 3.1.4. The maximum observed yield for the +3 charge state was around 13 % at 3 MV terminal voltage. This was done at the optimal gas pressure of 2×10^{-8} T, which was tested separately (Fig. 3.10). Besides Ar also He was tested as stripper gas and it turns out to be better suited for measuring Sr^{3+}, as it reaches transmissions around 23 %. Fig. 3.10 shows the $^{88}Sr^{3+}$ accelerator transmission as a function of the stripper gas pressure for both He and Ar. The optimum for He is pretty low with 5×10^{-8} T and even lower for Ar.

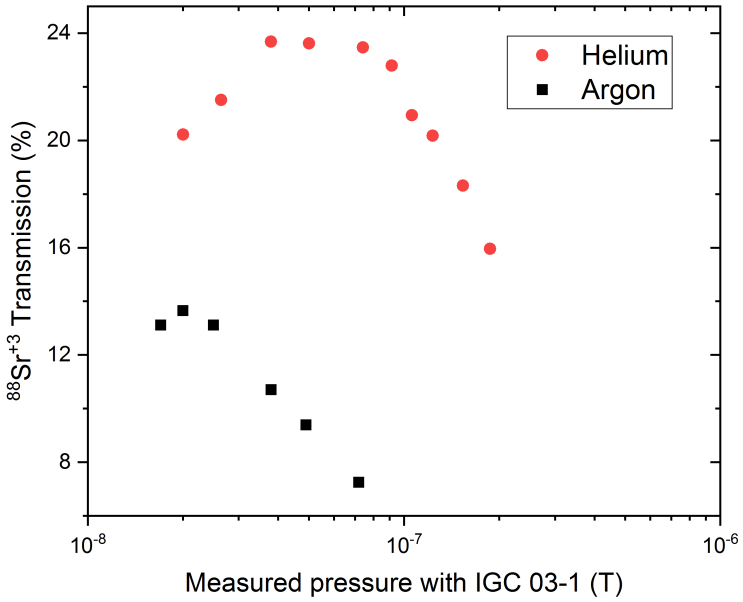

Figure 3.10.: Comparison of the optimal stripper gas pressure readings (IGC 03-1) for $^{88}Sr^{3+}$ with different gases. The used stripper gases are Ar (black) and He (red). Data points are taken from the beam times Sr1809 and Sr1907.

3.2.3. Detection efficiency

The overall ^{90}Sr detection efficiency describes the ratio of the detected ^{90}Sr and the total amount of ^{90}Sr atoms in the sample. The ^{90}Sr events in the detector together with the knowledge of all ^{90}Sr losses throughout the beam line provide everything needed to calculate the overall ^{90}Sr detection efficiency.
From section 3.1.3 we know that about 1 % of the ^{90}Sr in the sample produces $^{90}SrF_3^-$ and from section 3.2.1 that the ion cooler transmission for $^{90}SrF_3^-$ is around 35 %, while the accelerator transmission for $^{90}Sr^{3+}$ at a terminal voltage of 3 MV is around 23 %. As discussed in section 3.1.4, at least 50 % of the $^{90}Sr^{3+}$ events lie within the set region of interest (ROI). Taking all the above into account yields an overall ^{90}Sr detection efficiency of 0.4 ‰, i.e. every 2500$^{\text{th}}$ ^{90}Sr atom is detected.

3.2.4. Tuning procedure to set up a measurement

The ultimate goal of the tuning process is to get two setups: one for the trace isotope ^{90}Sr and one for the stable isotope ^{88}Sr as a reference. These setups are required because fast sequencing between two isotopes is not possible using the ILIAMS setup, since the magnet chamber of the BM I1-1 is not yet insulated. The differences between these setups are the mass injected into the ion cooler, the voltages of the multi beam switcher (MBS), the terminal voltage of the accelerator and the voltage of the high energy ESA.
In case a setup of the stable isotope from previous measurements is available it is loaded for the whole VERA beam line and used as a starting point of the tuning process, whereas the rest of the tuning process stays basically the same with or without an existing setup. The ion beam is stepwise guided through the whole beam line from one Faraday cup to the next one, while the parameters of the ion optical and deflecting components are optimized. The absence of a FC close to the ion cooler exit and two more 90° bends until FC 02-1 usually makes the tuning process through the ion cooler and into FC 02-1 the most time consuming and challenging part. The stepwise optimization process is typically done with a so-called „automax“ script, which searches for a local maximum of ion intensity in the FC or detector for all selected components of the beam line. More details can be found in the work of Steier 2000.

The ion beam of the stable isotope is too intense for the GIC-detector, therefore the $^{88}Sr^{3+}$ current is measured in FC 04-1 after the high energy analyzing magnet during measurements. Thus the stable setup only needs to be optimized up to FC 04-1, but usually includes tuning until FC L4-1 just in front of the GIC-detector. Once the setup is optimized it is saved. To get the trace isotope setup, the existing ^{88}Sr setup is used and only the few components listed above are rescaled to the corresponding masses and charge states. At VERA the rescaling can be done automatically except for BM I1-1, which can be calculated using equation (3.4), where B is the magnetic field strength and $m_{88,90}$ are the masses of the molecules $^{88}SrF_3^-$ and $^{90}SrF_3^-$ respectively.

$$B(^{90}SrF_3^-) = B(^{88}SrF_3^-) \cdot \sqrt{\frac{m_{90}}{m_{88}}} \tag{3.4}$$

After rescaling, the components are checked on the count rate of an isobar spiked sample in the detector and the setup is also saved. Due to the hysteresis effect of the magnet BM I1-1 it can be helpful to check whether the magnetic field reaches the optimal value of each setup if switched between them. In the case of Sr, the magnetic field after changing between the setups is typically 2 - 3 G off. Through iterative optimization of the magnet current it is possible to find values, where the magnetic field fits almost perfectly. These optimized current values for the BM I1-1 are then saved in the setups.

3.2.5. Measurement routine

The strontium measurement routine is different than routine measurements at VERA that do not need the ILIAMS setup. The Multi Beam Switcher (MBS) 01-1 allows fast switching between the stable and trace isotope, without changing the injection magnets magnetic field strength. This is not possible with the ILIAMS setup, due to the fact that there is no MBS for BM I1-1 yet, and the magnetic field strength has to be changed accordingly with the used setups. The switching times between setups requires a few seconds.

At VERA both ion sources use sample wheels holding up to 40 samples. In AMS blank materials and reference materials, also called standards, are measured in

addition to unknown samples. The blank material supposedly contains no trace isotopes and therefore is measured to get the background level, while the reference materials have known isotopic ratios and are used for normalization. The system collects data of the stable and the trace isotope for all measured cathodes in so-called „runs“. Every run is numbered in increasing order. Over the course of a measurement each cathode is measured multiple times to achieve higher precision. To distinguish those multiple measurements they are combined in „turns“, thus a measurement consists of multiple turns containing single runs of each cathode. Each run is also split in more parts called „sequences“. A sequence consists of two separate measurements one with the stable setup and one with the trace isotope setup, which will be referred to as „current sequence“ and „event sequence“ respectively.

Current sequence

During this sequence, the current of the stable ^{88}Sr is measured in different Faraday cups (FC). First, the $^{88}SrF_3^-$ current in front of the ion cooler is measured for 5 seconds in FC I1-1. Afterwards all FCs up to FC 04-1 are opened and the $^{88}SrF_3^-$ and $^{88}Sr^{3+}$ currents are measured for 5 seconds, almost simultaneously by fast switching. $^{88}SrF_3^-$ is measured in the offset cup MFC 02-1 in front of the accelerator and $^{88}Sr^{3+}$ in the FC 04-1 after the analyzing magnet on the high energy side. This combination allows monitoring the ion cooler and accelerator transmissions throughout a run.

Event sequence

The event sequences are much longer than the current sequences and are typically 150 s long. All events are recorded with the GIC-detector and the $^{90}Sr^{3+}$ region of interest (ROI) is set during offline-analysis of the two-dimensional energy loss spectra of the detector. From the mean $^{88}Sr^{3+}$ current, before and after the event sequence, and the number of $^{90}Sr^{3+}$ events in the set ROI the isotopic ratio ^{90}Sr/^{88}Sr is calculated.

These sequences are repeated three times, hence one single run consists of three event sequences and four current sequences. The specifics of the sequences, e.g. measured cathodes and their duration, can be arranged in a corresponding script file, called „control.log“.

3.3. AMS Results for ^{90}Sr

In this section the results of the AMS measurements for two dilution series are summarized and discussed. The preparations and the first ^{90}Sr measurement were quite successful, hence we were able to do several more measurements and improve the previous detection limit for ^{90}Sr by more than an order of magnitude. All AMS measurements have been conducted with in-house made SrF_2 standard material, blank material (SrF_2, Alfa Aesar) and Zr-spiked material. Two dilution series produced at least three dilution steps of standard materials each with ^{90}Sr/^{88}Sr ratios differing by roughly an order of magnitude. All materials have been measured at least once. The evaluation of the measurement's raw data will be given in Appendix A.

3.3.1. IAEA-TEL-2016-03 reference solution

The IAEA-TEL-2016-03 reference solution was used for the first dilution series and has a nominal activity of $(20.5 \pm 0.5)\,\mathrm{Bq\,kg^{-1}}$ of ^{90}Sr as of 2018, it will be referred to as „TEL“. Four different dilution samples and one corresponding blank of SrF_2 were produced with this material. Their properties can be found in Tab. 3.5. Afterwards their content of stable Sr was measured with inductively coupled plasma mass spectrometry (ICP-MS) to calculate the nominal ^{90}Sr/Sr isotopic ratios together with their uncertainties.

name	**material**	**Type**	**calculated ^{90}Sr/Sr ratio**
TEL-11	SrF_2	reference	$(1.09 \pm 0.03)\times10^{-11}$
TEL-12	SrF_2	reference	$(1.50 \pm 0.04)\times10^{-12}$
TEL-13	SrF_2	reference	$(1.74 \pm 0.05)\times10^{-13}$
TEL-14	SrF_2	reference	$(1.23 \pm 0.04)\times10^{-14}$
TEL-Blank	SrF_2	blank	0

Table 3.5.: Calculated nominal ^{90}Sr/Sr isotopic ratios of the SrF_2 reference and blank materials produced with the IAEA-TEL reference solution.

The ^{90}Sr/Sr ratios of these materials were measured twice in two different beam times (Sr1811 and Sr1901) and the TEL-11 was used for normalization. Not all

reference materials had the same amount of cathodes measured, because different amounts of material were produced. Measured results from all dilution steps are in good agreement with the nominal values within their $1\,\sigma$ uncertainty. The overall result of the measurements can be seen in Fig. 3.13, where the measured values are compared with the nominal values.

In Fig. 3.11 two energy loss spectra in the GIC-detector are shown, one is from a blank material and the other one is from the TEL-11 reference material. It shows different ion species reaching the detector. Knowing the location of the $^{90}Zr^{3+}$ events, the region of interest (ROI) for $^{90}Sr^{3+}$ can be set. Although almost complete ^{90}Zr suppression is achieved by the ILIAMS setup for typical samples without Zr-admixture and most of the events outside of the ROI are probably real $^{90}Sr^{3+}$ events, only the events in the ROI are counted. How tight the ROI has to be set depends on the desired isobar separation in the detector, discussed in section 3.1.4.

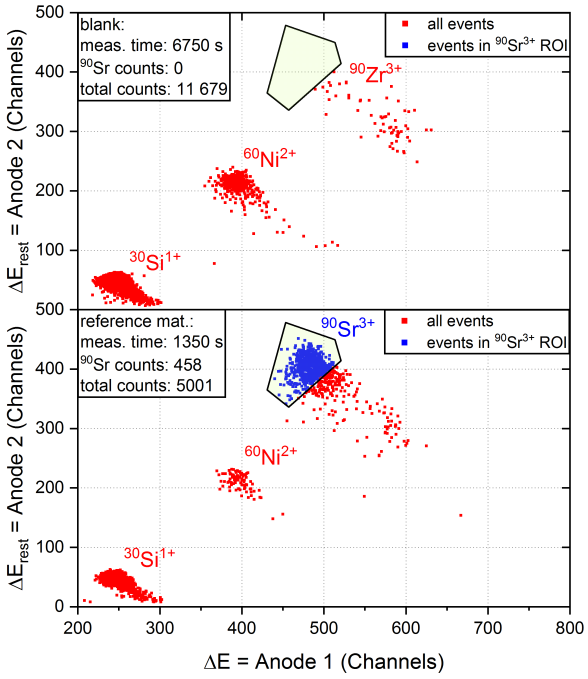

Figure 3.11.: Comparison between the two-dimensional energy loss spectra of a blank (top) and the TEL-11 with a nominal ratio of $^{90}Sr/Sr = (1.09 \pm 0.03) \times 10^{-11}$ (bottom) in the GIC-detector. The detected $^{90}Sr^{3+}$ events inside the ROI are in blue, while the remaining events are in red. One channel corresponds to roughly 12.5 keV. The spectra were taken from the beam time Sr1901.

The uncertainty for the measured material is the maxiumum of either the model uncertainty due to counting statistic or the scatter of the measured data. For the high standards TEL-11 and TEL-12 the relative uncertainty of the mean is 3.75 % and 8.07 %, respectively. For the low standards TEL-13 and TEL-14 it is 24 % and 50.2 %, respectively. The measurement results for the cathodes themselves can be seen in Fig. 3.12. Averaging over several cathodes of the same material was done by weighting individual results with the weights $w_i = \frac{1}{(\text{rel. uncert.})^2}$. This was done because of the low counting statistics of the TEL-14 cathodes, such that

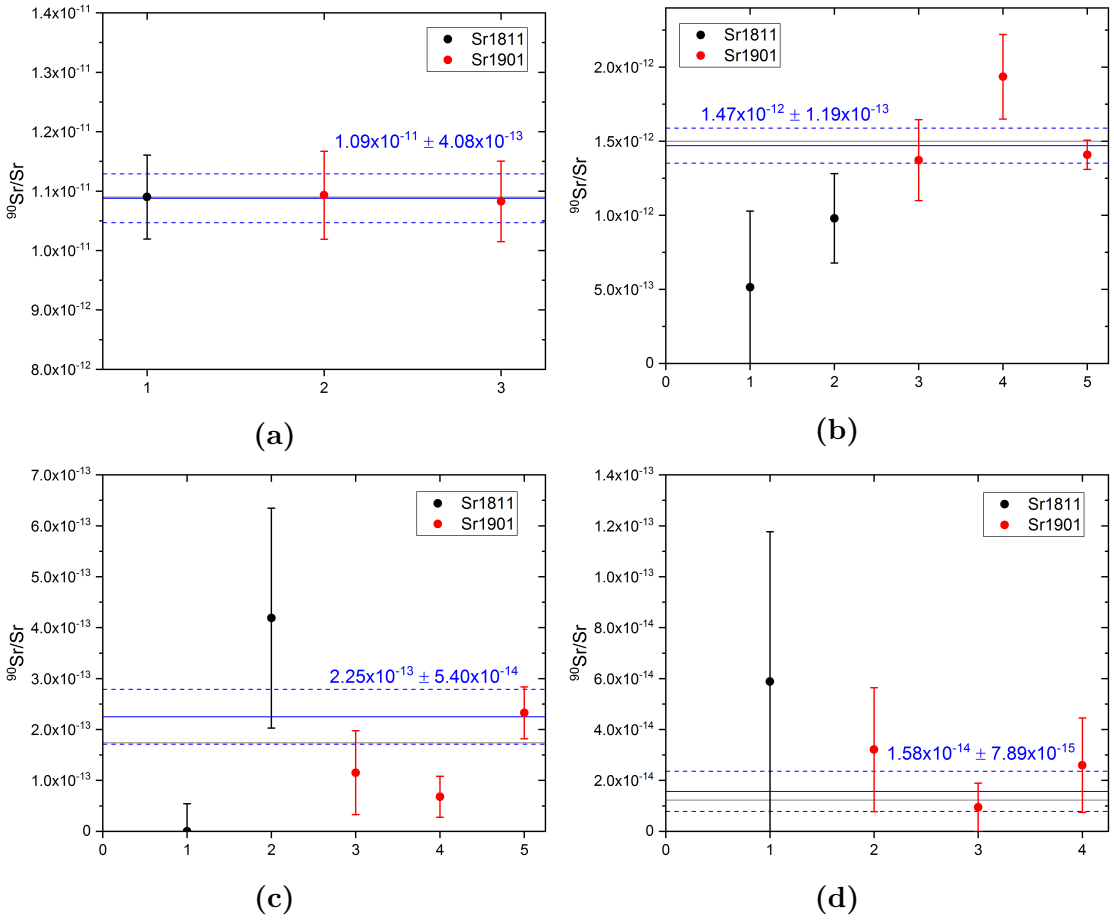

Figure 3.12.: Results of the ^{90}Sr measurements with the TEL reference materials for cathodes containing the dilution series materials (a) TEL-11, (b) TEL-12, (c) TEL-13 and (d) TEL-14 during the beam times Sr1811 (black) and Sr1901 (red). The solid lines represent the nominal ratio (gray) and the weighted average (blue), the dotted lines represent the uncertainty of the mean value. Every data point with its uncertainty represents a measured cathode in the corresponding beam times.

cathodes with smaller relative uncertainties have more weight than cathodes with just 1 event or less.

The uncertainties of the individually measured cathodes of the TEL-13 and TEL-14 is dominated by the low counting statistics, whereas their uncertainty is dominated by the scatter for the overall result of the material (see Fig. 3.12 or Fig. 3.13). For the TEL-12 it is different, the number of events is usually high enough that the uncertainty is dominated by the scatter for both, the individual cathodes and for the overall result. Since the TEL-11 is used for normalization there is no inter beam time scatter.

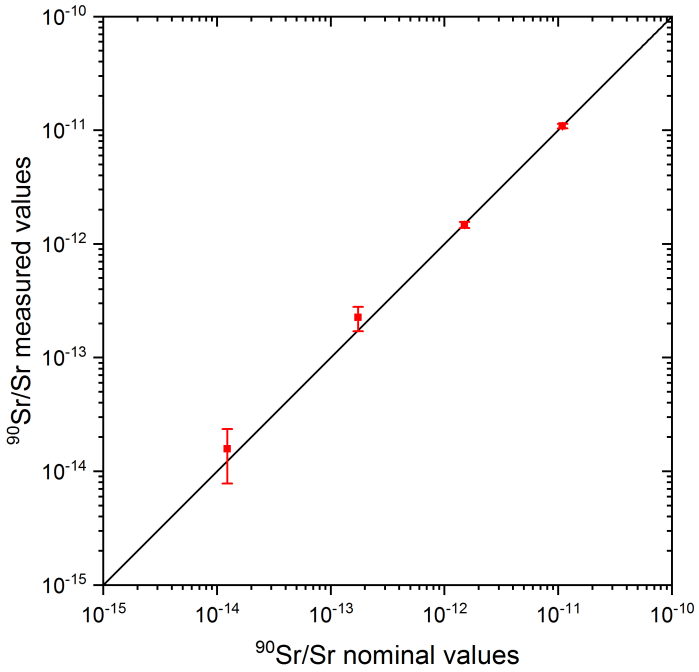

Figure 3.13.: Comparison of the measured and nominal ^{90}Sr/Sr ratios for the TEL dilution series. The data points represents the overall measurement results from both beam times. The solid line represents a 1:1 agreement of measured and nominal values. Note that measured results were normalized on the TEL-11 nominal value and thus only the linearity of measurement results is demonstrated.

3.3.2. Liquid scintillation counting calibration solution

The second solution was a former calibration solution of ^{90}Sr for liquid scintillation counting (LSC), it will be referred to as „LSC“. The LSC dilution series was made, because a large quantity of in-house reference material was needed and no TEL material was left. This time three different dilutions of SrF_2 were produced. Their estimated properties are listed in Tab. 3.6. The precise ratios are still unknown, because ICP-MS measurements of stable strontium of the LSC materials are still to be done. For each material around 800 mg were produced such that enough reference material is available for the next few years.

name	**Type**	**estimated ^{90}Sr/Sr ratio**	**amount (mg)**
Sr11	SrF_2	5.40×10^{-11}	≈ 800
Sr12	SrF_2	4.93×10^{-12}	≈ 800
Sr13	SrF_2	5.40×10^{-13}	≈ 800

Table 3.6.: Estimated ^{90}Sr/Sr isotopic ratios of the SrF_2 reference materials produced with the LSC solution.

The materials were tested once in the last beam time at the end of July (Sr1907). The preliminary results can be seen in Fig. 3.15. It shows a comparison between the measured and estimated isotopic ratios. When normalized to the estimated Sr11 ratio the other two reference materials are in good agreement within $1\,\sigma$ uncertainty. The uncertainty of the mean for Sr11 and Sr12 is 6.87 %, due to high scatter of the data (see Fig. 3.14), and 6.57 % respectively. For Sr13 it is 37.80 %, because only one cathode was measured there is no plot in Fig.3.14. The LSC reference materials have no dilution step with a ^{90}Sr/Sr ratio on the order of 10^{-14}, therefore no weighted average was needed nor used for the evaluation. The measurement results can be seen in Fig. 3.14.

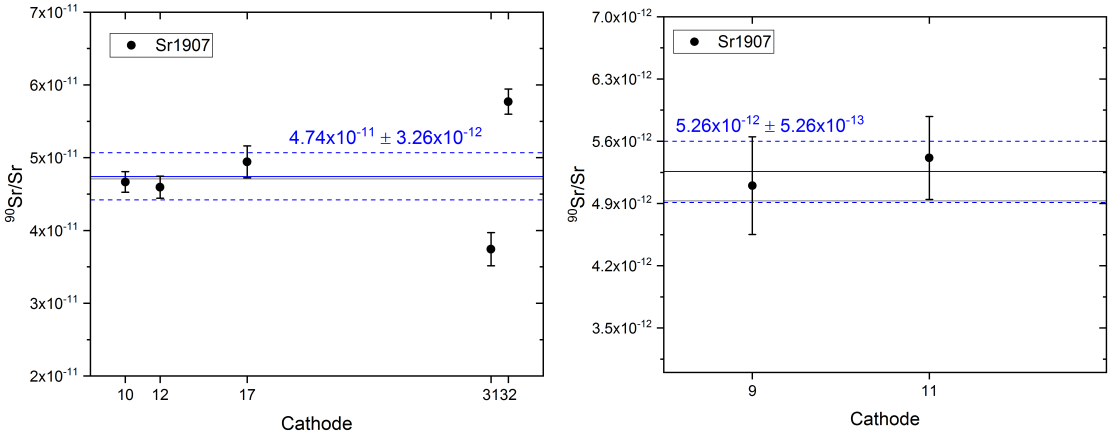

(a) **(b)**

Figure 3.14.: Results of the ^{90}Sr measurement of the cathodes containing the reference materials (a) Sr11 and (b) Sr12 during the beam time Sr1907. The solid lines represent the nominal value (gray) and the average (blue), the dotted lines represent the average's uncertainty. Measured results were normalized on the Sr-11 nominal value and thus only the linearity of measurement results is demonstrated.

3.3.3. Reproducibility

In this beam time a lot of Sr11 material has been measured to test the reproducibility of the results. This was done by placing three cathodes of the same material near to each other and two cathodes were placed on the opposite side of the sample wheel. The results of the measured cathodes and their position in the sample wheel can be seen in Tab. 3.7.

wheel position	**measured ^{90}Sr/^{88}Sr**
Cat 10	$(5.65 \pm 0.18) \cdot 10^{-11}$
Cat 12	$(5.57 \pm 0.19) \cdot 10^{-11}$
Cat 17	$(5.99 \pm 0.27) \cdot 10^{-11}$
Cat 31	$(4.53 \pm 0.28) \cdot 10^{-11}$
Cat 32	$(6.99 \pm 0.22) \cdot 10^{-11}$

Table 3.7.: Results of the measured cathodes, containing reference material on the order of ^{90}Sr/^{88}Sr$=10^{-11}$, placed on different wheel positions to test the reproducibility of the measurement.

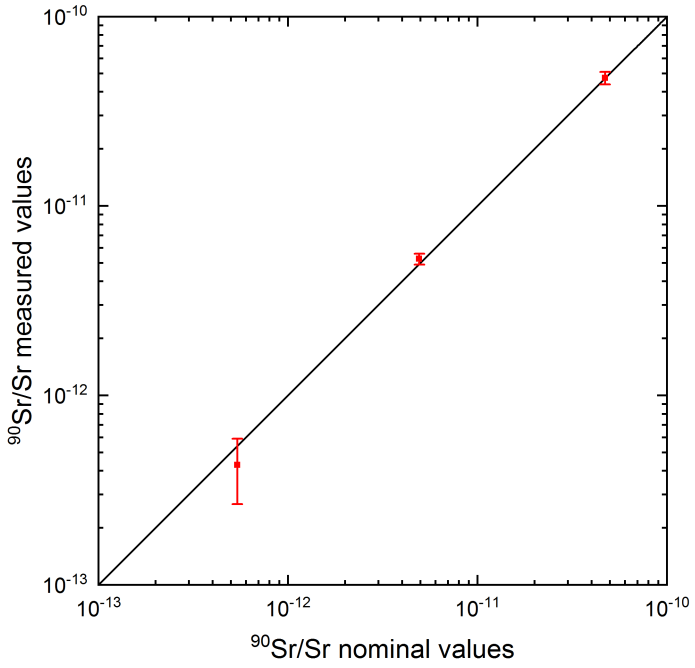

Figure 3.15.: Comparison of the measured and estimated ^{90}Sr/Sr ratios for the LSC dilution series. The solid line represents a 1:1 agreement of measured and estimated values. Note that measured results were normalized on the Sr11 nominal value and thus only the linearity of measurement results is demonstrated.

The results of the three cathodes Cat 10, Cat 12 and Cat 17 agree with each other within their 1σ uncertainties. The results of the remaining two cathodes however do not agree within their 1σ uncertainties and also not with the results of Cat 10, Cat 12 or Cat 17. To calculate the reproducibility eq. (3.5) was used.

$$\mathrm{R} = \frac{\sigma_{\mathrm{exp}}}{\overline{\mathrm{x}}} \tag{3.5}$$

Here R is the reproducibility, σ_{exp} is the standard deviation of the results containing identical material and $\overline{\mathrm{x}}$ is the average. Calculating the reproducibility only from Cat 10, Cat 12 and Cat 17 yields reproducibility of 3.87 %. However, if all measured cathodes of the Sr11 material are used then the reproducibility is almost 4 times higher with 15.38 %. The exact reason for the huge scatter of the two cathodes is unknown, but during this beam time the measurement conditions were difficult. A broken electrical connection led to erratic charge-up of the ion

cooler aperture and thus unstable conditions. Hence, the tuning was most likely not optimal and more sensitive to an offset or tilt of the wheel axis in the ion source or other slight differences in the sputter geometry among samples. Therefore the measurement will be repeated in the next beam time.
When looking at the results of the individual turns a similar picture can be seen (Fig. 3.16). The cathodes 10, 12 and 17 do scatter, but usually agree with each other within their uncertainties. The cathodes 31 and 32 however show big discrepancies in their measured ratios. They are the closest to each other right after a fresh tuning, but rapidly drift away from each other in the following turns.

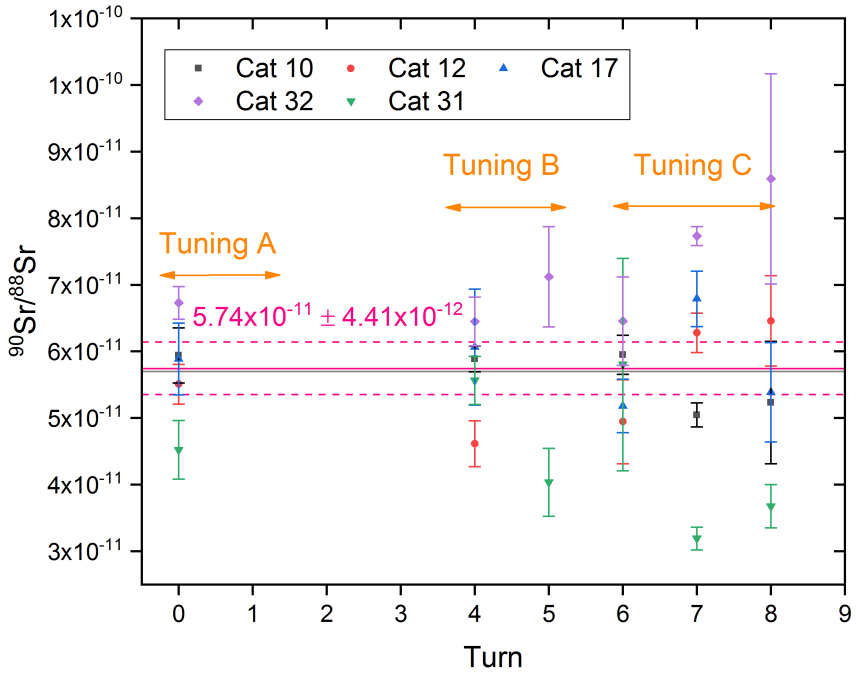

Figure 3.16.: Results of the ^{90}Sr measurement of each individual turn for the cathodes containing the Sr11 reference material during the beam time Sr1907. The solid lines represent the nominal ratio (gray) and the average (pink), the dotted lines represent the uncertainty of the average.

3.3.4. Blank level

Taking all measurements into account and calculating the ^{90}Sr/Sr-ratios of all blanks (Alfa Aesar material and the TEL-Blank) leads to an overall blank level of $^{90}\mathrm{Sr/Sr} = (4.5 \pm 3.2) \times 10^{-15}$. The limit of detection (LoD) can be calculated with the formula:

$$\mathrm{LoD} = \overline{\mathrm{x}}_{\mathrm{blank}} + 3\sigma_{\mathrm{blank}} \tag{3.6}$$

Here σ_{blank} is the uncertainty and $\overline{\mathrm{x}}_{\mathrm{blank}}$ is the average of the blank level. Hence, the blank level corresponds to a LoD of < 0.1 mBq (< 0.02 fg). This is equivalent to around 10^5 atoms of ^{90}Sr in 1 mg of Sr. With the overall detection efficiency of 0.4 ‰, 40 events of $^{90}Sr^{3+}$ out of these 10^5 would be be detected. The main problem of getting a lower blank limit might be cross contamination in the ion source, because the position of ^{90}Sr events of blank materials in the energy loss spectra typically are right in the set region of interest for Sr. There are also no events located at the $^{90}Zr^{3+}$ position in these spectra (see Fig. 3.17). Thus it is assumed, that those events come from cross contamination of the high reference material in the ion source, during target preparation or from the intrinsic ^{90}Sr conten of commercial SrF_2. These results show that the previous LoD with AMS of 3 mBq (Tumey et al. 2009) has been improved by a factor of 30, despite much lower ion energies were used. Thus AMS, compared to other methods, now provides the best sensitivity for ^{90}Sr using ILIAMS at VERA (see section 2.2.3).

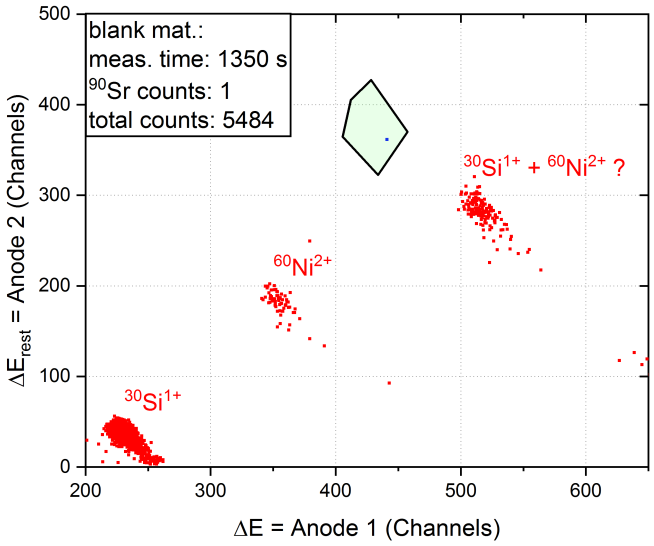

Figure 3.17.: Exemplary two-dimensional energy loss spectrum of a blank material to showcase the typical location of events in the ^{90}Sr ROI for blank materials. The detected $^{90}Sr^{3+}$ events are in blue, while the remaining events are in red. One channel corresponds to roughly 13.5 keV. Note the absence of ^{90}Zr events in the spectrum. ^{90}Zr is fully suppressed with ILIAMS and thus unlikely that blank events stem from isobaric interferences.

4. Measurements and results for ^{99}Tc

This chapter gives an overview of the results for ^{99}Tc. No AMS measurements have been conducted yet, therefore it mainly focuses on the search for suitable molecular systems using the ILIAMS setup.

4.1. Search for suitable molecular systems

Technetium is special with respect to the other two investigated nuclides, because there exists no stable Tc isotope. However the electron affinity (EA) of elemental Tc, similar to Sr, is known to be smaller than the EAs of its potential isobars. Hence a molecular anion suitable for operation with the ILIAMS setup has to be found. The absence of a stable isotope for Tc makes the search for a suitable molecular system difficult, due to the fact that the EA of the Tc molecules can not be checked easily. As a starting point for further research, the EAs of the potential isobars have been investigated for fluoride and oxide molecules with two different lasers with wavelengths of 532 nm and 355 nm respectively.

4.1.1. Isobaric background

There are two potential isobars that might interfere during AMS measurements of ^{99}Tc. The isobar for mass 99 is the stable isotope ^{99}Ru which has a natural abundance of 12.76 %. The established method of ^{99}Tc AMS uses ^{93}Nb for normalization where no other stable isobar requires suppression. In order to avoid uncertainties in negative ion yield and behavior in the ILIAMS system, it is considered to use ^{97}Tc in the future. This would introduce a second interfering isobar

for the measurement, which is the stable isotope ^{97}Mo with a natural abundance of 9.56 %. In Fig. 4.1 the relevant section of the nuclide chart for Tc is shown. The elemental EAs (i.e. Tc, Ru and Mo) and all known molecular fluoride and oxide EAs for these nuclides are listed in Tab. 4.1. In contrast to Sr, it is not clear for Tc which fluoride or oxide molecules have suitable EAs and there is no information on molecular EAs for Tc at all. Thus every molecule that forms inside the ion source has to be investigated.

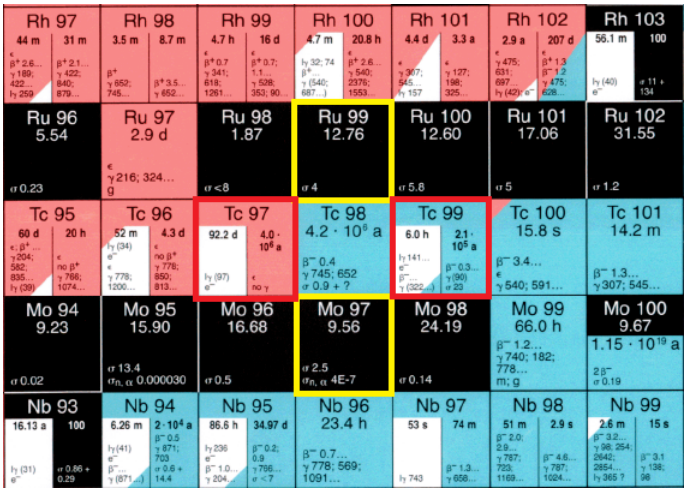

Figure 4.1.: Nuclide chart around mass 99 amu. The nuclides of interest are marked in red and the interfering isobars are marked in yellow. Picture was taken from *Karlsruher Nuklidkarte, 7th edition.*

4.1.2. Molecule formation within the ion source

Investigations on the yield for each molecule inside the ion source were carried out by mass scans. Starting from ion source S2 the magnetic field of BM I1-1 was varied by changing the current from 92 A to 150 A and the ion beam current was measured in Faraday cup FC I1-1 right after the magnet (see Fig. 3.7). The resulting mass range goes from 87 to 220 amu, which is enough to see the heaviest formed molecule $^{100}MoF_6^-$ at 214 amu.
Tab. 4.2 lists the matrices and mixing ratios of the sputter targets used in this study. Evaluation and mass calibration of the scans was done the same way as for Sr (cf. section 3.1.2). The results of the mass scans from the two beam times Tc1810 and Tc1903 can be found in Fig. 4.2.

anion	EA (eV)	reference
Tc^-	0.55 ± 0.20	Andersen et al. 1999
Ru^-	1.04638 ± 0.00025	Norquist et al. 1999
Mo^-	0.748 ± 0.002	Gunion et al. 1996
MoF_3^-	< 3.3	Sidorov et al. 1982
RuF_4^-	4.75 ± 0.28	Kuznetsov et al. 1989
MoF_4^-	< 3.0	Sidorov et al. 1982
MoF_5^-	3.46 ± 0.18	Borshchevskii et al. 1988
MoF_6^-	3.82 ± 0.19	Borshchevskii et al. 1988
MoO^-	1.290 ± 0.006	Gunion et al. 1996
MoO_3^-	3.17 ± 0.02	Yoder et al. 2005

Table 4.1.: List of the Tc, Ru & Mo electron affinities. All fluoride and oxide molecules, for which the EAs are published are listed.

As for Sr it was not possible to reproduce the distribution of fluoride molecules by Zhao et al. 2010 within our ion source. The sample matrices of Ru and Nb mixed with PbF_2, show different fluoride formation patterns than the literature (see Fig. 4.2 (a), (c) and (e)), whereas the MoF_x^- pattern is in agreement with the literature, i.e. MoF_5^- has the highest yield followed by MoF_4^-. An interesting behavior can be seen for the molecule formation of RuF_x^-. The data shows that the formation of higher fluoride molecules is heavily suppressed if the matrix is additionally mixed with Nb, while the total current decreases by a factor of 4. This is consistent with a recently published paper (Cornett et al. 2019), where the

sample matrix	mass-ratio
Ru + PbF_2	1:2
Ru + PbF_2	1:5
Mo + PbF_2	1:2
Nb + PbF_2	2:5
Ru + Nb + PbF_2	1:2:5
RuO_2	–
MoO_2	–
Nb_2O_5	–
RuO_2 + Nb_2O_5	1:2

Table 4.2.: Matrices and mixing ratios of sputter targets used during mass scans to investigate the molecule formation within the ion source.

formation yield of RuF_x^- is suppressed by adding either Fe or Nb to the matrix. The addition of more PbF_2 to the matrix (1:2 vs 1:5) does not significantly change the molecule formation.
For Nb the effect is reversed. When only mixed with PbF_2, the largest yield is by far NbF^- with more than 50 %. If Ru is added to the matrix, the higher fluoride molecules (i.e. NbF_5^- & NbF_6^-) reach more than double the yield, while the other molecules, with the exception of NbF^-, stay almost the same. No significant change in the total current of NbF_x^- was found due to the addition of Ru in the matrix.
The oxide results indicate a similar effect when Nb and Ru are in the same matrix. Ru does not form RuO_2^- and RuO_3^- anymore if Nb is part of the matrix, while the yield of the elemental anion Ru^- is almost 12 times higher. The effect for NbO_x^- also shifts towards higher oxide molecules, but not nearly as intense as observed for the fluoride molecules. The total currents for the oxides also behave similar to the fluorides, while the total current of RuO_x^- decreased by a factor of 8 it did not significantly change for NbO_x^-.

4.1.3. Isobar suppression

The electron affinities (EA) of all formed isobaric fluoride and oxide molecules of Ru and Mo were tested, even though some of the EAs are known and listed in Tab. 4.1. This was done by overlapping the anion beam with the 532-nm laser inside the RFQ ion guide and measuring the current after the ion cooler in either Faraday cup FC I2-2 or FC 02-1 with and without laser. The results of these tests are shown in Fig. 4.3. Until now, the only molecules tested with the new 355-nm laser are RuO_2^- and RuO_3^- (Fig. 4.3 (a)).
All tests with the 532-nm laser were done in the beam time Tc1810 and the current was measured in FC I2-2, which is not optimal due to the lack of m/q filtering option between ion cooler and Faraday cup. However this was the only option since another AMS beam time was conducted in parallel from the ion source S1. If the photon energy is high enough to detach the extra electron of the injected molecules, no or almost no current is detected in the Faraday cup. Negligible change in the detected current is a clear indicator that the EA of the injected

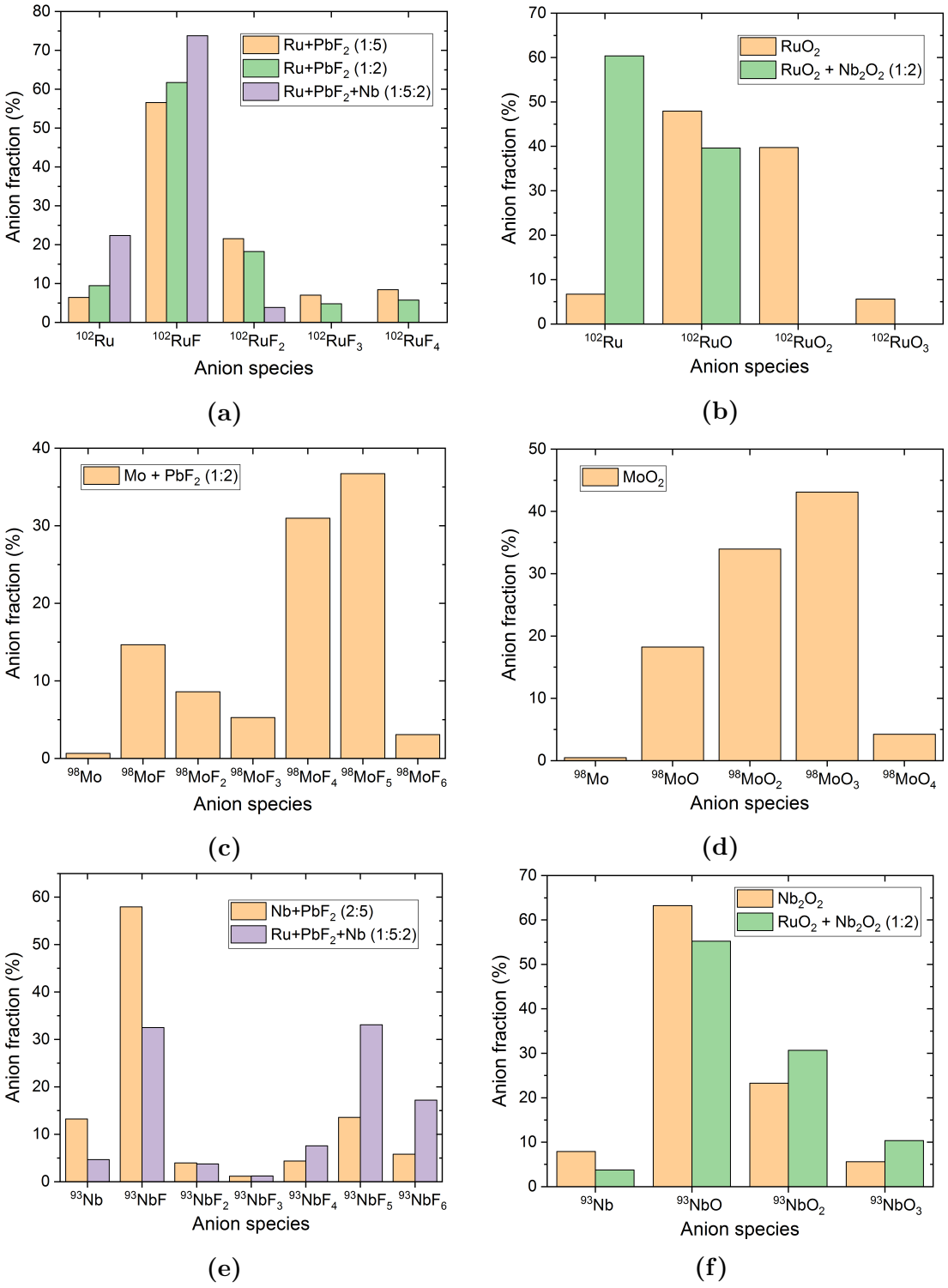

Figure 4.2.: Results of the mass scans for (a) RuF_x^-, (b) RuO_x^-, (c) MoF_x^-, (d) MoO_x^-, (e) NbF_x^- and (f) NbO_x^-. Empty columns correspond to no formation or formation below the Faraday cup threshold of 100 pA. The diagrams are normalized to the total current output of all detected molecules represented in the diagrams.

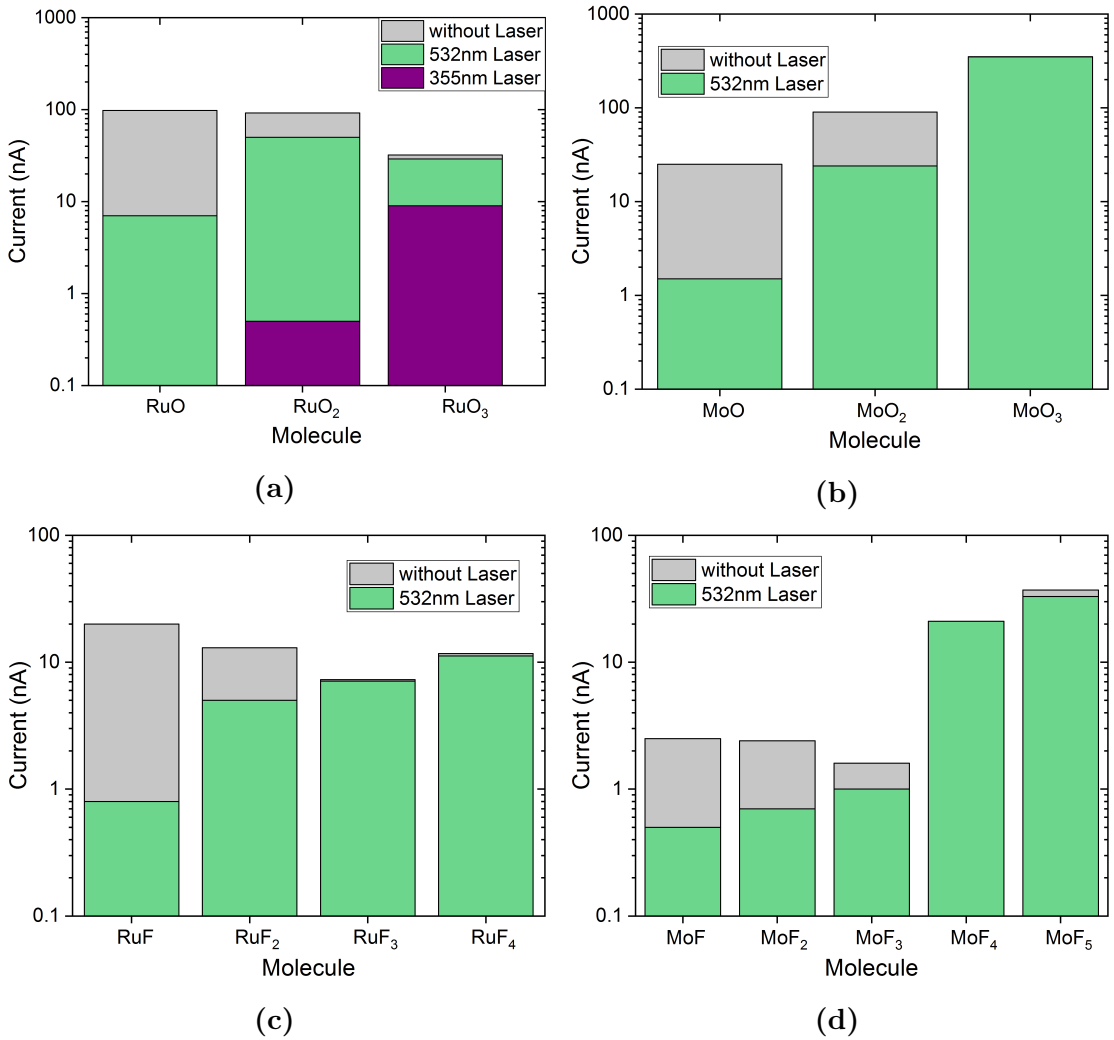

Figure 4.3.: Results of the laser photodetachment tests for (a) RuO_x^-, (b) MoO_x^-, (c) RuF_x^- and (d) MoF_x^-. It shows the measured current without laser (gray), with the 532 nm laser (green) operated at 10 W and with the 355 nm laser (purple) operated at 2.2 W. Note the logarithmic scale for the ion current. The data for the 532 nm laser was from the beam time Tc1810 measured in FC I2-2 and the data for the 355 nm laser was from Tc1906 measured in FC 02-1.

molecule is above the photon energy. On the other hand, if the detected current drops slightly it makes the interpretation tricky since it is not possible to unambiguously identify the anions generating the current in the Faraday cup due to the missing m/q filtering component. Another possibility is that their EA is slightly higher or lower than the used photon energy such that only a fraction

of the injected molecules are affected. With this in mind, the molecules where the interpretation is not straightforward are RuO^-, MoO^-, RuF^-, MoF^-, RuO_2^-, RuF_2^- and MoO_2^-. For these molecules only an estimate of their EA limit can be given.

The tests on RuO_2^- and RuO_3^- with the 355 nm laser were done in the beam time Tc1906, but this time the current was measured in the FC 02-1. Fig. 4.3 shows the results operating the laser at 2.2 W and a repetition rate of 100 kHz. With 10 W and a repetition rate of 100 kHz, the 500 pA of RuO_2^- surviving at 2.2 W vanished completely while for RuO_3^- still 170 pA of the 9 nA survive.

With the results upper and/or lower limits of the EAs between 2.33 - 3.49 eV for each molecule can be given and these are listed in Tab. 4.3. Comparing the EAs of the measured results and the literature from Tab. 4.1 there are no discrepancies.

molecule	**EA limit (eV)**	**molecule**	**EA limit (eV)**
MoF^-	<2.33	RuF^-	<2.33
MoF_2^-	<2.33	RuF_2^-	$\lesssim 2.33$
MoF_3^-	$\lesssim 2.33$	RuF_3^-	>2.33
MoF_4^-	>2.33	RuF_4^-	>2.33
MoF_5^-	>2.33		
MoO^-	<2.33	RuO^-	$\lesssim 2.33$
MoO_2^-	$\lesssim 2.33$	RuO_2^-	$2.33 \lesssim EA(RuO_2^-) < 3.49$
MoO_3^-	>2.33	RuO_3^-	$2.33 < EA(RuO_3^-) \lesssim 3.49$

Table 4.3.: Experimental electron affinity limits for various fluoride and oxide molecules of ruthenium and molybdenum. Note that not all results are unambiguous and these limits only represent estimations.

4.1.4. Transmission

Already some data regarding the ion cooler and accelerator transmissions are available, but not yet in such detail as for Sr.

Ion cooler transmission

The transmission was calculated with equation (3.2) for the molecules NbF_5^-, NbO^- and RuO^-. The results are listed in Tab. 4.4 and were collected with 0.25 mbar of pure He as buffer gas.

molecule	injected current (nA)	transmission (%)
NbF_5^-	12	30
NbO^-	180	18
RuO^-	90	7

Table 4.4.: Ion cooler transmissions of NbF_5^-, NbO^- and RuO^- with 0.25 mbar of He as buffer gas.

Accelerator transmission

The accelerator transmission was calculated with equation (3.3) for Nb and Ru in the +3 charge state with O_2 as stripper gas, while the accelerator was operated at 3 MV. The transmission yield can be found in Tab. 4.5.

injected ion	extracted ion	transmission (%)
NbF_5^-	$^{93}Nb^{3+}$	10
NbO^-	$^{93}Nb^{3+}$	18
RuO^-	$^{99}Ru^{3+}$	10

Table 4.5.: Accelerator transmission of Nb^{3+} and Ru^{3+}. The Accelerator was operated at 3 MV and a O_2 stripper gas pressure of 4.0×10^{-8} T in IGC 03-1.

5. Measurements and results for ^{107}Pd

This chapter will give an overview of the results for ^{107}Pd. No AMS measurements have been conducted yet, therefore it mainly focuses on the search for suitable molecular systems using the ILIAMS setup.

5.1. Search for a suitable molecular systems

The same way as for the other two nuclides, the electron affinity (EA) of elemental Pd is smaller than the EA of its interfering isobar. Therefore a suitable molecular system for the ILIAMS setup has to be found. Not much information about the EAs of the fluoride molecules can be found for either Pd or its isobar Ag, but fluoride and oxide molecules were still both investigated to find out whether there exists a suitable one for VERA.

5.1.1. Isobaric background

^{107}Pd has only one potential isobar interfering in AMS measurements, which is stable ^{107}Ag with a natural abundance of 51.84 %. The corresponding part of the nuclide chart can be found in Fig. 5.1.
All known EAs, i.e. for elemental Pd and Ag as well as for their oxide and fluoride molecules, are listed in Tab. 5.1. It can be deduced that elemental Pd, PdO^- and PdO_2^- can not be used with the current laser setup due to their EAs being either too low for the 532 nm or the 355 nm laser. Hence at first glance the fluoride molecules are the more promising ones.

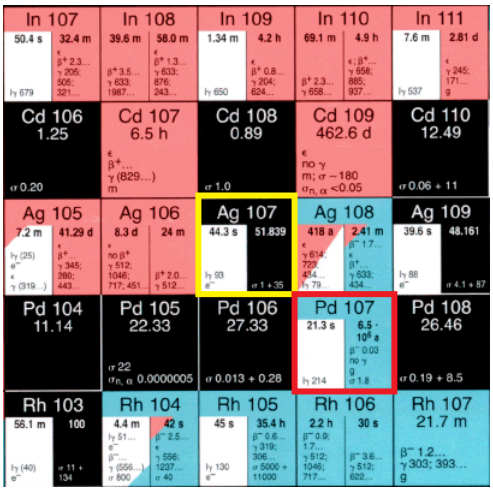

Figure 5.1.: Nuclide chart around mass 107 amu. The isotope of interest is marked in red and the interfering isobar is marked in yellow. Picture was taken from *Karlsruher Nuklidkarte, 7th edition.*

anion	EA (eV)	reference
Pd^-	0.56214 ± 0.00012	Scheer et al. 1998
Ag^-	1.30448 ± 0.00005	Bilodeau et al. 1998
PdO^-	1.672 ± 0.005	Ramond et al. 2002
AgO^-	1.654 ± 0.002	Andrews et al. 2002
PdO_2^-	3.086 ± 0.005	Ramond et al. 2002

Table 5.1.: List of the Pd and Ag electron affinities, as well as for all published fluoride and oxide molecules.

5.1.2. Molecule formation within the ion source

The mass scans and their evaluation were done the same way as for Sr and Tc (see sections 3.1.2 or 4.1.2). The bending magnet current was varied from 97 A to 155 A, which, after mass calibration, corresponds to a covered mass range of 97 to 233 amu. In Tab. 5.2 the sample matrices used in the mass scans are listed, the mass scan results are shown in Fig. 5.2.

In contrast to the other two nuclides no higher fluorides than di-fluoride molecules are formed at all in the ion source. PdF^- forms almost exclusively inside the ion source with around 70 %, while AgF^- and AgF_2^- are both formed with around 40 % relative yield. These PdF_x and AgF_x molecule formation patterns are in agreement with Zhao et al. 2010.

sample matrix	mass-ratio
Pd + PbF_2	1:2
Ag + PbF_2	1:1
PdO	–
AgO	–

Table 5.2.: Sample matrices used for mass scans to investigate the molecule formation within the ion source.

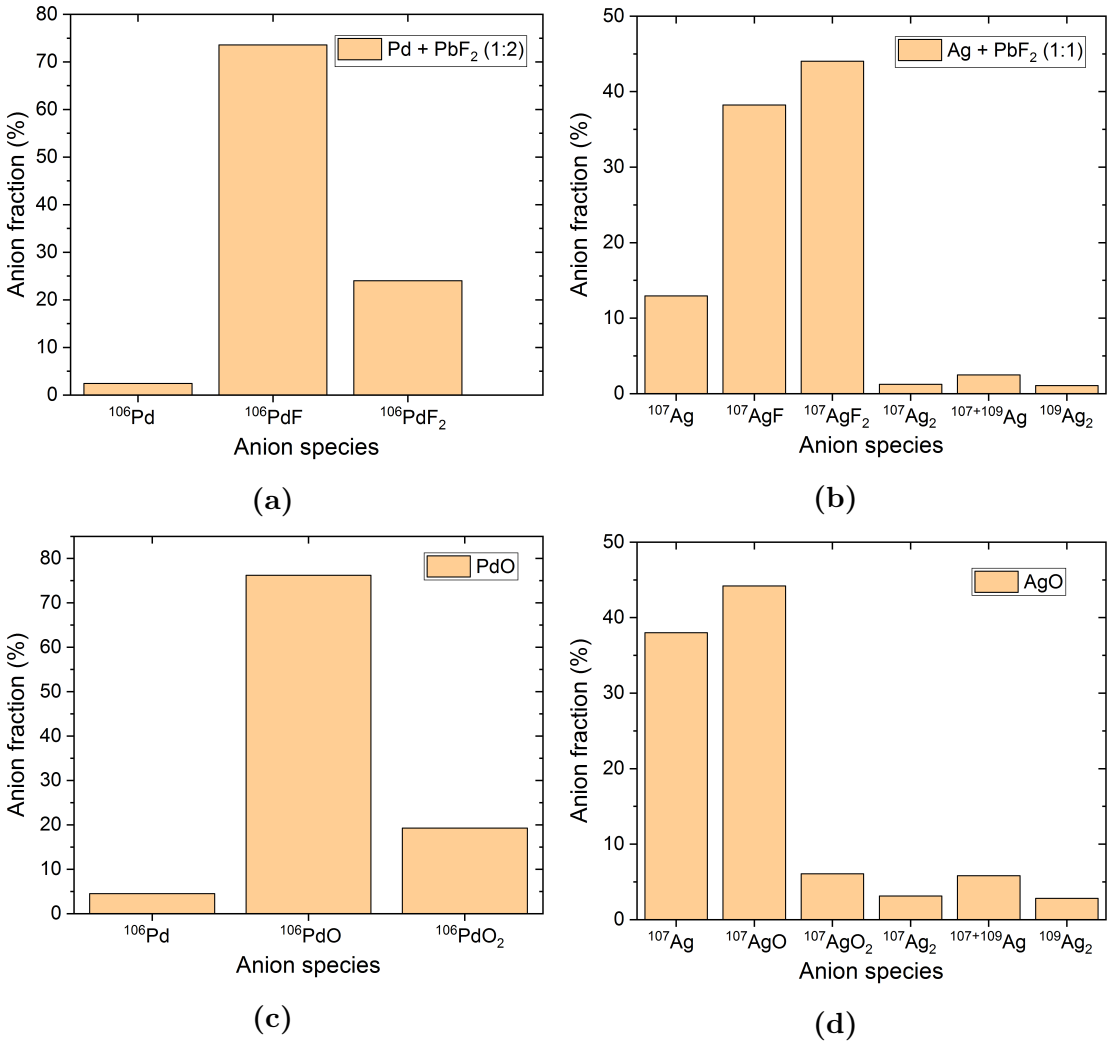

Figure 5.2.: Results of the mass scans for (a) PdF_x^-, (b) AgF_x^-, (c) PdO_x^- and (d) AgO_x^-. The diagrams are normalized to the total current output of all detected molecules represented in the diagrams.

The oxide results are very similar to the fluorides, especially for PdO_x^-. There are no higher oxide molecules formed within the ion source than di-oxides. PdO^- forms almost exclusively with a yield of around 70 %. In contrast to the fluorides a lot of elemental Ag^- and AgO^- is formed with roughly 38 % and 45 % yield respectively.
The results of the mass scans suggest that, if possible, the oxide molecules should be used, because PdO^- and PdO_2^- have high currents in the range of nA. The corresponding isobaric molecules are suppressed by a factor of 2 - 3 out of the ion source which is not much, but the situation for the fluorides is reversed where much more AgF_x^- than PdF_x^- is formed within the ion source.

5.1.3. Isobar suppression

The electron affinities (EA) of all formed molecules, with the exception of Ag_2^-, were tested with the 532-nm laser and the EAs of the oxides were additionally tested with the 355-nm laser. Both lasers were operated at 10 W. The results are shown in Fig. 5.3. All currents were measured in FC 02-1 such that the anions reaching the Faraday cup must have the right m/q ratio. An overview of the electron affinity limits for all tested molecules is given in Tab. 5.3.

The EAs shown in Tab. 5.1 are in agreement with the tests done as both PdO^- and AgO^- were detached with the 532-nm laser (2.33 eV) and PdO_2^- was detached with the 355-nm laser (3.49 eV). Unfortunately AgO_2^- is only slightly affected by the 355-nm laser, meaning that the EA is very likely somewhere around 3.49 eV and hence higher than the EA of PdO_2^-.
The fluorides PdF_2^- and AgF_2^- are unaffected by the 532-nm laser leaving only the mono-fluorides as a possibility for the green laser. Although more than half of the PdF^- current is detached, there still remain around 6 nA and the m/q ratio suggests that the measured current is indeed PdO^-. Therefore, without additional tests on the di-fluorides with the 355-nm laser, PdF^- might be the only suitable molecule for measuring ^{107}Pd at VERA with the current setup available.
To conclude, the oxide molecules are not suitable with ILIAMS. The difference of the EAs between PdO^- and AgO^- is very small (see Tab. 5.1). For such small

molecule	EA limit (eV)	molecule	EA limit (eV)
PdO^-	<2.33	AgO^-	<2.33
PdO_2^-	$2.33<EA(PdO_2^-)<3.49$	AgO_2^-	$\gtrsim 3.49$
PdF^-	$\lesssim 2.33$	AgF^-	<2.33
PdF_2^-	>2.33	AgF_2^-	>2.33

Table 5.3.: Experimental electron affinity limits for various fluoride and oxide molecules of palladium and silver.

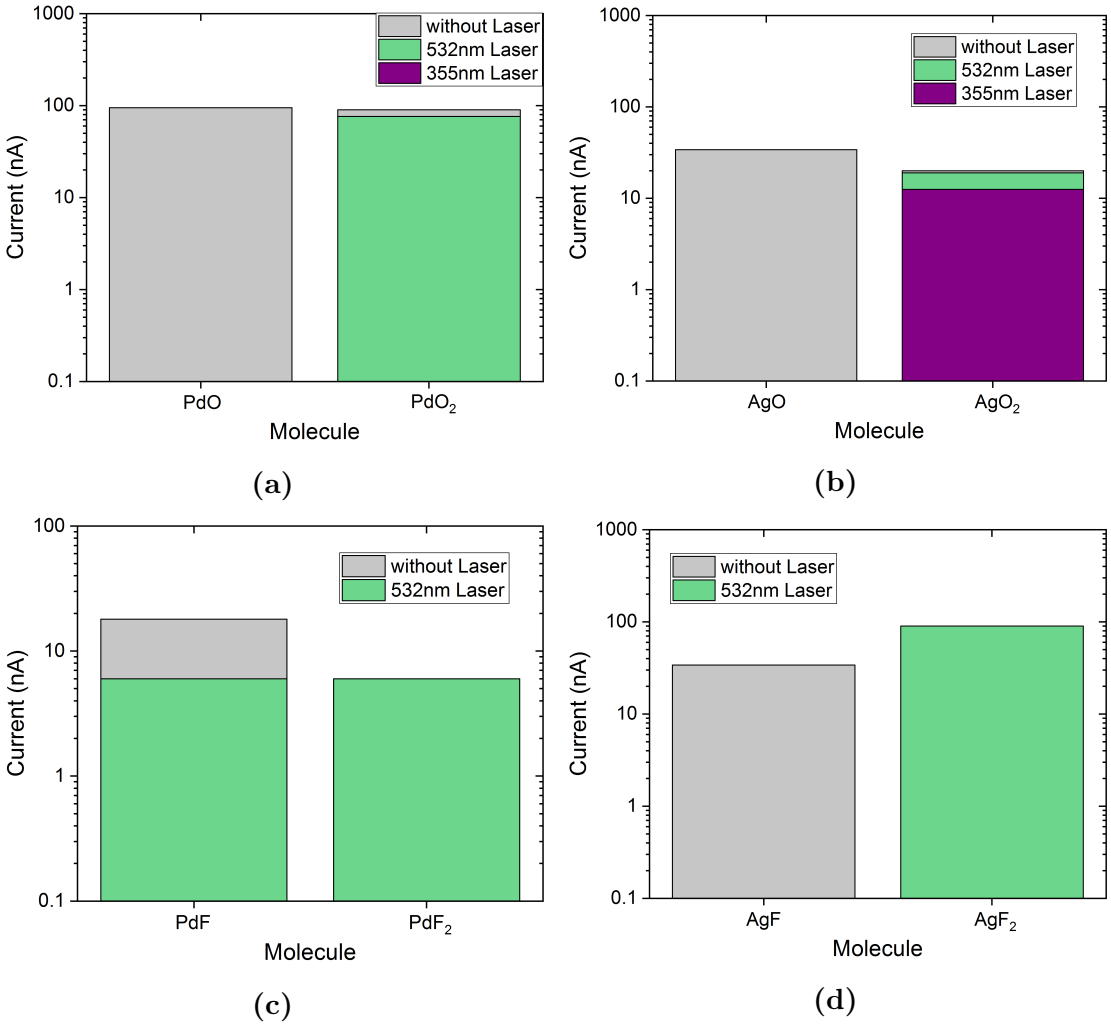

Figure 5.3.: Results of the laser photodetachment tests for (a) PdO_x^-, (b) AgO_x^-, (c) PdF_x^- and (d) AgF_x^-. The plots show the measured currents without laser (gray), with the 532-nm laser (green) and with the 355-nm laser (purple) both operated at 10 W. Note the logartihmic scale for the ion current.

differences it is nearly impossible to find a laser that would only detach the isobar AgO^-. However, it seems possible to buy a dedicated laser with the right photon energies for the molecules PdF^- and AgF^-, because the data strongly indicates that the EA of AgF^- is lower than for PdF^-.

5.1.4. Transmission

Data has been collected for both the ion cooler and accelerator transmission, but since EA tests were the main focus of the beam time, not all settings of the ion cooler were fully optimized for highest transmissions.

Ion cooler transmission

The ion cooler transmission was calculated with equation (3.2) and a summary can be found in Tab. 5.4. During the measurements pure He was used as buffer gas at a gas pressure of around 0.30 mbar. Unfortunately the molecule PdF^- has by far the lowest transmission, but this setup might have been poorly tuned.

molecule	**transmission (%)**	**molecule**	**transmission (%)**
PdO^-	47.5	AgO^-	31.5
PdO_2^-	40.0	AgO_2^-	33.0
PdF^-	16.0	AgF^-	12.0
PdF_2^-	35.0	AgF_2^-	29.0

Table 5.4.: Ion cooler transmissions of the oxide and fluoride molecules of Pd and Ag. The data was taken in the beam time Pd1901 with 0.30 mbar of pure He as buffer gas.

Accelerator transmission

When injecting PdO^- into the accelerator the transmission was calculated with equation (3.3) for ^{106}Pd in the charge states +2 and +3 using different stripper gases at different pressures. The two stripper gases were He and O_2 at pressures between 3×10^{-8} and 2×10^{-7} T at IGC 03-1. The terminal voltage of the accelerator was set to 2.6951 MV for Pd^{3+} and to 2.3873 MV for Pd^{2+}. This was needed, because otherwise the bending magnet would not have been able to deflect the Pd^{2+} into FC 04-1. The results can be seen in Fig. 5.4.

The best transmission with O_2 for both charge states are at the lowest measured gas pressure of 3×10^{-8} T and they are almost linearly increasing with decreasing pressure. Their maxima are around 23 % and 18 % for Pd^{2+} and Pd^{3+} respectively at 3×10^{-8} T. The better suited stripper gas is He as it not only shifts the maxima back to higher pressures, but also increases the +3 charge state transmission at similar terminal voltages to almost the same level as for the +2 charge state. Both maxima with He gas can be found at a stripper gas pressure of 5×10^{-8} T and are roughly 22 %. By increasing the terminal voltage to 3 MV the Pd^{3+} transmission increases slightly to 24 %.

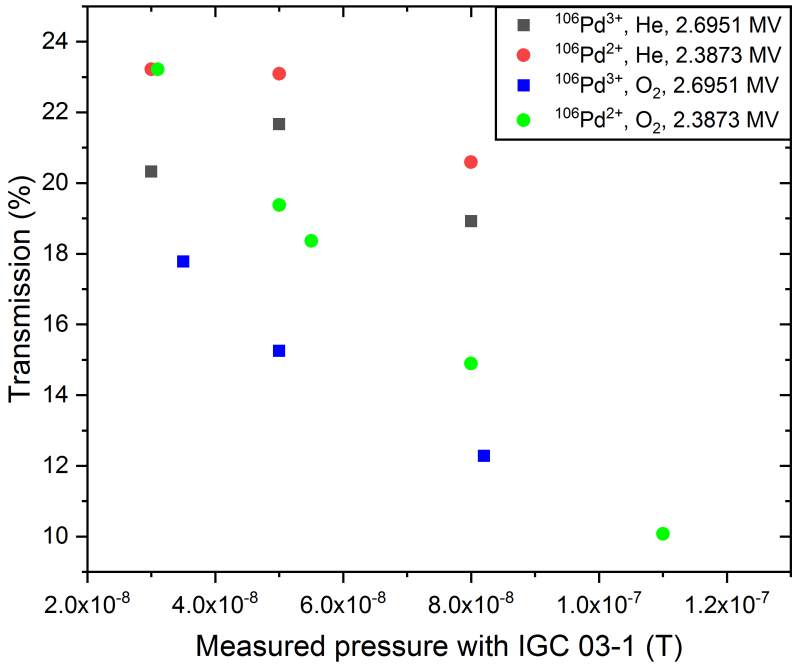

Figure 5.4.: Picture of the accelerator transmission for $^{106}Pd^{2+,3+}$ at different stripper gas pressures readings (IGC 03-1) for He (squares) and O_2 (circles) as stripper gases, when injecting PdO^-. The terminal voltages are different for the charge states, because at 2.6951 MV the Pd^{2+} ions could not pass the analyzing magnet.

6. Conclusion and Outlook

In this master thesis the long lived fission products ^{90}Sr, ^{99}Tc and ^{107}Pd have been investigated to different degrees. Therefore the conclusion and outlook will be written for each fission product separately.

^{90}Sr

With ILIAMS it was possible to make an entirely new trace isotope (^{90}Sr) accessible at VERA.
When starting to work on ^{90}Sr it was clear that SrF_3^- is a suitable molecule to use with the ILIAMS setup. At first the sample matrix was a mixture of SrF_2 and PbF_2, but mass scans revealed that, contrary to the literature, additionally a lot of SrF^- was formed in the ion source. This problem was solved by mixing SrF_2 and PbF_2 1:8 by weight instead of 1:3. Ionization yield measurements verified the increased SrF_3^- formation seen in the mass scans. The yield of the 1:8 mixture reaches around 1 % and is almost twice as high as the yield of the 1:3 mixture. The extraction of SrF_3^- suppresses both isobars ^{90}Y and ^{90}Zr by 10^3 due to poor tri-fluoride formation in the ion source.
The transmission of SrF_3^- through the ion cooler and of Sr^{3+} through the accelerator were investigated and improved. Currents around 150 nA reach up to 35 % transmission through the ion cooler, compared to around 50 % and 80 % for $^{26}AlO^-$ and $^{36}Cl^-$ respectively. The accelerator transmission is up to 25 % in the +3 charge state with He as stripper gas at a gas pressure of 5×10^{-8} T and a terminal voltage of 3 MV.
The interfering isobars ^{90}Y and ^{90}Zr can be suppressed by several orders of magnitude via laser photodetachment using either the 532-nm or the 355-nm laser. 0.30 mbar of a He+O_2 (30:1) mixture is used as buffer gas instead of pure He. The

gas mixture alone suppresses ^{90}Y and ^{90}Zr $>1.5\times10^{3}$ and $>5\times10^{5}$ respectively and either laser suppresses them further. Therefore a ^{90}Zr suppression of 1×10^{7} is achieved by the ILIAMS setup.
First in-house made reference materials with isotopic ratios of ^{90}Sr/Sr between 10^{-11} and 10^{-14} were produced and measured. With these and blanks (SrF_2, Alfa Aesar) AMS measurements were conducted. When normalized to the highest ratio material, all reference materials agree within $1\,\sigma$ uncertainty with their nominal values. A blank level of $^{90}\mathrm{Sr/Sr} = (4.5 \pm 3.2)\times10^{-15}$ is reached. This corresponds to a limit of detection of <0.1 mBq, improving the previous limit of detection by more than an order of magnitude. Thus, AMS is now the most sensitive technique for measuring ^{90}Sr, surpassing the established method of decay counting and other methods e.g. ICP-MS.
In the near future, first AMS measurements of environmental samples will be made. Additionally a cross calibration of the in-house made reference materials will be conducted, as well as a re-investigation of the reproducibility. Provided that the sample preparation and measurements of the environmental samples work as well as the in-house made materials, it will be possible to routinely measure ^{90}Sr at VERA.

^{99}Tc

Fundamental tests of the sputter yields and the electron affinities of oxide and fluoride molecules formed within the ion source have been conducted for future AMS measurements of ^{99}Tc at VERA.
The molecule formation in the ion source shows that adding Nb to Ru matrices suppresses the formation of specific oxide and fluoride molecules, e.g. RuO^- and RuF_3^-. In contrast to this effect, the oxide and fluoride molecule formation for Nb improves in the Nb-added Ru matrices, e.g. for NbO_2^- and NbF_4^-
The electron affinities of all isobaric molecules formed within the ion source have been investigated with a laser. Since the electron affinities of the corresponding Tc molecules are unknown it is not possible to dismiss any of the molecules as not suitable yet.

This provides a good basis for future work to measure ^{99}Tc at VERA, which is part of an ongoing FWF project. Within this project the electron affinities of the oxide and fluoride molecules of Tc will be tested to find out if a suitable molecular system exists. Since there are no stable Tc isotopes this was beyond the scope of this thesis. Only after a suitable molecule has been found other parameters like ion cooler and accelerator transmissions can be thoroughly investigated.

^{107}Pd

Like for ^{99}Tc, the main investigations revolved around finding suitable molecular systems to potentially do AMS measurements of ^{107}Pd in the future.
Mass scans show that the oxide molecules have a higher formation yield in the ion source than the fluorides. However, their electron affinities are not suitable with the current lasers available. The data points to an electron affinity of the isobar AgO_2^- around 3.49 eV while it is lower for PdO_2^-. Both mono-oxide molecules are detached by 2.33 eV photons. With the current knowledge and ILIAMS setup a possible molecular system might be PdF^-. The molecules PdF_2^- and AgF_2^- remain to be tested with the 355-nm laser.
Preliminary values for the ion cooler transmissions are that, besides PdF^- and AgF^- with 16 % and 12 % respectively, all other molecules had ion cooler transmissions of 30 % or higher using 0.30 mbar of pure He. The accelerator transmission was only investigated injecting PdO^-. He turns out to be a better stripper gas than O_2 reaching transmissions around 22 % for the +2 and +3 charge states.
In the future the electron affinities of the molecules PdF_2^- and AgF_2^- have to be tested with the 355-nm laser to see whether this molecular system is suitable or not. Depending on the result either only PdF^- or also PdF_2^- could be investigated further with the current ILIAMS setup. Alternatively, one could potentially buy a dedicated laser with the right photon energy for the molecular system PdF^- and AgF^-. This might also be possible for the system PdO^- and AgO^-, although their reported difference in EA is only 0.018 eV. It is important to test different sample matrices for an improved PdF_x^- output from the ion source, because the fluoride output was a factor of 12 lower than for the oxides.

A. ^{90}Sr measurement data evaluation

This appendix is designed to give a better overview of the measurement evaluation for ^{90}Sr. The raw data is accessed via the VERA homepage where it is saved in the beam time folder selected during the measurement. Knowledge about the procedure of the measuring routine is helpful and can be found in section 3.2.5.
The typical AMS evaluation of an unknown sample is done with standard material for normalization and blank material for the background. Since no environmental samples have been measured yet our different dilution materials were treated like unknown samples, while only the highest reference material (i.e. $^{90}\mathrm{Sr}/\mathrm{Sr} = 10^{-11}$) was used for normalization. In addition, Zr-spiked targets were also measured in order to be able to accurately assess the ^{90}Sr region of interest (ROI)
During the automatic measurement a lot of data is taken and stored in the beam time folder, but not necessarily needed for the evaluation itself. The data important for the evaluation are the events of ^{90}Sr in the detector ($\mathrm{N_{90Sr}}$), the events of ^{90}Zr in the detector ($\mathrm{N_{90Zr}}$) the time measured ($\mathrm{t_{meas}}$), the high energy side current of the stable ^{88}Sr ($\mathrm{I_{88Sr}}$) and the high energy charge state (Q). All calculations were usually made with Microsoft Excel.
At first the $^{90}\mathrm{Sr}/^{90}\mathrm{Zr}$ ratio for the Zr-spiked targets

$$\left(^{90}\mathrm{Sr}/^{90}\mathrm{Zr}\right)_{\text{spike, run}} = \frac{\mathrm{N_{90Sr,\ run}}}{\mathrm{N_{90Zr,\ run}}} \tag{A.1}$$

was calculated for each run to see how much ^{90}Zr is counted as ^{90}Sr by mistake, because of the tightly set ROI. The average over $\left(^{90}\mathrm{Sr}/^{90}\mathrm{Zr}\right)_{\text{spike, run}}$ in each turn results in the, typically small, turnwise Zr correction factor ($\mathrm{K_{Zr,\ turn}}$). This factor is used to correct the number of ^{90}Sr events detected ($\mathrm{N_{90Sr,\ Zr\ corr}}$) for events caused

by ^{90}Zr in the ^{90}Sr ROI.

$$N_{90Sr,\ Zr\ corr} = N_{90Sr} - K_{Zr,\ turn} \cdot N_{90Sr} \tag{A.2}$$

The corrected number of ^{90}Sr events is used to calculate the ^{90}Sr count rate

$$R_{90Sr,\ Zr\ corr,\ run} = \frac{N_{90Sr,\ Zr\ corr}}{t_{meas}} \tag{A.3}$$

for each run. The count rate is needed to calculate the ^{90}Sr/^{88}Sr ratio

$$\left(^{90}Sr/^{88}Sr\right)_{Zr\ corr,\ run} = \frac{R_{90Sr,\ Zr\ corr,\ run} \cdot Q \cdot e}{I_{88Sr}} \tag{A.4}$$

for the corresponding run where e denotes the elementary charge. This is done for the standard (i.e. 10^{-11} reference material), samples and blanks such that for all cathodes in each run and turn the Zr corrected ratio is gained.
Next is the additional blank correction for the total corrected ratios. The average over all Zr corrected blank measurements $\left(\overline{\left(^{90}Sr/^{88}Sr\right)}_{Blank,\ Zr\ corr}\right)$ is calculated and subtracted from the from the sample and standard ratios.

$$\left(^{90}Sr/^{88}Sr\right)_{Stand./Sample,corr} = \left(^{90}Sr/^{88}Sr\right)_{Stand./Sample,Zr\ corr} - \overline{\left(^{90}Sr/^{88}Sr\right)}_{Blank,Zr\ corr} \tag{A.5}$$

With the corrected ratios of the standard a turnwise normalization factor ($K_{Sr,\ turn}$) can be calculated. First a weighted average of the standard is calculated for each turn $\left(\overline{\left(^{90}Sr/^{88}Sr\right)}_{Standard,\ corr,\ turn}\right)$. The typically used weight (w_i) was the collected charge, i.e. product of high energy side current and the time measured. Afterwards the turnwise normalization factor was calculated as the ratio between the nominal ratio over the measured one.

$$K_{Sr,\ turn} = \frac{\left(^{90}Sr/^{88}Sr\right)_{Standard,\ corr,\ turn,\ nominal}}{\overline{\left(^{90}Sr/^{88}Sr\right)}_{Standard,\ corr,\ turn,\ measured}} \tag{A.6}$$

All ratios of the samples are then multiplied with the turnwise normalization factor to get the normalized and corrected ratio for each run of the corresponding turn $\left(\left(^{90}\mathrm{Sr}/^{88}\mathrm{Sr}\right)_{\text{Sample, norm}}\right)$.

$$\left(^{90}\mathrm{Sr}/^{88}\mathrm{Sr}\right)_{\text{Sample, norm}} = \left(^{90}\mathrm{Sr}/^{88}\mathrm{Sr}\right)_{\text{Sample, corr, run}} \cdot \mathrm{K}_{\text{Sr, turn}} \tag{A.7}$$

In the final step a weighted average over all runs and turns of the same cathode $\left(\overline{\left(^{90}\mathrm{Sr}/^{88}\mathrm{Sr}\right)}_{\text{Sample, final}}\right)$ was calculated

$$\overline{\left(^{90}\mathrm{Sr}/^{88}\mathrm{Sr}\right)}_{\text{Sample, final}} = \frac{\sum_{\mathrm{i}} \left(^{90}\mathrm{Sr}/^{88}\mathrm{Sr}\right)_{\text{Sample, norm, i}} \cdot \mathrm{w_i}}{\sum_{\mathrm{i}} \mathrm{w_i}} \tag{A.8}$$

again with the total collected ^{88}Sr charge as weight.
An overall result $\left(\overline{\left(^{90}\mathrm{Sr}/^{88}\mathrm{Sr}\right)}_{\text{Sample, overall}}\right)$ can be calculated, if more than one cathode contains the same sample material. This is done by calculating the weighted average of all final results of the same material, e.g. average over all final results with identical 10^{-12} reference material. Typically a weighted average with $\frac{1}{(\text{rel. uncert.})^2}$ as weight was used.

$$\overline{\left(^{90}\mathrm{Sr}/^{88}\mathrm{Sr}\right)}_{\text{Sample, overall}} = \frac{\sum_{\mathrm{i}} \left(^{90}\mathrm{Sr}/^{88}\mathrm{Sr}\right)_{\text{Sample, final, i}} \cdot \mathrm{w_i}}{\sum_{\mathrm{i}} \mathrm{w_i}} \tag{A.9}$$

This was done to obtain the results given in Fig. 3.13 and Fig. 3.15.
The uncertainties of the results are either the Gaussian propagation of the counting statistic or the statistic uncertainty of the mean value from scatter, depending on which of them is higher.

B. Ionization yield data evaluation

This appendix is designed to give an overview of the evaluation of the ionization yield measurements. The mass scan data is stored in the beam time folders of the corresponding beam times and a Microsoft Excel template exists that calculates the ionization yield. A checklist for ionization yield measurements can be found on the VERA homepage under VERA_Manuals/procedures/Checklist for Ionisation Yield Measurements at S2.html. The evaluation is shown for $^{88}SrF_3^-$ done in the beam time Sr1906, but can be applied to any other isotope by changing the beam time folders and isotopes accordingly.

After the measurement is completed the the measured data usually stored on dataaxel has to be copied over to dataVERA2. This can be done by typing the command „cp -rvp cat?? /dataVERA2/Sr/Sr1906“ as csadmin@axel in a xterm window.

The next step is to copy the file „extract_peak_mass145“ from an older ionization yield measurement and make a few changes. The things that need to be changed in the file are the „MASS“ (mass of the element or molecule of interest), „HVS_PATTERN“ (HVS range of the peak in the mass scan that is evaluated), „export CATS“ (cathodes measured) and „TURNS“ (turns measured). Afterwards using the command „extract_peak_mass145“ as csadmin@VERA2 in the according beam time folder (e.g. /dataVERA2/Sr/Sr1906) starts running the extraction file and creates the file „mass145_cur_vs_time.txt“ in the beam time folder. This new file contains the cathodes and the current of the evaluated peak for every measured scan. These current values are then used for the data evaluation of the ionization yield.

The evaluation itself is pretty straightforward since the ionization yield is just the ratio of the collected $^{88}SrF_3^-$ charge over the theoretically producible $^{88}SrF_3^-$ charge.

First a few minor calculations have to be made. One of them is the average time of one scan ($\bar{t}_{scan}$). The other one is the number of ^{88}Sr atoms in the matrix of the sputtered sample ($N_{^{88}Sr}$). The calculation of the number of ^{88}Sr atoms in the sample can be split into two steps. At first the mass of ^{88}Sr ($m_{^{88}Sr}$) in the sample is calculated and to do so the fraction of SrF_2 in the (SrF_2+PbF_2)-matrix (f_{SrF_2}) and the fraction of ^{88}Sr in SrF_2 ($f_{^{88}Sr}$) have to be known. The fraction f_{SrF_2} is obtained by

$$f_{SrF_2} = \frac{m_{SrF_2}}{m_{SrF_2} + m_{PbF_2}} \tag{B.1}$$

where m_{SrF_2} and m_{PbF_2} are the masses of the two materials mixed together to form the matrix. The fraction $f_{^{88}Sr}$ is calculated with

$$f_{^{88}Sr} = \frac{M_{Sr}}{M_{SrF_2}} \cdot A_{^{88}Sr} \tag{B.2}$$

where M_{Sr} and M_{SrF_2} denote the molar masses of the corresponding element/molecule and $A_{^{88}Sr}$ is the natural abundance of ^{88}Sr. With these two fractions and the mass of the sample (m_{sample}) put into the cathode, the mass of ^{88}Sr inside the sample can be calculated as follows.

$$m_{^{88}Sr} = m_{sample} \cdot f_{SrF_2} \cdot f_{^{88}Sr} \tag{B.3}$$

After that the number of ^{88}Sr atoms is obtained by

$$N_{^{88}Sr} = \frac{m_{^{88}Sr} \cdot N_A}{M_{Sr}} \tag{B.4}$$

where N_A is the Avogadro constant. The ionization yield increment of each individual scan i ($Y_{^{88}SrF_{3,\,i}}$) can be calculated by

$$Y_{^{88}SrF_{3,\,i}} = \frac{\bar{t}_{scan} \cdot I_{peak,\,i}}{N_{^{88}Sr} \cdot e} \tag{B.5}$$

where $I_{peak,\,i}$ is the current of the $^{88}SrF_3^-$ peak of scan i found in the „mass145_cur_vs_time.txt“ file and e is the elementary charge. The last step is to calculate the cumulative ionization yield ($Y_{^{88}SrF_3}$) by building the sum over the increment ionization yields of each scan.

$$Y^{88}_{SrF_3} = \sum_i Y^{88}_{SrF_3,\,i} \tag{B.6}$$

In order to make a plot of the cumulative ionization yield against the sputter time ($t_{sputter}$) the sputter time has to be calculated for each scan by the following equation

$$t_{sputter,\,i} = i \cdot \bar{t}_{scan} \tag{B.7}$$

where the index i denotes the cumulative sputter time at scan i.

C. Machine setups for Sr measurement

This appendix gives an overview of the typical settings of components during a ^{90}Sr measurement at VERA. The most important AMS components are listed in Tab. C.1 for the stable ^{88}Sr and rare ^{90}Sr setup. The ILIAMS components are listed in Tab. C.2.

	value	
component	**^{88}Sr**	**^{90}Sr**
HPB I1-1|MfieldR	8685 G	8747 G
ESA 01-1|VC	5.155 kV	
ESA 01-2|VC	5.062 kV	
HPB 01-1|MfieldR	7354 G	
MBS 01-1|VCreg0	6.015 kV	5.528 kV
ESX 02-1|VCreg0	69.720 V	54.292 V
ESY02-1|VCreg0	150.426 V	150.426 V
TPS TK-1|GvmVC	2.992 MV	2.924 MV
HPB 03-1|MfieldR	11672 G	
ESY 04-1|YVC	1.241 kV	1.213 kV
ESA 04-1|VC	82.187 kV	80.341 kV

Table C.1.: Typical values of the main AMS components at VERA.

category	component	value
Ion Source S2	CAT S2-1|VC 01-1	−4.61 kV
	EXT S2-1|VC	−12.61 kV
	HVS S2-1|VC	−12.63 kV
	FOC S2-1|VC	0.30 kV
	ION S2-1|VC	30 A
	OVN S2-1|VC	33 V
	LNH S2-1|VC	25 A
RFQ ion guide	RFQ I1-1|FreqC	1547 kHz
	RFQ I1-1|AmplVC	0.0593 V
	RFQ I1-1|HVVC	29.97 kV
	RFQ I1-1|InjHVC	4.10 kV
	RFQ I1-1|InjLVC	1.23 kV
	RFQ I1-1|GElecVC	150 V
	RFQ I1-1|ExtLVC	1.09 kV
	RFQ I1-1|ExtHVC	2.93 kV
Ion optics & filter	ESX S2-1|XVC	−323 V
	ESY S2-1|YVC	−107 V
	ESX I1-1|XVC	507 V
	ESY I1-1|YVC	−63 V
	ESX I1-2|XVC	602 V
	ESY I1-2|YVC	−1034 V
	ESX I2-1|XVC	0.02 kV
	ESY I2-1|YVC	−0.15 kV
	EL I2-1|VC	−8.09 kV
	EL I2-2|VC	−8.22 kV
	ESA I2-1|VC	5.022 kV

Table C.2.: Typical values of the ILIAMS components during a ^{90}Sr measurement excluding the bending magnet BM I1-1.

Bibiliography

Alary, J.-F. et al. (2015). "Isobar Separator for Anions: Current status". *Nuclear Instruments and Methods in Physics Research Section B: Beam Interactions with Materials and Atoms* 361, pp. 197–200. ISSN: 0168-583X. URL: https://doi.org/10.1016/j.nimb.2015.03.059.

Andersen, H. H. et al. (1997). "Structural properties of the negative strontium ion: Binding energy and fine-structure splitting". *Phys. Rev. A* 55 (4), pp. 3247–3249. URL: https://link.aps.org/doi/10.1103/PhysRevA.55.3247.

Andersen, T. et al. (1999). "Binding Energies in Atomic Negative Ions: III". *Journal of Physical and Chemical Reference Data* 28 (6), pp. 1511–1533. URL: https://doi.org/10.1063/1.556047.

Andersson, P. et al. (2010). "Nearly complete isobar suppression by photodetachment". *Journal of Applied Physics* 107 (2), p. 026102. URL: https://doi.org/10.1063/1.3291104.

Andrews, D. H. et al. (2002). "On the photoelectron spectrum of AgO^-". *The Journal of Chemical Physics* 117 (8), pp. 4074–4076. URL: https://doi.org/10.1063/1.470975.

Bilodeau, C. et al. (1998). "Infrared laser photodetachment of transition metal negative ions: studies on Cr^-, Mo^-, Cu^- and Ag^-". *Journal of Physics B: Atomic, Molecular and Optical Physics* 31 (17), pp. 3885–3891. URL: https://doi.org/10.1088%2F0953-4075%2F31%2F17%2F013.

Borshchevskii, A. Y. et al. (1988). "Thermochemical quantities for gas-phase iron, uranium, and molybdenum fluorides, and their negative ions". *The Journal of Chemical Thermodynamics* 20 (5), pp. 523–537. ISSN: 0021-9614. URL: https://doi.org/10.1016/0021-9614(88)90080-8.

Bu, W. et al. (2016). "Mass spectrometry for the determination of fission products ^{135}Cs, ^{137}Cs and ^{90}Sr: A review of methodology and applications". *Spectrochimica*

Acta Part B: Atomic Spectroscopy 119, pp. 65–75. ISSN: 0584-8547. URL: https://doi.org/10.1016/j.sab.2016.03.008.

Bush, R. P. (1991). "Recovery of Platinum Group Metals from High Level Radioactive Waste". *Platinum Metals Rev.* 35 (4), pp. 202–208. URL: https://www.ingentaconnect.com/content/matthey/pmr/1991/00000035/00000004/art00009#.

Campbell, J. E. et al. (1959). "The occurrence of strontium-90, iodine-131, and other radionuclides in milk-May, 1957, through April, 1958". *American Journal of Public Health* 49, pp. 225–235. URL: https://ajph.aphapublications.org/doi/pdf/10.2105/AJPH.49.2.225.

Chen, F. et al. (2000). "Near-field behavior of ^{99}Tc during the oxidative alteration of spent nuclear fuel". *Journal of Nuclear Materials* 278 (2), pp. 225–232. ISSN: 0022-3115. URL: https://doi.org/10.1016/S0022-3115(99)00264-0.

Coakley, A. J. et al. (1989). "^{99m}Tc sestamibi–a new agent for parathyroid imaging". *Nuclear medicine communications* 10 (11), pp. 791–794. ISSN: 0143-3636. URL: http://europepmc.org/abstract/MED/2532313.

Cornett, R. J. et al. (2019). "A preliminary study of ^{99}Tc measurement using matrix-assisted low energy AMS". *Nuclear Instruments and Methods in Physics Research Section B: Beam Interactions with Materials and Atoms* 455, pp. 181–189. ISSN: 0168-583X. URL: https://doi.org/10.1016/j.nimb.2018.12.028.

Crouch, E. A. C. (1977). "Fission-product yields from neutron-induced fission". *Atomic Data and Nuclear Data Tables* 19 (5), pp. 417–532. ISSN: 0092-640X. URL: https://doi.org/10.1016/0092-640X(77)90023-7.

Dahlgaard, H. (1994). "Sources of ^{137}Cs, ^{90}Sr and ^{99}Tc in the East Greenland Current". *Journal of Environmental Radioactivity* 25 (1), pp. 37–55. ISSN: 0265-931X. URL: https://doi.org/10.1016/0265-931X(94)90006-X.

Dawson, P. H. (1976). *Quadrupole mass spectrometry and its applications*. Elsevier Scientific Publishing Company.

Dewiere, L. et al. (2004). "^{90}Sr migration to the geo-sphere from a waste burial in the Chernobyl exclusion zone". *Journal of Environmental Radioactivity* 74 (1), pp. 139–150. ISSN: 0265-931X. URL: https://doi.org/10.1016/j.jenvrad.2004.01.019.

Egorov, V. N. et al. (1999). "^{90}Sr and ^{137}Cs in the Black Sea after the Chernobyl NPP accident: inventories, balance and tracer applications". *Journal of Environmental Radioactivity* 43 (2), pp. 137–155. ISSN: 0265-931X. URL: https://doi.org/10.1016/S0265-931X(98)00088-5.

Eliades, J. A. et al. (2015). "Negative ion-gas reaction studies using ion guides and accelerator mass spectrometry I: SrF_3^-, YF_3^-, ZrF_3^-, YF_4^- and ZrF_5^- in NO_2". *Nuclear Instruments and Methods in Physics Research Section B: Beam Interactions with Materials and Atoms* 361, pp. 294–299. ISSN: 0168-583X. URL: https://doi.org/10.1016/j.nimb.2015.06.025.

Eliades, J. et al. (2013). "On-line ion chemistry for the AMS analysis of ^{90}Sr and ^{135,137}Cs". *Nuclear Instruments and Methods in Physics Research Section B: Beam Interactions with Materials and Atoms* 294, pp. 361–363. ISSN: 0168-583X. URL: https://doi.org/10.1016/j.nimb.2011.11.030.

England, T. R. and B. F. Rider (1995). "Evaluation and compilation of fission product yields 1993 (LA-SUB–94-170)". URL: http://inis.iaea.org/search/search.aspx?orig_q=RN:26035261.

Feigerle, C. S. et al. (1981a). "Laser photoelectron spectrometry of Sc^-, and Y^-: A determination of the order of electron filling in transition-metal anions". *Journal of Electron Spectroscopy and Related Phenomena* 23 (3), pp. 441–450. ISSN: 0368-2048. URL: https://doi.org/10.1016/0368-2048(81)85050-5.

Feigerle, C. S. et al. (1981b). "Binding energies and structure of transition metal negative ions". *The Journal of Chemical Physics* 74 (3), pp. 1580–1598. URL: https://doi.org/10.1063/1.441289.

Forstner, O. et al. (2015). "The ILIAS project for selective isobar suppression by laser photodetachment". *Nuclear Instruments and Methods in Physics Research Section B: Beam Interactions with Materials and Atoms* 361, pp. 217–221. ISSN: 0168-583X. URL: https://doi.org/10.1016/j.nimb.2015.04.021.

García-Léon, Manuel (2005). "^{99}Tc in the Environment: Sources, Distribution and Methods". *Journal of Nuclear and Radiochemical Sciences* 6 (3), pp. 253–259. DOI: 10.14494/jnrs2000.6.3_253.

Gunion, R. F. et al. (1996). "Ultraviolet photoelectron spectroscopy of molybdenum and molybdenum monoxide anions". *The Journal of Chemical Physics* 104 (5), pp. 1765–1773. URL: https://doi.org/10.1063/1.470975.

Haynes, W. M. et al. (2016). *CRC Handbook of Chemistry and Physics*. 97^{th} edition (2016-2017), p.14-17. CRC Press.

Herfurth, F. et al. (2001). "A linear radiofrequency ion trap for accumulation, bunching, and emittance improvement of radioactive ion beams". *Nuclear Instruments and Methods in Physics Research Section A: Accelerators, Spectrometers, Detectors and Associated Equipment* 469 (2), pp. 254–275. ISSN: 0168-9002. URL: https://doi.org/10.1016/S0168-9002(01)00168-1.

Hirose, K. (2012). "2011 Fukushima Dai-ichi nuclear power plant accident: summary of regional radioactive deposition monitoring results". *Journal of Environmental Radioactivity* 111, pp. 13–17. ISSN: 0265-931X. URL: https://doi.org/10.1016/j.jenvrad.2011.09.003.

Hu, Q.-H. et al. (2010). "Sources of anthropogenic radionuclides in the environment: a review". *Journal of Environmental Radioactivity* 101 (6), pp. 426–437. ISSN: 0265-931X. URL: https://doi.org/10.1016/j.jenvrad.2008.08.004.

Ionplus (n.d.). https://www.ionplus.ch/milea. Accessed: 2020-01-15.

JAEA-Nuclear Data Center (2012). https://wwwndc.jaea.go.jp/cgi-bin/FPYfig. Accessed: 2019-10-08.

JANIS 4.0 (2013). http://www.oecd-nea.org/janisweb/book/neutrons/U235/MT1/renderer/2450. Accessed: 2019-09-30.

Kelly, S. et al. (2005). "Tracing the geographical origin of food: The application of multi-element and multi-isotope analysis". *Trends in Food Science & Technology* 16 (12), pp. 555–567. ISSN: 0924-2244. URL: https://doi.org/10.1016/j.tifs.2005.08.008.

Kim, C. K. et al. (1991). "Application of a high resolution inductively coupled plasma mass spectrometer to the measurement of long-lived radionuclides". *J. Anal. At. Spectrom.* 6 (3), pp. 205–209. URL: http://dx.doi.org/10.1039/JA9910600205.

Knie, K. et al. (1997). "AMS at the Munich gas-filled analyzing magnet system GAMS". *Nuclear Instruments and Methods in Physics Research Section B: Beam Interactions with Materials and Atoms* 123 (1), pp. 128–131. ISSN: 0168-583X. URL: https://doi.org/10.1016/S0168-583X(96)00753-7.

Kolarik, Z. and R. V. Edouard (2003a). "Recovery of Value Fission Platinoids from Spent Nuclear Fuel". *Platinum Metals Rev.* 47 (2), pp. 74–87. URL: https:

//www.ingentaconnect.com/content/matthey/pmr/2003/00000047/00000002/art00010.

Kolarik, Z. and R. V. Edouard (2003b). "Recovery of Value Fission Platinoids from Spent Nuclear Fuel". *Platinum Metals Rev.* 47 (3), pp. 123–131. URL: https://www.ingentaconnect.com/search/article?option2=author&value2=Renard%2c+Edouard+V.&pageSize=10&index=2#.

Kolarik, Z. and R. V. Edouard (2005). "Recovery of Value Fission Platinoids from Spent Nuclear Fuel". *Platinum Metals Rev.* 49 (2), pp. 79–90. URL: https://www.ingentaconnect.com/search/article?option2=author&value2=Kolarik.

Korschinek, G. et al. (1994). "AMS for M > 36 with a gas-filled magnetic spectrograph". *Nuclear Instruments and Methods in Physics Research Section B: Beam Interactions with Materials and Atoms* 92 (1), pp. 146–152. ISSN: 0168-583X. URL: https://doi.org/10.1016/0168-583X(94)95995-1.

Kutschera, W. (2013). "Applications of accelerator mass spectrometry". *International Journal of Mass Spectrometry* 349-350, pp. 203–218. ISSN: 1387-3806. URL: https://doi.org/10.1016/j.ijms.2013.05.023.

Kuznetsov, S. V. et al. (1989). "Gas-phase negative ions of platinum metal fluorides. I. Electron affinity of platinum metal tetrafluorides". *International Journal of Mass Spectrometry and Ion Processes* 87 (1), pp. 1–11. ISSN: 0168-1176. URL: https://doi.org/10.1016/0168-1176(89)80001-1.

Lachner, J. et al. (2019). "^{36}Cl in a new light: AMS measurements assisted by ion-laser interaction". *Nuclear Instruments and Methods in Physics Research Section B: Beam Interactions with Materials and Atoms* 456, pp. 163–168. ISSN: 0168-583X. URL: https://doi.org/10.1016/j.nimb.2019.05.061.

Li, J. et al. (2018). "$^{99}TcO_4^-$ remediation by a cationic polymeric network". *Nature Communications* 9 (3007). URL: https://doi.org/10.1038/s41467-018-05380-5.

Liljestrand, R. et al. (1976). "Target thickness uniformity gauge". *Nuclear Instruments and Methods* 138 (3), pp. 471–477. ISSN: 0029-554X. URL: https://doi.org/10.1016/0029-554X(76)90313-X.

Litherland, A.E. et al. (2007). "Isobar separation at very low energy for AMS". *Nuclear Instruments and Methods in Physics Research Section B: Beam In-*

teractions with Materials and Atoms 259 (1). Accelerator Mass Spectrometry, pp. 230–235. ISSN: 0168-583X. URL: https://doi.org/10.1016/j.nimb.2007.01.254.

Liu, Y. et al. (2002). "Collisional cooling of negative-ion beams". *Nuclear Instruments and Methods in Physics Research Section B: Beam Interactions with Materials and Atoms* 187 (1), pp. 117–131. ISSN: 0168-583X. URL: https://doi.org/10.1016/S0168-583X(01)00844-8.

Liu, Y. et al. (2007). "A high efficiency RF quadrupole ion beam cooler for negative ions". *Nuclear Instruments and Methods in Physics Research Section B: Beam Interactions with Materials and Atoms* 255 (2), pp. 416–422. ISSN: 0168-583X. URL: https://doi.org/10.1016/j.nimb.2006.11.128.

Maffioli, L. et al. (1996). "Applications of ^{99m}Tc-Sestamibi in Oncology". *Tumori Journal* 82 (1), pp. 12–21. URL: https://doi.org/10.1177/030089169608200103.

Magill, J. et al. (2006). *Karlsruher Nuklidkarte, 7^{th} edition*.

Major, F. et al. (2006). *Charged Particle Traps*. Springer.

Marek, C. (2018). "AMS measurements of ^{36}Cl using isobar suppression via laser photodetachment". MA thesis. University of Vienna.

Martin, J. E. (1987). "Measurement of ^{90}Sr in reactor wastes by Cerenkov counting of ^{90}Y". *International Journal of Radiation Applications and Instrumentation. Part A. Applied Radiation and Isotopes* 38 (11), pp. 953–957. ISSN: 0883-2889. URL: https://doi.org/10.1016/0883-2889(87)90267-X.

Martschini, M. et al. (2017). "Selective laser photodetachment of intense atomic and molecular negative ion beams with the ILIAS RFQ ion beam cooler". *International Journal of Mass Spectrometry* 415, pp. 9–17. ISSN: 1387-3806. URL: http://www.sciencedirect.com/science/article/pii/S1387380616302378.

Martschini, M. et al. (2019). "The ILIAMS project - An RFQ ion beam cooler for selective laser photodetachment at VERA". *Nuclear Instruments and Methods in Physics Research Section B: Beam Interactions with Materials and Atoms* 456, pp. 213–217. ISSN: 0168-583X. URL: https://doi.org/10.1016/j.nimb.2019.04.039.

Moreau, T. (2016). "Development and characterization of the Ion Laser InterAction Setup (ILIAS)". MA thesis. University of Vienna.

Müller, A.M. et al. (2010). "Competitive ^{10}Be measurements below 1MeV with the upgraded ETH-TANDY AMS facility". *Nuclear Instruments and Methods in Physics Research Section B: Beam Interactions with Materials and Atoms* 268 (17), pp. 2801–2807. ISSN: 0168-583X. URL: https://doi.org/10.1016/j.nimb.2010.05.104.

Nieminen, A. et al. (2001). "Beam cooler for low-energy radioactive ions". *Nuclear Instruments and Methods in Physics Research Section A: Accelerators, Spectrometers, Detectors and Associated Equipment* 469 (2), pp. 244–253. ISSN: 0168-9002. URL: https://doi.org/10.1016/S0168-9002(00)00750-6.

Norquist, P. L. et al. (1999). "Theoretical and experimental binding energies for the d^7s^24F levels in Ru^-, including calculated hyperfine structure and $M1$ decay rates". *Phys. Rev. A* 59 (3), pp. 1896–1902. URL: https://link.aps.org/doi/10.1103/PhysRevA.59.1896.

O´Brien, R. C. et al. (2008). "Safe radioisotope thermoelectric generators and heat sources for space applications". *Journal of Nuclear Materials* 377 (3), pp. 506–521. ISSN: 0022-3115. URL: https://doi.org/10.1016/j.jnucmat.2008.04.009.

Paul, M. (1990). "Separation of isobars with a gas-filled magnet". *Nuclear Instruments and Methods in Physics Research Section B: Beam Interactions with Materials and Atoms* 52 (3), pp. 315–321. ISSN: 0168-583X. URL: https://doi.org/10.1016/0168-583X(90)90429-X.

Paul, W. and H. Steinwedel (1953). "Notizen: Ein neues Massenspektrometer ohne Magnetfeld". *Zeitschrift für Naturforschung A* 8 (7), pp. 448–450. URL: https://doi.org/10.1515/zna-1953-0710.

Pitters, J. (2015). "Laser Photodetachment in a Gas-Filled RF-Quadrupole". MA thesis. University of Vienna.

Pöllänen, R. et al. (1997). "Transport of radioactive particles from the chernobyl accident". *Atmospheric Environment* 31 (21), pp. 3575–3590. ISSN: 1352-2310. URL: https://doi.org/10.1016/S1352-2310(97)00156-8.

Popma, J. J. et al. (2002). "Randomized Trial of ^{90}Sr/^{90}Y β-Radiation Versus Placebo Control for Treatment of In-Stent Restenosis". *Circulation* 106 (9), pp. 1090–1096. URL: https://www.ahajournals.org/doi/abs/10.1161/01.CIR.0000027814.96651.72.

Priller, A. et al. (1997). "First performance tests of VERA". *Nuclear Instruments and Methods in Physics Research Section B: Beam Interactions with Materials and Atoms* 123 (1), pp. 193–198. ISSN: 0168-583X. URL: https://doi.org/10.1016/S0168-583X(96)00780-X.

Purser, K. H. (1977). "Ultra-sensitive spectrometer for making mass and elemental analyses". *US Patent* 4,037,100. URL: https://patents.google.com/patent/US4037100A/en.

Quinn, J. L. (1965). "Tc^{99m} Pertechnetate for Brain Scanning". *Radiology* 84 (2), pp. 354–355. URL: https://doi.org/10.1148/84.2.354.

Quinto, F. et al. (2019). "Ultratrace Determination of 99Tc in Small Natural Water Samples by Accelerator Mass Spectrometry with the Gas-Filled Analyzing Magnet System". *Analytical Chemistry* 91 (7), pp. 4585–4591. URL: https://doi.org/10.1021/acs.analchem.8b05765.

Raisbeck, G.M. et al. (1984). "Measurement of ^{10}Be with a tandetron accelerator operating at 2 MV". *Nuclear Instruments and Methods in Physics Research Section B: Beam Interactions with Materials and Atoms* 5 (2), pp. 175–178. ISSN: 0168-583X. URL: https://doi.org/10.1016/0168-583X(84)90505-6.

Ramond, T. M. et al. (2002). "Photoelectron Spectroscopy of Nickel, Palladium, and Platinum Oxide Anions". *Journal of Molecular Spectroscopy* 216 (1), pp. 1–14. ISSN: 0022-2852. URL: https://doi.org/10.1006/jmsp.2002.8669.

Rienstra-Kiracofe, J. C. et al. (2002). "Atomic and Molecular Electron Affinities: Photoelectron Experiments and Theoretical Computations". *Chemical Reviews* 102 (1), pp. 231–282. URL: https://doi.org/10.1021/cr990044u.

Salvatores, M. and G. Palmiotti (2011). "Radioactive waste partitioning and transmutation within advanced fuel cycles: Achievements and challenges". *Progress in Particle and Nuclear Physics* 66 (1), pp. 144–166. ISSN: 0146-6410. URL: https://doi.org/10.1016/j.ppnp.2010.10.001.

Scheer, M. et al. (1998). "Laser spectroscopic measurements of binding energies and fine-structure splittings of Co^-, Ni^-, Rh^-, and Pd^-". *Phys. Rev. A* 58 (3), pp. 2051–2062. URL: https://link.aps.org/doi/10.1103/PhysRevA.58.2051.

Shand, P. et al. (2009). "Sr isotopes in natural waters: Applications to source characterisation and water-rock interaction in contrasting landscapes". *Applied*

Geochemistry 24 (4), pp. 574–586. ISSN: 0883-2927. URL: https://doi.org/10.1016/j.apgeochem.2008.12.011.

Sidorov, L. N. et al. (1982). "Electron affinities of higher molybdenum fluorides as determined by the effusion technique". *Chemical Physics* 71 (1), pp. 145–156. ISSN: 0301-0104. URL: https://doi.org/10.1016/0301-0104(82)87014-6.

Stamoulis, K. C. et al. (1999). "Strontium-90 concentration measurements in human bones and teeth in Greece". *Science of The Total Environment* 229 (3), pp. 165–182. ISSN: 0048-9697. URL: https://doi.org/10.1016/S0048-9697(99)00052-2.

Steier, P. (2000). "Exploring the limits of VERA. PhD thesis". PhD thesis. University of Vienna.

Steier, P. et al. (2004). "VERA, an AMS facility for „all" isotopes". *Nuclear Instruments and Methods in Physics Research Section B: Beam Interactions with Materials and Atoms* 223-224, pp. 67–71. ISSN: 0168-583X. URL: https://doi.org/10.1016/j.nimb.2004.04.017.

Steier, P. et al. (2019). "The actinide beamline at VERA". *Nuclear Instruments and Methods in Physics Research Section B: Beam Interactions with Materials and Atoms* 458, pp. 82–89. ISSN: 0168-583X. URL: https://doi.org/10.1016/j.nimb.2019.07.031.

Synal, H.-A. (2013). "Developments in accelerator mass spectrometry". *International Journal of Mass Spectrometry* 349-350, pp. 192–202. ISSN: 1387-3806. URL: https://doi.org/10.1016/j.ijms.2013.05.008.

Tagami, K. and S. Uchida (2002). "Global Fallout Technetium-99 Distribution and Behavior in Japanese Soils". *Journal of Nuclear and Radiochemical Sciences* 3 (2), pp. 1–5. URL: https://www.jstage.jst.go.jp/article/jnrs2000/3/2/3_2_1/_article/-char/ja/.

Tumey, S. J. et al. (2009). "Further development of accelerator mass spectrometry for the measurement of ^{90}Sr at Lawrence Livermore National Laboratory". *Journal of Radioanalytical and Nuclear Chemistry* 282 (3), pp. 821–824. ISSN: 1588-2780. URL: https://doi.org/10.1007/s10967-009-0327-9.

Universität Wien - Isotopenphysik (2019). https://isotopenphysik.univie.ac.at/projekte/fwf-projekt-technetium-99/. Accessed: 2019-10-16.

Vockenhuber, C. et al. (2007). "Development of isobar separation for ^{182}Hf AMS measurements of astrophysical interest". *Nuclear Instruments and Methods in Physics Research Section B: Beam Interactions with Materials and Atoms* 259 (1), pp. 250–255. ISSN: 0168-583X. URL: https://doi.org/10.1016/j.nimb.2007.01.223.

Wacker, L. et al. (2004). "Developments in AMS of ^{99}Tc". *Nuclear Instruments and Methods in Physics Research Section B: Beam Interactions with Materials and Atoms* 223-224, pp. 185–189. ISSN: 0168-583X. URL: https://doi.org/10.1016/j.nimb.2004.04.038.

Wendt, K. et al. (2000). "Resonant laser ionization mass spectrometry: An alternative to AMS?" *Nuclear Instruments and Methods in Physics Research Section B: Beam Interactions with Materials and Atoms* 172 (1), pp. 162–169. ISSN: 0168-583X. URL: c.

Wigner, E. P. (1948). "On the Behavior of Cross Sections Near Thresholds". *Phys. Rev.* 73 (9), pp. 1002–1009. URL: https://link.aps.org/doi/10.1103/PhysRev.73.1002.

Yaroshevsky, A. A. (2006). "Abundances of chemical elements in the Earth's crust". *Geochemistry International* 44 (1), pp. 48–55. ISSN: 1556-1968. URL: https://doi.org/10.1134/S001670290601006X.

Yoder, B. L. et al. (2005). "Structures of $Mo_2O_y^-$ and Mo_2O_y (y=2, 3, and 4) studied by anion photoelectron spectroscopy and density functional theory calculations". *The Journal of Chemical Physics* 122 (9), p. 094313. URL: https://doi.org/10.1063/1.1853379.

Zhao, X.-L. et al. (2010). "Studies of anions from sputtering I: Survey of MF_n^-". *Nuclear Instruments and Methods in Physics Research Section B: Beam Interactions with Materials and Atoms* 268 (7), pp. 807–811. ISSN: 0168-583X. URL: https://doi.org/10.1016/j.nimb.2009.10.036.

Zhou, Zh. et al. (2002). "Cooling beams of negative ions". *International Journal of Mass Spectrometry* 218 (3), pp. 199–205. ISSN: 1387-3806. URL: https://doi.org/10.1016/S1387-3806(02)00711-X.